Linear and Nonlinear Analysis of Susceptibility of F/A-18 Flight Control Laws to the Falling Leaf Mode

A THESIS
SUBMITTED TO THE FACULTY OF THE GRADUATE SCHOOL
OF THE UNIVERSITY OF MINNESOTA
BY

Abhijit Chakraborty

IN PARTIAL FULFILLMENT OF THE REQUIREMENTS
FOR THE DEGREE OF
MASTER OF SCIENCE

Prof. Gary J. Balas, Adviser

May 2010

Acknowledgements

I would like to thank my parents and my family who have always gone out of their way to help me anytime and every time. I would like to specially thank my brother-in-law Joy who has been very supportive through out my educational career in the States. Thanks to all my friends who have been a huge source of motivation in my life, especially Mahmud, Muntasir, Ashfaque, Zahid, Nabila, Anahita, Hitendra, Aman, Amartya, Rajes, Projjwal and many others. A very special and heartfelt thank goes to Dr. David Dillard and his wife Cindy at Virginia Tech, who have motivated me a lot to pursue graduate school and taken care of me during my undergraduate career.

I owe to a great extent to my Advisor, Dr. Gary Balas, who has been very patient with me and helped me shape where I am today in my graduate school career. I would like to thank Dr. Pete Seiler for many reasons. I probably would not be able to finish this work and writing this acknowledgment now without his help, support and guidance. I acknowledge my thank to Dr. Ufuk Topcu at Caltech and Prof. Andrew Packard at University of California at Berkley for useful discussions. I would also like to thank Dr. Demoz Gebre-Egziabher for useful discussion. My committee members, Dr. William L. Garrard and Dr. Mihailo Jovanovic, who have also provided me with useful comments to my work.

I would like to provide a very special thanks to all my lab mates and colleagues: Paw, Rohit, Arnar, Andrei, Paul, Arda, Hamid, Qian and Austin. They have been the source of my productivity. Besides that, they have also accompanied me to running, going to coffee shop, playing badminton and what not.

Finally, I would like to acknowledge my gratitude to the technical monitor Dr. Christine Belcastro and NASA Langley for supporting our work.

Dedicated

To My Parents

Ritvik and Dinarika

To My Sisters

To My Brother-in-Laws

Abstract

The F/A-18 Hornet aircraft with the original flight control law exhibited an out-of-control phenomenon known as the falling leaf mode. The falling leaf mode went undetected during the validation and verification stage of the flight control law. Several F/A-18 Hornet aircraft were lost due to the falling leaf mode and this led NAVAIR and Boeing to redesign the flight control law. The revised flight control law exhibited successful suppression of the falling leaf mode during flight tests with aggressive maneuvers. Prior to performing expensive flight tests, the flight control law is extensively validated and verified by performing linear robustness analysis at different trim points and running many Monte-Carlo simulations. Additional insight can be gained by using nonlinear analyses. This thesis compares the two flight control laws using standard linear robustness analyses, nonlinear region-of-attraction analyses and Monte Carlo simulations. The classical linear robustness analyses, i.e. gain and phase margin, does not indicate any significant improvement in robustness properties of the revised control law over the baseline design. However, advanced linear robustness analyses, i.e, the μ and worst-case analysis, indicate that the revised design is better able to handle the cross-coupling and variations in the dynamics than the baseline design. However, it can be difficult to interpret these results since the falling leaf motion is a truly nonlinear dynamical phenomenon. Thus nonlinear analyses tools provide useful insight into the susceptibility of both control laws to the falling leaf motion. The results of the nonlinear analyses indicate that the revised flight control law has considerably better stability properties than the baseline design and less susceptible to the falling leaf motion.

Contents

List of Tables

List of Figures

Nomenclature

Abbreviations and Acronyms

AOA Angle-of-attack, rad
$I.C.$ Initial Condition
ROA Region of Attraction
MC Monte Carlo
CAS Control Augmentation System
IM Input Multiplicative
GM Gain Margin
PM Phase Margin
DM Disk Margin
LIN Linearized
SOS Sum-of-Squares

List of Symbols

α	Angle-of-attack, rad
β	Sideslip Angle, rad
V	Velocity, $\frac{ft}{s}$
p	Roll Rate, $\frac{rad}{s}$
q	Pitch Rate, $\frac{rad}{s}$
r	Yaw Rate, $\frac{rad}{s}$
ϕ	Bank Angle, rad
θ	Pitch Angle, rad
ψ	Yaw Angle, rad
T	Thrust, lbf
ρ	Density, $\frac{slugs}{ft^3}$
$\bar{q}$	Dynamic Pressure, $\frac{lbs}{ft^2}$
$\bar{c}$	Mean Aerodynamic Chord, ft
m	Mass, $slugs$
g	Gravitational Constant, $\frac{ft}{s^2}$
a_y	Lateral Acceleration, g
S	Wing Area, ft^2
b	Wing Span, ft

I_{xx} Roll Axis Moment of Inertia, $slug - ft^2$

I_{yy} Pitch Axis Moment of Inertia, $slug - ft^2$

I_{zz} Yaw Axis Moment of Inertia, $slug - ft^2$

I_{xz} Cross-product of Inertia about y-axis, $slug - ft^2$

δ_{ail} Aileron Deflection, rad

δ_{rud} Rudder Deflection, rad

δ_{stab} Stabilator Deflection, rad

l Rolling Moment, $lbs - ft$

M Pitching Moment, $lbs - ft$

n Yawing Moment, $lbs - ft$

L Lift Force, lbs

D Drag Force, lbs

Y Sideforce, lbs

C_m Pitching Moment Coefficient

C_{m_α} Bare Frame Pitching Moment Coefficient, rad^{-1}

$C_{m_{\delta_{stab}}}$ Pitching Moment Coefficient due to Stabilator Deflection, rad^{-1}

C_{m_q} Pitching Moment Coefficient due to Pitch Damping, rad^{-1}

C_l Rolling Moment Coefficient

C_{l_β} Rolling Moment Coefficient due to Sideslip, rad^{-1}

$C_{l_{\delta_{ail}}}$ Rolling Moment Coefficient due to Aileron Deflection, rad^{-1}

$C_{l_{\delta_{rud}}}$ Rolling Moment Coefficient due to Rudder Deflection, rad^{-1}

C_{l_p} Rolling Moment Coefficient due to Roll Rate, rad^{-1}

C_{l_r} Rolling Moment Coefficient due to Yaw Rate, rad^{-1}

C_n Yawing Moment Coefficient

C_{n_β} Yawing Moment Coefficient due to Sideslip, rad^{-1}

$C_{n_{\delta_{ail}}}$ Yawing Moment Coefficient due to Aileron Deflection, rad^{-1}

$C_{n_{\delta_{rud}}}$ Yawing Moment Coefficient due to Rudder Deflection, rad^{-1}

C_{n_p} Yawing Moment Coefficient due to Roll Rate, rad^{-1}

C_{n_r} Yawing Moment Coefficient due to Yaw Rate, rad^{-1}

C_Y Sideforce Coefficient

C_{Y_β} Sideforce Coefficient due to Sideslip, rad^{-1}

$C_{Y_{\delta_{ail}}}$ Sideforce Coefficient due to Aileron Deflection, rad^{-1}

$C_{Y_{\delta_{rud}}}$ Sideforce Coefficient due to Rudder Deflection, rad^{-1}

C_L Lift Force Coefficient

C_{L_α} Bare Frame Lift Force Coefficient, rad^{-1}

$C_{L_{\delta_{stab}}}$ Lift Force Coefficient due to Stabilator Deflection, rad^{-1}

C_D Drag Force Coefficient

C_{D_α} Bare Frame Drag Force Coefficient, rad^{-1}

$C_{D_{\delta_{stab}}}$ Drag Force Coefficient due to Stabilator Deflection, rad^{-1}

μ Structured Singular Value

t Trim Value

Δ Uncertainty Structure

k_m Stability Margin

N Shape Matrix

$p(x)$ Reference Shape Ellipsoid

$V(x)$ Lyapunov Function

$s(x)$ Decision Variable

γ Lyapunov Sub level Set

$\mathcal{E}_\beta$ Ellipsoid

$\bar{\beta}$ ROA Upper Bound

$\underline{\beta}$ ROA Lower Bound

x_c Controller State

x_{cl} Closed-loop State

Chapter 1

Introduction

Safety critical flight systems require extensive validation prior to entry into service. Validation of the flight control system is becoming more difficult due to the increased use of advanced flight control algorithms, e.g. nonlinear flight controls systems. NASA's Aviation Safety Program (AvSP) aims to reduce the fatal (commercial) aircraft accident rate by 90% by 2022 [1]. A key challenge in achieving this goal is the need for extensive validation and certification tools for the flight systems. The current certification and validation procedure involves analysis, simulations, and experimental techniques such as flight tests [1]. Prior to flight tests, extensive analyses and simulations are performed to validate safety of the system. Standard practice is to assess the closed-loop stability and performance characteristics of the aircraft flight control system around numerous trim conditions using linear analysis tools. These techniques include stability margins, robustness analyses and worst-case analyses. These linear analyses are supplemented with Monte Carlo simulations of the full nonlinear equations of motion to provide further confidence in the system performance. The simulations are also used to uncover nonlinear dynamic characteristics, e.g. limit cycles, that are not revealed by the linear analyses. To summarize, current practice involves extensive linear analyses at different trim conditions and probabilistic nonlinear simulations. The certification process typically does not involve nonlinear analysis methods. This gap between linear analyses and Monte Carlo simulations can cause significant nonlinear effects to go undetected. The F/A-18 Hornet aircraft is one example which suffered from the existing gap in the validation procedure.

The US Navy F/A-18 A/B/C/D Hornet aircraft with the original baseline flight

control law experienced a number of out-of-control flight departures since the early 1980's. Many of these incidents have been described as a falling leaf motion of the aircraft [2]. The falling leaf motion dynamics is nonlinear in nature and this poses a great challenge in studying this motion. An extensive revision of the baseline control law was performed by NAVAIR and Boeing in 2001 to suppress departure phenomenon, improve maneuvering performance and to expand the flight envelope [2]. The revised control law was implemented on the F/A-18 E/F Super Hornet aircraft after successful flight tests. These flight tests included aggressive maneuvers that demonstrated successful suppression of the falling leaf motion by the revised control law.

The baseline flight control law of the F/A-18 Hornet aircraft went through the extensive validation and verification process without detecting the susceptibility to the falling leaf motion. The failure to detect the falling leaf motion is not due to the lack of an accurate aerodynamic model. In fact, the nonlinear simulation model of the F/A-18 Hornet aircraft used in this thesis is able to reproduce the falling leaf mode. Thus the failure to detect this susceptibility should be attributed to the lack of appropriate analysis tools. Moreover, the falling leaf motion is due to nonlinearities in the aircraft dynamics and cannot be replicated with linear models. Thus analysis of the F/A-18 control laws is a particularly interesting example for the application of nonlinear robustness analysis techniques.

The thesis employs different analysis tools to validate and verify both the F/A-18 flight control laws' susceptibility to the falling leaf motion. First, the linear robustness properties of the original (baseline) and the revised flight control law are considered. The standard linear robustness metric includes computing the classical and multivariable gain & phase margin for both the control laws. More advanced linear analysis tools, such as μ and suitable worst-case performance analysis of the controllers are considered. However, it can be difficult to interpret these results since the falling leaf motion is a truly nonlinear dynamical phenomenon. The hypotheses is that the nonlinear analyses tools would provide useful insight into the susceptibility of both control laws to the falling leaf motion. Hence, nonlinear analyses, particularly estimating region-of-attraction and Monte-Carlo simulations, are performed to validate the flight controllers' susceptibility to the falling leaf motion.

Estimating region-of-attraction for nonlinear system is a challenging task. However,

significant research has been performed recently on the development of nonlinear analysis tools for computing regions of attraction, reachability sets, input-output gains, and robustness with respect to uncertainty for nonlinear polynomial systems [3–12]. These tools make use of polynomial sum-of-squares (SOS) optimization [12] and hence they can only be applied to systems whose dynamics are described by polynomial vector fields. These techniques offer great potential to complement the linear analyses and nonlinear simulations that are typically used in the flight control validation process. This thesis presents the first application of these techniques to an actual industrial flight control problem and shows the advantage of including the nonlinear analyses techniques in flight control law validation and verification process.

The thesis has the following structure:

- Chapter 2 develops the nonlinear simulation model of the F/A-18 aircraft. The simulation model is constructed by using publicly available data from various papers and reports [13–19]. The aerodynamic model is presented in Appendix A.1. Moreover, the F/A-18 model is also available at .
- Chapter 3 briefly describes the falling leaf motion.
- Chapter 4 presents a simplified architecture of both the baseline and the revised flight control law.
- Chapter 5 performs linear robustness analyses for both baseline and revised flight control law. The analyses include: (i) Gain & phase margin analysis, (ii) μ analysis for unmodeled dynamics uncertainty, (iii) μ analysis for parametric uncertainty in aerodynamic coefficients, and (iv) worst-case analysis for sideslip disturbance rejection properties.
- Chapter 6 presents the main contribution of the thesis. This chapter focuses on estimating upper and lower bounds of the region-of-attraction for both the flight control laws. The upper bound is estimated by Monte Carlo simulation while the estimation of the lower bound involves performing recently developed nonlinear analysis technique involving polynomial SOS optimization algorithm. The F/A-18 aircraft dynamics need to be described by polynomial vector fields in order to use the SOS based nonlinear analysis tools. Hence, this chapter formulates a polynomial description of the F/A-18 aircraft. Moreover, some

heuristic validations are also performed to ensure that the polynomial model captures the dynamic characteristics of the original F/A-18 aircraft, for all engineering purpose. The chapter concludes by rationalizing why the baseline flight control law is susceptible to the falling leaf motion, but the revised design is not based on the nonlinear analysis results.

- Chapter 7 summarizes the results, discusses some limitations and drawbacks of the proposed nonlinear analysis technique. Future research directions are also proposed in this chapter.

Chapter 2

F/A-18 Aircraft Description and Model Development

This chapter contains a brief description of the F/A-18A/B including the physical parameters and the aerodynamic characteristics of the aircraft. More information can be found on the reference [19].

2.1 Vehicle Description

The US Navy F/A-18 aircraft, Figure 2.1[a], is a high performance, twin engine fighter aircraft built by the McDonnell Douglas (currently the Boeing Company) Corporation. The F/A-18-A/B and F/A-18-C/D are single and two seat aircraft, respectively. These variants are commonly known as Hornet. Each engine of the Hornet is a General Electric, F404-GE-400 rated at 16,100-lbf of static thrust at sea level. The aircraft features a low sweep trapezoidal wing planform with 400 ft^2 area and twin vertical tails [19]. Table 2.1 lists the aerodynamic reference and physical parameters of the F/A-18 Hornet [19]. The US Navy has experienced numerous mishaps, including loss of aircraft and pilot, over the life of the F/A-18A/B/C/D Hornet program due to a specific sustained out-of-control oscillatory motion known as the Falling Leaf mode [2]. A revision to the baseline F/A-18 Hornet flight control law was developed and successfully implemented on the F/A-18E/F Super Hornet aircraft in 2001. This revised flight control law has successfully suppressed the falling leaf motion.

[1]Picture taken from http://www.dfrc.nasa.gov/Gallery/Photo/F-18Chase/Small/EC02-0224-1.jpg

Figure 2.1: F/A-18 Hornet

Table 2.1: Aircraft Parameters

Wing Area, S	400 ft^2
Mean Aerodynamic Chord, $\bar{c}$	11.52 ft
Wing Span, b	37.42 ft
Mass, m	1034.5 slugs
Roll Axis Moment of Inertia, I_{xx}	23000 slug-ft^2
Pitch Axis Moment of Inertia, I_{yy}	151293 slug-ft^2
Yaw Axis Moment of Inertia, I_{zz}	169945 slug-ft^2
Cross-product of Inertia about y-axis, I_{xz}	-2971 slug-ft^2

A nonlinear mathematical model of the F/A-18 Hornet aircraft including its aerodynamic characteristics and control surface description is presented for the purpose of linear and nonlinear analysis of flight control system. Moreover, the Super Hornet has similar aerodynamic and inertial characteristics as of the Hornet [2]. Hence, the aerodynamic and inertial properties presented next are used to analyze both the baseline and the revised flight control system.

2.1.1 Control Surfaces

The conventional F/A-18 Hornet aircraft has five pairs of control surfaces: stabilators, rudders, ailerons, leading edge flaps (LEF), and trailing edge flaps (TEF). The leading and trailing edge flaps are used mostly during take-off and landing. Hence, these control effectors are not considered in the control analysis and modeling. Only the symmetric stabilator, aileron and rudder are considered as control effectors for the

analyses performed in this thesis. Note that the differential stabilator's contribution in roll-axis control is ignored in this thesis for simplicity purpose. Longitudinal control or pitch axis control is provided by the symmetric deflection of the stabilators. Deflection of the ailerons is used to control the roll axis or lateral direction, and deflection of the rudders provides directional or yaw axis control. Note, The hydraulic actuation systems for these primary controls are modeled as first order lags. Table 2.2 provides the mathematical models of the actuators and their deflection and rate limits [19]. The actuator dynamics and rate/position limits are neglected in all analyses presented in this paper. Their values are only included for completeness.

Table 2.2: Control Surface and Actuator Configuration

Actuator	Rate Limit	Position Limit	Model
Stabilator, δ_{stab}	$\pm 40°/s$	-24°,+10.5°	$\frac{30}{s+30}$
Aileron, δ_{ail}	$\pm 100°/s$	-25°,+45°	$\frac{48}{s+48}$
Rudder, δ_{rud}	$\pm 61°/s$	-30°,+30°	$\frac{40}{s+40}$

2.2 Equations of Motion

A six degree-of-freedom (DOF) 9-state mathematical model for the F/A-18 aircraft is presented in this section. The F/A-18 Hornet model is described by the conventional aircraft equations of motion [17, 20, 21]. The equations of motion take the form:

$$\dot{x} = f(x, u) \tag{2.1}$$

where,

$$x := \begin{bmatrix} \text{Velocity, } V \text{ (ft/s)} \\ \text{Sideslip Angle, } \beta \text{ (rad)} \\ \text{Angle-of-Attack, } \alpha \text{ (rad)} \\ \text{Roll Rate, } p \text{ (rad/s)} \\ \text{Pitch Rate, } q \text{ (rad/s)} \\ \text{Yaw Rate, } r \text{ (rad/s)} \\ \text{Bank Angle, } \phi \text{ (rad)} \\ \text{Pitch Angle, } \theta \text{ (rad)} \\ \text{Yaw Angle, } \psi \text{ (rad)} \end{bmatrix}, \; u := \begin{bmatrix} \text{Aileron Deflection, } \delta_{ail} \text{ (rad)} \\ \text{Rudder Deflection, } \delta_{rud} \text{ (rad)} \\ \text{Stabilator Deflection, } \delta_{stab} \text{ (rad)} \\ \text{Thrust, } T \text{ (lbf)} \end{bmatrix}$$

The equations of motion are provided next, without any formal derivation or detailed explanation. Readers are encouraged to refer to [17, 20, 21] for a more detailed and formal derivation.

2.2.1 Euler Angles

The rate of change of aircraft's angular positions are provided in Equation (2.2).

$$\begin{bmatrix} \dot{\phi} \\ \dot{\theta} \\ \dot{\psi} \end{bmatrix} = \begin{bmatrix} 1 & \sin\phi\tan\theta & \cos\phi\tan\theta \\ 0 & \cos\phi & -\sin\phi \\ 0 & \sin\phi\sec\theta & \cos\phi\sec\theta \end{bmatrix} \begin{bmatrix} p \\ q \\ r \end{bmatrix} \tag{2.2}$$

2.2.2 Force Equations

The aerodynamic forces, gravity forces and thrust force applied to the aircraft are considered. Thrust force is assumed to be constant. Equation (2.3) defines the force equations.

$$\begin{aligned} \dot{V} = &-\frac{1}{m}(D\cos\beta - Y\sin\beta) + g(\cos\phi\cos\theta\sin\alpha\cos\beta + \sin\phi\cos\theta\sin\beta \\ &- \sin\theta\cos\alpha\cos\beta) + \frac{T}{m}\cos\alpha\cos\beta \qquad (2.3a) \\ \dot{\alpha} = &-\frac{1}{mV\cos\beta}L + q - \tan\beta(p\cos\alpha + r\sin\alpha) \\ &+ \frac{g}{V\cos\beta}(\cos\phi\cos\theta\cos\alpha + \sin\alpha\sin\theta) - \frac{T\sin\alpha}{mV\cos\beta} \qquad (2.3b) \\ \dot{\beta} = &\frac{1}{mV}(Y\cos\beta + D\sin\beta) + p\sin\alpha - r\cos\alpha + \frac{g}{V}\cos\beta\sin\phi\cos\theta \\ &+ \frac{\sin\beta}{V}(g\cos\alpha\sin\theta - g\sin\alpha\cos\phi\cos\theta + \frac{T}{m}\cos\alpha) \qquad (2.3c) \end{aligned}$$

where D, L, Y denotes the drag force, lift force and sideforce, respectively. These forces are explained in Section 2.3. The gravitational constant is taken as, $g = 32.2\text{ft/s}$.

2.2.3 Moment Equations

The aerodynamic moments are associated with external applied moments. The gyroscopic effect of the moment is neglected. Equation (2.4) describes the corresponding moment equations for the F/A-18 Hornet.

$$\begin{bmatrix} \dot{p} \\ \dot{q} \\ \dot{r} \end{bmatrix} = \begin{bmatrix} \frac{I_{zz}}{\kappa} & 0 & \frac{I_{xz}}{\kappa} \\ 0 & \frac{1}{I_{yy}} & 0 \\ \frac{I_{xz}}{\kappa} & 0 & \frac{I_{xx}}{\kappa} \end{bmatrix} \left(\begin{bmatrix} l \\ M \\ n \end{bmatrix} - \begin{bmatrix} 0 & -r & q \\ r & 0 & -p \\ -q & p & 0 \end{bmatrix} \begin{bmatrix} I_{xx} & 0 & -I_{xz} \\ 0 & I_{yy} & 0 \\ -I_{xz} & 0 & I_{zz} \end{bmatrix} \begin{bmatrix} p \\ q \\ r \end{bmatrix} \right) \tag{2.4}$$

where $\kappa = I_{xx}I_{zz} - I_{xz}^2$ and $l,\ M,\ n$ indicates the rolling, pitching and yawing moment, respectively. Again, these moments are explained in Section 2.3.

Equations (2.2), (2.3), and (2.4) describe the mathematical model for the F/A-18 aircraft with the aerodynamic model presented in Section 2.3. This is a standard mathematical representation for describing aircraft dynamics.

2.3 Aerodynamic Model

This section discusses the aerodynamic model of the F/A-18 aircraft. The aerodynamic model is formed using publicly available data from various papers [13–18]. The values and plots of the aerodynamic coefficients are provided in Appendix A.1.

The aircraft motion depends on the aerodynamic forces and moments acting on the vehicle. The aerodynamic forces consist of lift force (L in lbs), drag force (D in lbs), and sideforce (Y in lbs). The aerodynamic moments are described by the pitching moment (M in ft-lbs), rolling moment (l in ft-lbs), and yawing moment (n in ft-lbs). The aerodynamic forces and moments depend on the aerodynamic angles (α and β in rad), angular rates ($p,\ q,\ r$ in rad/s) and control surface deflections ($\delta_{stab},\ \delta_{ail},\ \delta_{rud}$ in rad). These forces and moments are given by:

$$D = \bar{q}SC_D(\alpha, \beta, \delta_{stab}) \tag{2.5a}$$
$$L = \bar{q}SC_L(\alpha, \beta, \delta_{stab}) \tag{2.5b}$$
$$Y = \bar{q}SC_Y(\alpha, \beta, \delta_{ail}, \delta_{rud}) \tag{2.5c}$$
$$l = \bar{q}SbC_l(\alpha, \beta, \delta_{ail}, \delta_{rud}, p, r, V) \tag{2.5d}$$
$$M = \bar{q}S\bar{c}C_M(\alpha, \delta_{elev}, q, V) \tag{2.5e}$$
$$n = \bar{q}SbC_n(\alpha, \beta, \delta_{ail}, \delta_{rud}, p, r, V) \tag{2.5f}$$

where $\bar{q} := \frac{1}{2}\rho V^2$ is the dynamic pressure (lbs/ft^2) and ρ is the air density (lbs/ft^3). C_D, C_L, C_Y, C_l, C_M, and C_n are unitless aerodynamic coefficients. The functional form for the aerodynamic coefficients can be expressed as a sum of terms that model the aerodynamic effects of the basic airframe (C_*,basic), control inputs (C_*,control) and angular rate damping (C_*,rate). Here, '*' can be replaced by $D,\ L,\ Y,\ l,\ M,\ n$.

$$C_D(\alpha, \beta, \delta_{stab}) = C_{D,basic}(\alpha, \beta) + C_{D,control}(\alpha, \delta_{stab}) \tag{2.6a}$$
$$C_L(\alpha, \beta, \delta_{stab}) = C_{L,basic}(\alpha, \beta) + C_{L,control}(\alpha, \delta_{stab}) \tag{2.6b}$$
$$C_Y(\alpha, \beta, \delta_{ail}, \delta_{rud}) = C_{Y,basic}(\alpha, \beta) + C_{Y,control}(\alpha, \delta_{rud}, \delta_{ail}) \tag{2.6c}$$
$$C_l(\alpha, \beta, V, \delta_{ail}, \delta_{rud}) = C_{l,basic}(\alpha, \beta) + C_{l,control}(\alpha, \delta_{rud}, \delta_{ail}) + C_{l,rate}(\alpha, p, r, V) \tag{2.6d}$$
$$C_M(\alpha, \beta, V, \delta_{stab}) = C_{M,basic}(\alpha) + C_{M,control}(\alpha, \delta_{stab}) + C_{M,rate}(\alpha, q, V) \tag{2.6e}$$
$$C_n(\alpha, \beta, V, \delta_{ail}, \delta_{rud}) = C_{n,basic}(\alpha, \beta) + C_{n,control}(\alpha, \delta_{rud}, \delta_{ail}) + C_{n,rate}(\alpha, p, r, V) \tag{2.6f}$$

Due to lack of available data the rate damping effect on the aerodynamic force coefficients ($C_D,\ C_L,\ C_Y$) is ignored in the model formulation. These force coefficients are modeled based only on contributions from the basic airframe and control surfaces.

A number of publications are available which provide the flight test data for the stability and control derivatives of the F/A-18 HARV vehicle [13–18], which has similar aerodynamic characteristics to the F/A-18 Hornet aircraft [22]. The aerodynamic data of the F/A-18 HARV is used to formulate the aerodynamic model for the F/A-18 Hornet. Least-square fitting of the flight data [13–18] is performed to derive a

closed-form expression to the aerodynamic model. Appendix A.1 provides the least squares fits for the aerodynamic coefficients.

There are two important issue associated with fitting the aerodynamic coefficients. First, the flight test data are provided over a range of 5 or 10^o to 60^o angle-of-attack with fewer data points at low angle-of-attack ($0^o \leq \alpha \leq 10^o$). Extrapolation of data within the lower range of angle-of-attack can lead to unrealistic fit which may lead to unrealistic aerodynamic characteristics at low angle-of-attack. For traditional aircraft, the aerodynamic characteristics of the vehicle do not change significantly at low angle-of-attack ($\alpha \leq 10^o$). Hence if data is unavailable then the aerodynamic coefficient is held constant for angle-of-attack between 0^o and 10^o [23]. The resulting model is valid for an angle-of-attack range from $0^o - 60^o$. Second, data is unavailable for nonzero sideslip flight conditions. However, the basic airframe coefficients are functionally dependent on both $\alpha,\ \beta$. In this paper, the basic airframe dependence of $C_Y,\ C_l,\ C_n$, respectively $C_{Y,basic}(\alpha,\beta),\ C_{l,basic}(\alpha,\beta),\ C_{n,basic}(\alpha,\beta)$, in Equation (2.6c), (2.6d), (2.6f), are approximated as $C_{Y,basic}(\alpha)\beta,\ C_{l,basic}(\alpha)\beta,\ C_{n,basic}(\alpha)\beta$ to account for this lack of data. This indicates, for C_Y, that the sideforce is expected to be zero when the sideslip is zero. This approximation step can also be viewed as linearization of the sideslip effect around the origin. Similar approach has been shown in the book by Stevens & Lewis [24]. Moreover, analytical expressions of $C_{D,basic}(\alpha,\beta),\ C_{L,basic}(\alpha,\beta)$ are extracted from the thesis by Lulch [15].

Chapter 3

Falling Leaf

The F/A-18A/B/C/D Hornet aircraft with the original baseline control law are susceptible to an out-of-control flight departure phenomenon with sustained oscillation namely 'falling leaf' motion. The F/A-18 has experienced numerous mishaps due to thisout-of-control motion [2]. The falling leaf mode is nonlinear in nature and poses a great challenge to understand its interaction with the flight control system. An extensive revision of the original (baseline) flight control law was performed by NAVAIR and Boeing in 2001 to suppress this departure phenomenon, improve maneuvering performance and to expand the flight envelope of the vehicle [2]. The falling leaf mode is briefly described in the following paragraph. A more detailed discussion of the falling leaf motion can be found in other references [2, 25].

3.1 Characterization of Falling Leaf Mode

The falling leaf motion of an aircraft can be characterized as large, coupled out-of-control oscillations in the roll rate (p) and yaw rate (r) direction combined with large fluctuations in angle-of-attack (α) and sideslip (β) [2,25]. Figure 3.1 shows the typical roll rate and yaw rate trajectories associated with the falling leaf motion [2, 25]. This out-of-control mode exhibits periodic in-phase roll and yaw rates with large amplitude fluctuations about small or zero mean. Generation of the roll and yaw rate response is mainly due to the large sideslip oscillation. During large sideslip and angle-of-attack motion, the dihedral effect (roll caused by sideslip) of the aircraft wings becomes extremely large and the directional stability becomes unstable. The like-signs of

these two components are responsible for the in-phase motion. The roll rate motion can easily reach up to $\pm 120^{\circ}/s$, while the yaw rate motion can fluctuate around $\pm 50^{\circ}/s$. During this motion, the value of angle-of-attack can reach up to $\pm 70^{\circ}$ with sideslip oscillations between $\pm 40^{\circ}$ [25]. The required aerodynamic nose-down pitching moment is exceeded by the pitch rate generation due to the inertial coupling of the in-phase roll and yaw rates. The reduction in pitching moment is followed by a reduction in normal force, eventually causing a loss of lift in the aircraft. Another distinguishing feature of the falling leaf motion is the time response of α vs. β produces a mushroom shape curve as shown in Figure 3.2.

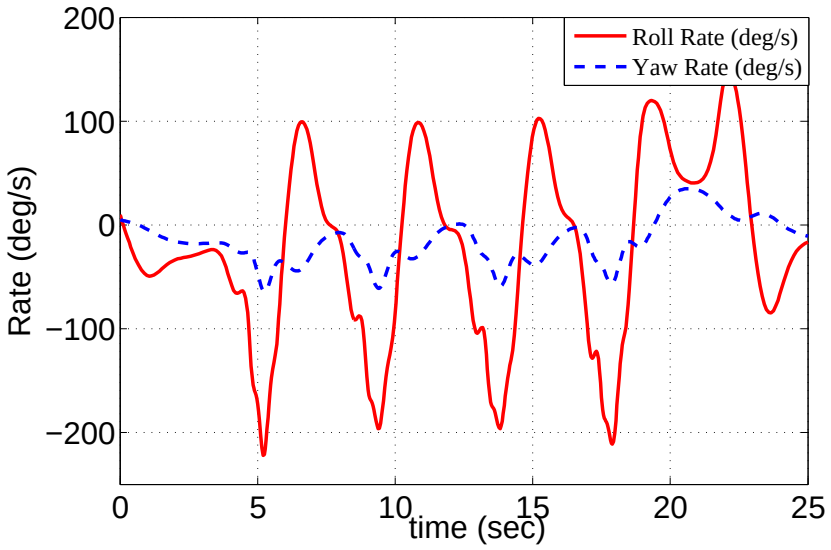

Figure 3.1: Large and coupled roll rate - yaw rate oscillation during falling leaf motion

The characteristics of the falling leaf motion are nonlinear in nature. Figures 3.1 and 3.2 are generated by simulating the nonlinear F/A-18 model presented in this paper. The falling leaf motion shown in Figures 3.1 and 3.2 are generated with the following initial condition.

$$x_o := [350 \text{ (ft/s)} \ 20^o \ 40^o \ 10^o/s \ 0^o/s \ 5^o/s \ 0^o \ 0^o \ 0^o] \tag{3.1}$$

Note that, units of degree are used for ease of interpretation. The model presented in Chapter 2 uses the unit of radian when appropiate. The ordering of the states x are same as mentioned in Equation 2.1. The inputs are set to zeros for this particular simulation. Note that the falling leaf responses cannot be generated by simulating

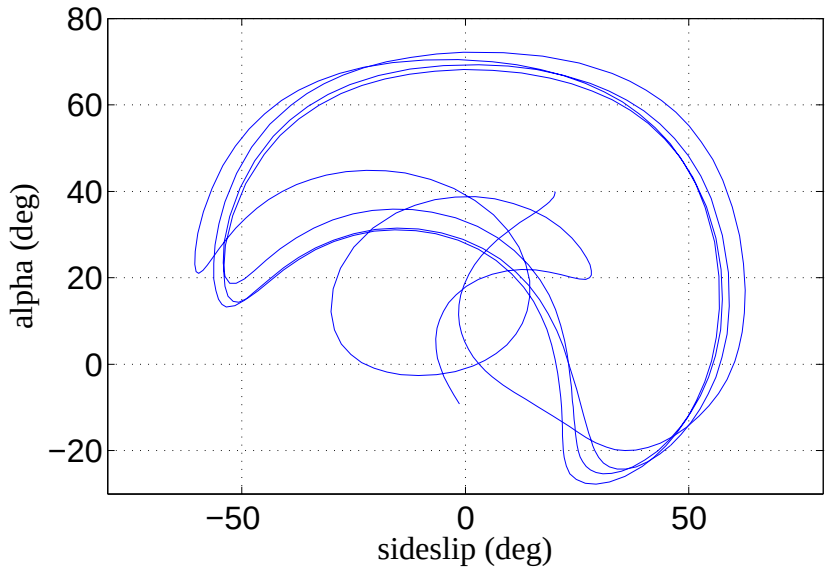

Figure 3.2: Time response of α vs. β produces a mushroom shape curve during falling leaf motion

the linearized models, developed later in Chapter 5.

A study of the falling leaf motion [25] has categorized the motion into three different spectrum: (i) slow falling leaf, (ii) fast falling leaf, and (iii) high alpha fast falling leaf. The primary differences in shifting from the slow to the fast mode can be contributed to the movement of α to higher values, the biasing of yaw rate, and an increase in the frequency of the oscillation. Table 3.1 categorizes the three falling leaf motion as reported in the study [25]. The analyses presented in this thesis are closely related to the slow falling leaf mode category.

Table 3.1: Falling Leaf Categories

State	Slow Mode	Fast Mode	High α Mode
α(deg)	-5 to $+60$	$+20$ to $+70$	$+30$ to $+85$
β(deg)	-40 to $+40$	-40 to $+40$	-40 to $+40$
p(deg/s)	-120 to $+150$	-90 to $+130$	-90 to $+130$
r(deg/s)	-50 to $+50$	-10 to $+60$	-10 to $+75$
period(s)	7	4.7	4.5
frequency(rad/s)	0.898	1.34	1.39

Falling leaf motion should not be confused with the oscillatory spin or a steady spin. Both the oscillatory and steady spin motions produce relatively small α and β fluctuations. Moreover, oscillatory spin produces in-phase roll and yaw rates, and

it fluctuates about large non-zero means unlike falling leaf. The steady spin also exhibits steady roll and yaw rates around large non-zero mean, which is not typical of falling leaf [2].

Chapter 4

F/A-18 Flight Control Laws

An extensive revision of the original (baseline) flight control law was implemented on the F/A-18 E/F Super Hornet in 2001. Numerous aggressive flight tests of the Super Hornet indicated the suppression of the 'falling leaf' motion under the revised flight control law [2]. A simplified architecture of both the baseline and the revised flight control law is presented in this chapter. The state-space realization for both the flight control laws is presented in Section 4.3.

4.1 Baseline Control Law

Figure 4.1 shows the control law architecture for the baseline control laws used for analysis in this paper. The baseline controller structure for the F/A-18 aircraft closely follows the *Control Augmentation System (CAS)* presented in the report by Buttrill, Arbuckle, and Hoffler [19]. The actuators have fast dynamics, as mentioned in Table 2.2, and their dynamics can be neglected without causing any significant variation in the analysis results. Hence, the actuator dynamics, presented in Table 2.2, are ignored for analysis purposes. Differences between the control structure presented in this thesis and the report by Buttrill, Arbuckle, and Hoffler [19] are described in the following sections.

4.1.1 Longitudinal Control

The longitudinal baseline control design for the F/A-18 aircraft includes angle-of-attack (α in rad), normal acceleration (a_n in g), and pitch rate (q in rad/s) measure-

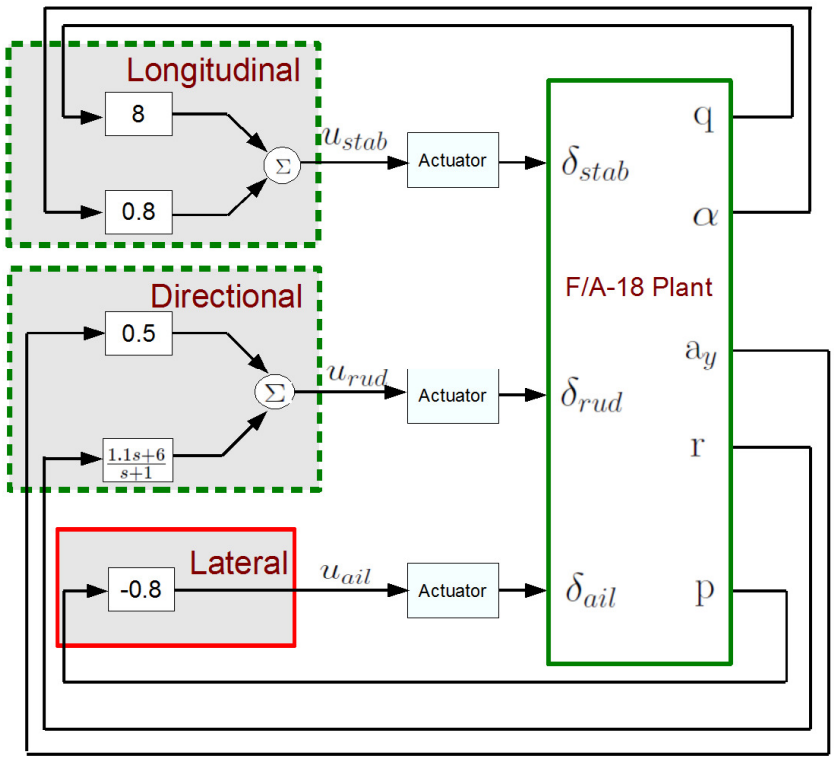

Figure 4.1: F/A-18 Baseline Flight Control Law

ment feedback. The angle-of-attack feedback is used to stabilize an unstable short period mode that occurs during low speed, high angle-of-attack maneuvering. The inner-loop pitch rate feedback is comprised of a proportional feedback gain, to improve damping of the short-period mode. In the high speed regime, the pitch rate proportional gain needs to be increased to avoid any unstable short period mode. The normal acceleration feedback, a proportional-integrator (PI) compensator, has not been implemented in the simplified control law structure. The normal acceleration feedback is usually implemented to stabilize any unstable short period mode of the aircraft. This short period stabilization is provided by α or q feedback in the simplified control law structure presented in this thesis. Hence, the normal acceleration feedback is ignored.

4.1.2 Lateral Control

Control of the lateral direction axis involves roll rate (p) feedback to the aileron actuators. Roll rate feedback is used to improve roll damping and the roll-subsidence

mode of the aircraft. Due to the inherent high roll damping associated with the F/A-18 aircraft at high speed, the roll rate feedback authority is usually reduced at high dynamic pressure. In the low speed regime, the roll rate feedback gain is used to increase damping of the Dutch roll mode. The roll rate feedback gain ranges between 0.8 at low speed to 0.08 at high speed. The flight conditions considered in the analysis in this thesis are at a forward velocity of 350 ft/s. At this speed, a feedback gain of 0.8 is used to provide roll damping.

4.1.3 Directional Control

Directional control involves feedback from yaw rate (r) and lateral acceleration (a_y) to the rudder actuators. Yaw rate is fed back to the rudder to generate a yawing moment. Yaw rate feedback reduces the yaw rate contribution to the Dutch-roll mode. In a steady state turn, there is always a constant nonzero yaw rate present. This requires the pilot to apply larger than normal rudder input to negate the effect of the yaw damper and make a coordinated turn. A washout filter is used to effectively eliminate this effect. The filter approximately differentiates the yaw rate feedback signal at low frequency, effectively eliminating yaw rate feedback at steady state conditions [24]. The lateral acceleration feedback contributes to reduce sideslip during turn coordination.

4.2 Revised Control Law

Figure 4.2 shows the architecture of the revised F/A-18 flight control law as described in the papers by Heller, David, & Holmberg [2] and Heller, Niewoehner, & Lawson [26]. The objective of the revised flight control law was to improve the departure resistance characteristics and full recoverability of the F/A-18 aircraft without sacrificing the maneuverability of the aircraft [2]. The significant changes in the revised control law are the additional sideslip (β) and sideslip rate ($\dot{\beta}$) feedback to the aileron actuators. There are no direct measurements of sideslip and sideslip rate. The sideslip and the sideslip rate feedback signals are computed based on already available signals from the sensors and using the kinematics of the aircraft. Specifically, sideslip rate ($\dot{\beta}$) is estimated by using a 1^{st} order approximation to the sideslip state derivative equation. The sideslip feedback plays a key role in increasing the lateral stability in the $30-35^o$ range of angle-of-attack. The sideslip rate feedback improves the lateral-directional damping. Hence, sideslip motion is damped even at high angles-of-attack. This

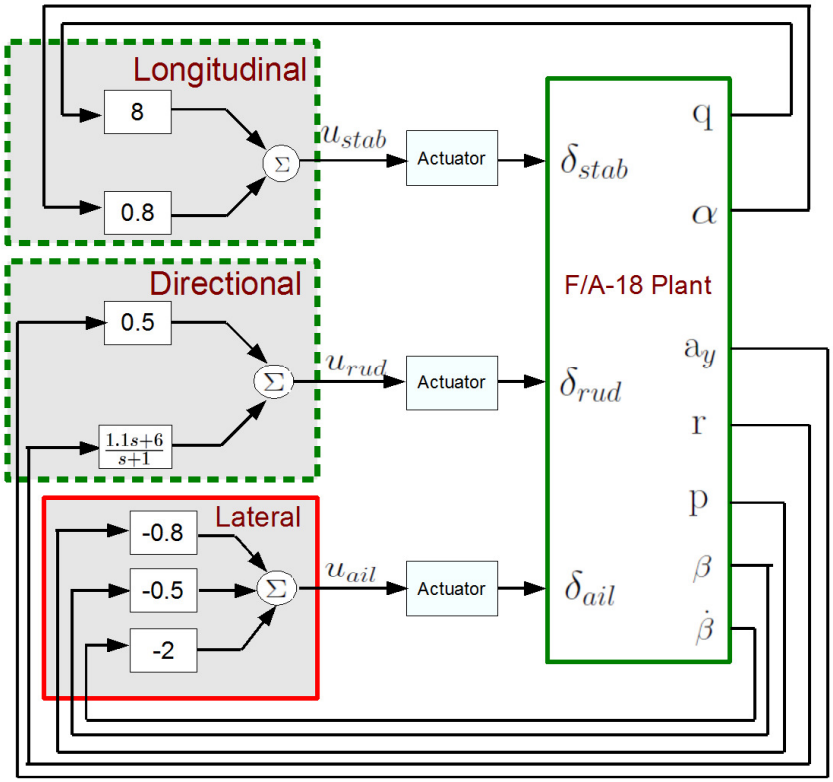

Figure 4.2: F/A-18 Revised Flight Control Law

feature is key to eliminating the falling leaf mode behavior of the aircraft, which is an aggressive form of in-phase Dutch-roll motion. Proportional feedback is implemented in these two feedback channels. The values of the proportional gains are $k_\beta = 0.5$ and $k_{\dot{\beta}} = 2$.

4.3 Controller Realization

State-space realizations for both the baseline and revised flight control laws are presented in this section. Figure 4.3 shows the general architecture of the feedback considered in this thesis. P represents the F/A-18 plant.

The controller, $K = \left[\begin{array}{c|c} A_c & B_c \\ \hline C_c & D_C \end{array}\right]$ can be realized as following:

$$\dot{x}_c = A_c x_c + B_c y \tag{4.1}$$

$$u_3 = C_c x_c + D_c y \tag{4.2}$$

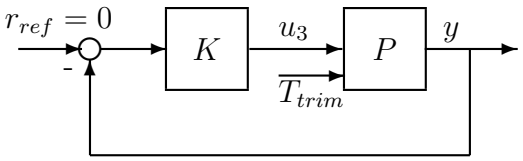

Figure 4.3: Feedback Structure

where x_c is the controller state, $u_3 := [\delta_{ail},\ \delta_{rud},\ \delta_{stab}]$ indicates the input of the plant. Thrust (T) input, mentioned in Chapter 2, is held fixed at its trim value (T_{trim}). The plant measurements are $y := [a_y,\ p,\ r,\ \alpha,\ \beta,\ q,\ \dot{\beta}_{lin}]$. The lateral acceleration is given by $a_y = \dfrac{\bar{q}S}{mg} C_Y$ (in units of g) and computed around a flight condition. Moreover, the measurement signal $\dot{\beta}_{lin}$ represents the linearized representation of the sideslip-rate ($\dot{\beta}$). This signal is estimated by using a 1^{st} order approximation to the sideslip state derivative equation around a flight condition.

The baseline flight control law is:

$$\left[\begin{array}{c|c} A_c & B_c \\ \hline C_c & D_c \end{array}\right] = \left[\begin{array}{c|cccccc} -1 & 0 & 0 & 4.9 & 0 & 0 & 0 & 0 \\ \hline 0 & 0 & 0.8 & 0 & 0 & 0 & 0 & 0 \\ -1 & -0.5 & 0 & -1.1 & 0 & 0 & 0 & 0 \\ 0 & 0 & 0 & 0 & -0.8 & 0 & -8 & 0 \end{array}\right] \tag{4.3}$$

and the revised controller is:

$$\left[\begin{array}{c|c} A_c & B_c \\ \hline C_c & D_c \end{array}\right] = \left[\begin{array}{c|cccccc} -1 & 0 & 0 & 4.9 & 0 & 0 & 0 & 0 \\ \hline 0 & 0 & 0.8 & 0 & 0 & 2 & 0 & 0.5 \\ -1 & -0.5 & 0 & -1.1 & 0 & 0 & 0 & 0 \\ 0 & 0 & 0 & 0 & -0.8 & 0 & -8 & 0 \end{array}\right] \tag{4.4}$$

Chapter 5

Linear Analysis

Current practice for validating flight control laws relies on applying linear analysis tools to assess the closed loop stability and performance characteristics about many trim conditions. Linear analysis investigates robustness issues and possibly worst-case scenarios around the operating points. In this chapter, the F/A-18 aircraft is trimmed around different operating points of interest that are suitable to characterize the falling leaf motion. A reduced 6-state linear representation is extracted from the 9-state linear models around these operating points. This 6-state linear representation is used to construct the closed-loop models for both the baseline and revised flight control law for linear robustness analysis.

5.1 Linear Model Formulation

Linear models are formulated around selected operating points. The flight conditions for these operating points are chosen such that the aircraft is likely to experience the falling leaf motion. Chapter 3 characterized the falling leaf motion similar to the aggressive dutch roll motion with strong coupling in all three axes: longitudinal, lateral and directional. Flight conditions that exhibit coupling in all three directions are suitable candidates for analyzing the falling leaf motion. Therefore, steady-level flight conditions are not considered in the analysis. However, bank angle maneuvers exhibit coupling in all three directions and are suitable to analyze the falling leaf motion. In this thesis, both coordinated ($\beta = 0$ deg) and uncoordinated ($\beta \neq 0^o$) turns with 0^o, 10^o, 25^o, 35^o bank angle are considered. Simulation results [25] have

shown the velocity of the aircraft is usually within 250 - 350 ft/s during the falling leaf motion. The F/A-18 aircraft is trimmed around $V_t = 350$ ft/s. Table 5.1 provides the trim values for the flight conditions considered in this thesis. The subscript 't' denotes the trim value.

Table 5.1: Trim Values around $V_t = 350\frac{ft}{s}$ altitude =25,000 ft

State/Input	Plant 1	Plant 2	Plant 3	Plant 4	Plant 5	Plant 6	Plant 7	Plant 8
α_t (deg)	15.29	15.59	17.43	20.29	15.59	16.16	18.41	21.40
β_t (deg)	0	0	0	0	10	10	10	10
ϕ_t (deg)	0	10	25	35	0	10	25	35
p_t (deg/s)	0	0.1322	0.8695	1.845	-0.1478	-0.5188	-1.074	-1.353
r_t (deg/s)	0	0.7500	1.864	2.635	0.3276	1.084	2.141	2.821
q_t (deg/s)	0	0.1322	0.8695	1.845	0	0.1911	0.9982	1.975
θ_t (deg)	26.10	25.67	22.98	18.69	24.27	25.24	24.45	21.45
ψ_t (deg)	0	0	0	0	0	0	0	0
δ_{stab_t} (deg)	-2.606	-2.683	-3.253	-4.503	-2.669	-2.823	-3.606	-5.101
δ_{ail_t} (deg)	0	-0.1251	-0.3145	-0.4399	12.21	12.45	13.72	15.60
δ_{rud_t} (deg)	0	-0.3570	-0.9109	-1.359	13.24	12.73	11.22	8.334
T_t (lbf)	14500	14500	14500	14500	14500	14500	14500	14500

The F/A-18 aircraft is linearized around the trim points specified in Table 5.1. The linearized plants have the following form:

$$\dot{x} = Ax + Bu \tag{5.1}$$

$$y = Cx + Du \tag{5.2}$$

where $x,\ u$ are described in Section 2.2 and y denotes the output, $y := [a_y,\ p,\ r,\ \alpha,\ \beta,\ q,\ \dot{\beta}]$. Recall, $a_y = \dfrac{\bar{q}S}{mg}C_y$ and $\dot{\beta}$ is computed based on already available signals from the sensors and using the kinematics of the aircraft. The linearized equations for both a_y and $\dot{\beta}$ are used as output signals. Appendix A.2 provides the linear state-space data for Plant 4 and Plant 8 presented in Table 5.1.

A six-state representation of the F/A-18 model is extracted from the above 9-state model, described in Equation (5.1). Decoupling the three states $V,\ \theta,\ \psi$ from the 9-state linear model results in the following 6-state model with the thrust input held

constant at the trim value.

$$\dot{x}_6 = Ax_6 + Bu_3 \tag{5.3}$$

$$y = Cx_6 + Du_3 \tag{5.4}$$

where $x_6 := [\beta,\ \alpha,\ p,\ q,\ r,\ \phi]$ and $u_3 := [\delta_{ail},\ \delta_{rud},\ \delta_{stab}]$.

Table 5.2 shows the eigenvalues of the linear plant (Plant 4) with 9-state and 6-state representation. The zero eigenvalue in the 9-state linear plant is due to the heading angle (ψ) state, which does not affect the dynamics. This state can be ignored in formulating the reduced (6-state) linear plant for analysis. Moreover, the eigenvalues indicate that the dynamic modes of a standard aircraft are present in the F/A-18 linear model. The dynamic modes of the aircraft are: short-period and phugoid mode in the longitudinal axes and dutch roll, roll subsidence and spiral mode in the lateral directional axes. The phugoid mode in the longitudinal direction involves V and θ states. The period of this mode ($T_p \approx 50.3\ s$) is separated by more than an order of magnitude to the one of the short-period ($T_p \approx 3.79\ s$), as shown in Table 5.2. This large time scale separation rationalizes that the phugoid mode can be decoupled from the aircraft model and yet retain the important characteristics of the other dynamic modes of the aircraft.

Table 5.2: Eigenvalue of the F/A-18 Linear Plant

	9-State		6-State	
Mode	Eigenvalue	Period (s)/ Time Constant (s)	Eigenvalue	Period (s)/ Time Constant (s)
Short Period	-0.195 ± 1.66	3.79	-0.194 ± 1.66	3.79
Phugoid	-0.0509 ± 0.125	50.3	N/A	N/A
Dutch Roll	-0.202 ± 0.918	6.85	-0.203 ± 0.933	6.73
Roll Subsidence	-0.307	3.25	-0.302	3.31
Spiral	-0.0209	47.8	-0.0515	19.4
Heading Angle	0	0	N/A	N/A

The rationale for decoupling the $V,\ \theta$ states can also be seen examining the frequency response of the linear models. Figure 5.1 shows a Bode plot of the magnitude response for both the 9-state and 6-state model representation from the stabilator channel input to the six states (x_6). Removal of states V and θ does not affect the aileron and rudder channel as much as the stabilator channel. The bode phase plot is also shown in Figure 5.2. Recall, the frequency for the slow falling leaf motion is approximately

0.9 rad/s, as shown in Table 3.1. Moreover, the magnitude and phase plots show that the 6-state approximation is a good approximation in the interested falling leaf region, above 0.9 rad/s. The two models differ in the low frequency ($\leq$ 0.9 rad/s) region. The mismatch in low frequency region between the two models is acceptable in terms of capturing the characteristics of the falling leaf motion.

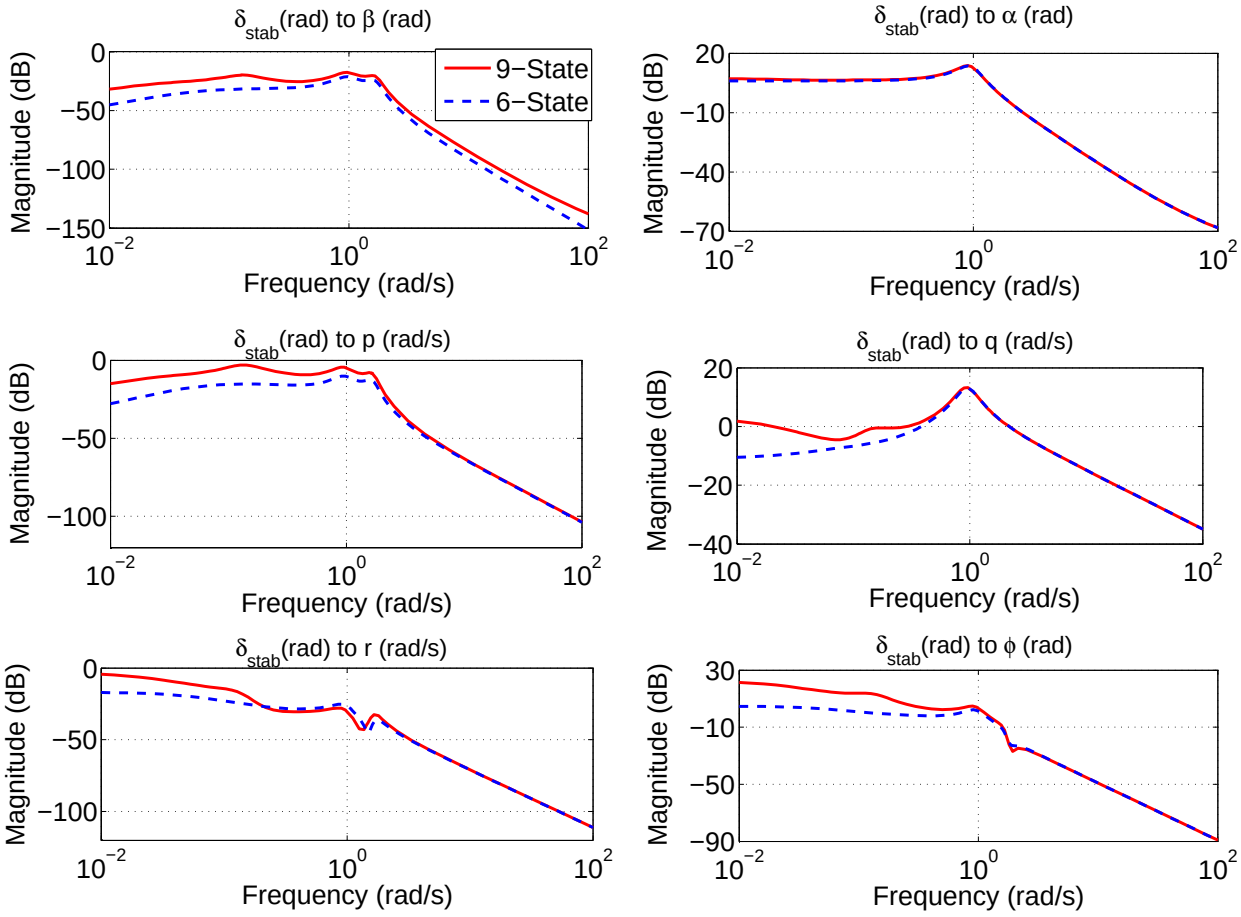

Figure 5.1: Bode plot: Magnitude comparison between the 9-state and 6-state representation

The lateral-directional modes are important to capture the in-phase roll-yaw oscillation characteristics of the falling leaf motion. Hence, these dynamic modes (dutch roll, roll subsidence and spiral mode) involving β, p, r, ϕ states are kept in the formulation of the linear plant. The longitudinal states α, q are also retained in order to capture the short-period mode. Table 5.2 provides the eigenvalue characteristics of the two linear representation. The reduced 6-state representation retains the dynamic modes of the aircraft, excluding the phugoid mode.

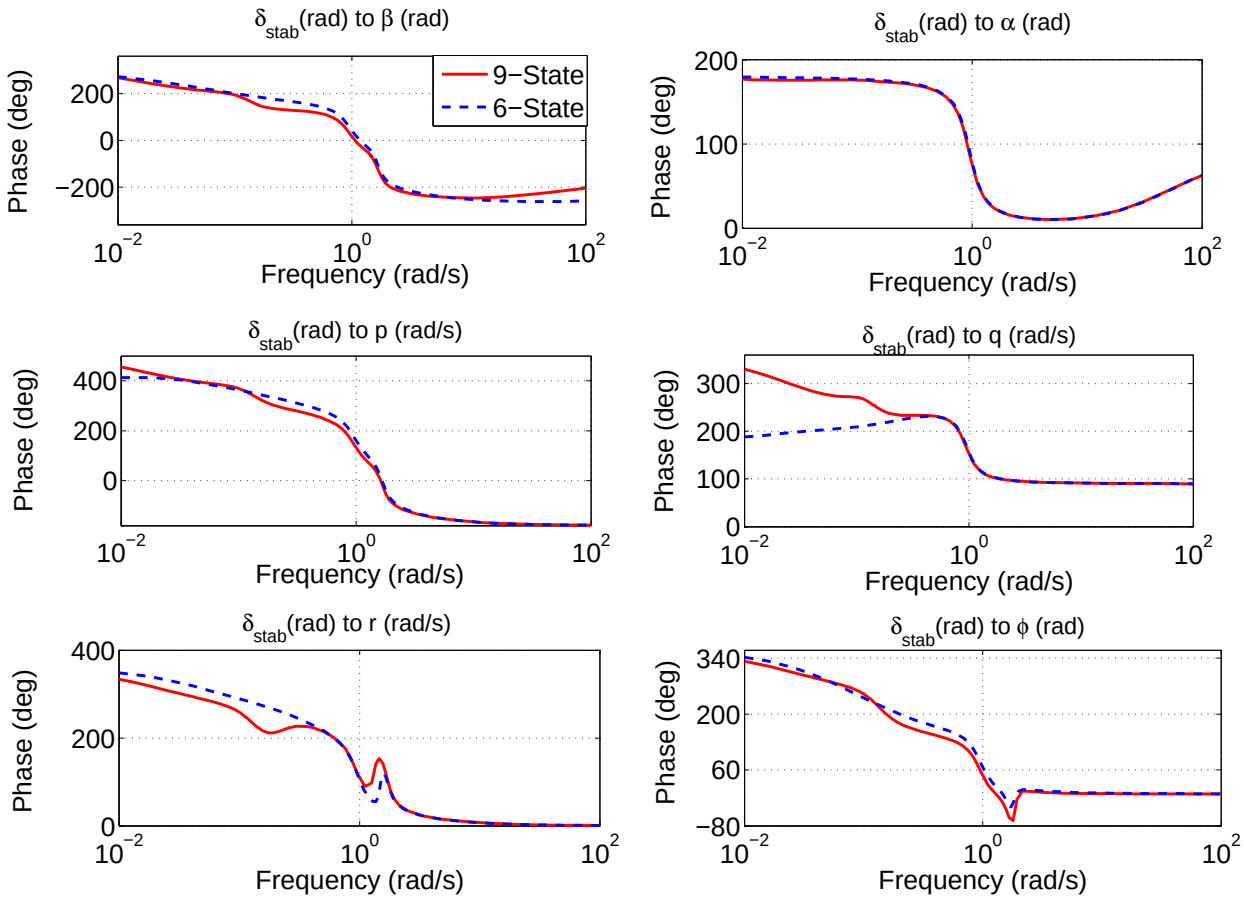

Figure 5.2: Bode plot: Phase comparison between the 9-state and 6-state representation

Six state linear models are constructed for each of the eight operating points. These 6-state linear representations are used to construct the closed-loop model for the baseline and revised flight control law. Eight closed-loop systems are formulated for each of the flight control law; four plants for coordinated turn and four associated with an uncoordinated turn. A variety of linear robustness concepts are employed next to compare the stability performance between the baseline and the revised flight control law.

5.2 Loopmargin Analysis

Gain and phase margins are classical measures of robustness for the closed-loop system. A typical requirement for certification of a flight control law requires the closed-loop system to achieve at least $6dB$ of gain margin and 45^o of phase margin. The

F/A-18 aircraft closed-loop plants under consideration are multivariable; hence, both disk margin and multivariable margin analyses are also performed in addition to the classical loop-at-a-time margin analysis.

5.2.1 Classical Gain, Phase and Delay Margin Analysis

Classical gain, phase and delay margins provide robustness margins for each individual feedback channel with all the other loops closed. This loop-at-a-time margin analysis provides insight on the sensitivity of each channel individually. Table 5.3 provides the classical margins for both the baseline and the revised flight control laws. The results, presented in Table 5.3, are based on the uncoordinated ($\beta = 10^o$) bank turn maneuver at $\phi = 35^o$ (Plant 8). This plant results in the worst margins among all the other plants mentioned in Table 5.1. The baseline and revised flight control laws have very similar classical margins at the input channel. Both the flight control laws are very robust and satisfy the minimum requirement of $6dB$ gain margin and 45^o phase margin.

Table 5.3: Classical Gain & Phase Margin Analysis for Plant 8

Input Channel		**Baseline**	**Revised**
Aileron	*Gain Margin*	43.4 dB	37.1 dB
	Phase Margin	∞	93.6^o
	Delay Margin	∞	0.399 sec
Rudder	*Gain Margin*	21.8 dB	21.7 dB
	Phase Margin	69.5^o	70.8^o
	Delay Margin	2.00 sec	1.38 sec
Stabilator	*Gain Margin*	∞	∞
	Phase Margin	90.4^o	90.4^o
	Delay Margin	0.110 sec	0.110 sec

5.2.2 Disk Margin Analysis

Disk margin analysis provides an estimate of the single-loop robustness to combined gain/phase variations [27]. The disk margin metric is very similar to an exclusion region on a Nichols chart. As with the classical margin calculation, coupling effects between channels may not be captured by this analysis. Table 5.4 provides the disk gain and phase variations at each loop for both the control laws. The results are based on the uncoordinated bank turn maneuver at $\phi = 35^o$ (Plant 8). Again, both

the flight control laws achieve similar robustness margin. The disk margins of the two flight control laws are nearly identical.

Table 5.4: Disk Margin Analysis for Plant 8

Input Channel		**Baseline**	**Revised**
Aileron	*Gain Margin*	43.4 dB	37.1 dB
	Phase Margin	89.2^o	88.4^o
Rudder	*Gain Margin*	7.15 dB	7.92 dB
	Phase Margin	42.6^o	46.2^o
Stabilator	*Gain Margin*	∞	∞
	Phase Margin	90^o	90^o

5.2.3 Multivariable Disk Margin Analysis

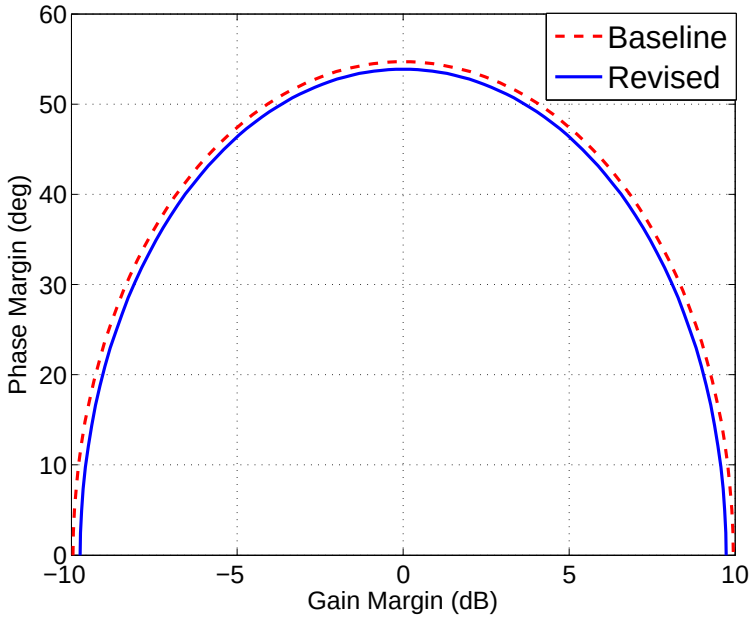

Figure 5.3: Multivariable disk margin analysis for coordinated 35^o bank angle turn

The multivariable disk margin indicates the robustness of the closed-loop system to simultaneous (across all channels), independent gain and phase variations. This analysis is conservative since it allows independent variation of the input channels simultaneously. Figures 5.3 and 5.4 presents the multivaribale disk margin ellipses, respectively for plant 4 (coordinated turn at 35^o bank angle) and plant 8 (uncoordinated turn at 35^o bank angle). The mutivariable disk margin analysis certifies that for simultaneous gain & phase variations in each channel inside the region of the ellipses the closed-loop system remains stable. The mutivariable disk margin analysis

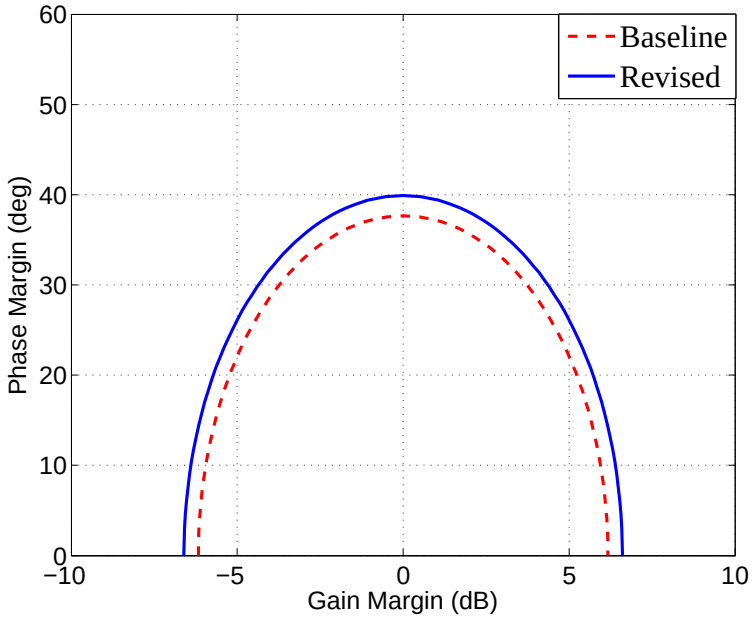

Figure 5.4: Multivariable disk margin analysis for uncoordinated 35^o bank angle turn with 10^o sideslip angle

for steady bank turn maneuvers, Figure 5.3, shows both the baseline and the revised flight control laws have similar multivariable margins. In fact, the baseline appears to have slightly better margin than the revised flight control law. For this steady maneuver, both the control laws are robust to gain variation of up to $\approx \pm 9.5$ dB and phase variation of $\approx \pm 54^o$ across channels. Figure 5.4 shows the mutivariable disk margin analysis for unsteady bank turn maneuvers. Here, the revised flight control law achieves slightly better margin than the baseline flight control law. However, the differences in the margins between the two control laws is not significant enough to conclude which flight control law is susceptible to the falling leaf motion. Moreover, both the control laws achieve the typical margin requirement specification (6dB gain margin and 45^o phase margin) for the steady maneuver. For the unsteady maneuvers, the gain margin requirement is satisfied (both achieves slightly over 6 dB), but the achieved phase margin ($\approx 40^o$) falls short of the requirement.

5.3 Unmodeled Dynamics: Input Multiplicative Uncertainty

Modeling physical systems accurately in many engineering applications is a challenge. A mathematical model of the physical system usually differs from the actual behavior of the system. The F/A-18 aircraft model presented in this paper is no exception.

One approach is to account for the inaccuracies of the modeled aircraft dynamics by unmodeled dynamics entering at the input to the system.

Figures 5.5 shows the general uncertainty structure of the plant that will be considered in the input multiplicative uncertainty analysis. To assess the performance due to the inaccuracies of the vehicle modeled, multiplicative uncertainty, $W_I\Delta_{IM}$, in all three input channels is introduced. The uncertainty Δ_{IM} represents unit norm bounded unmodeled dynamics. The weighting function is set to unity for analysis purpose, $W_I = I_{3\times3}$. The structured singular value (μ) will be used to analyze the uncertain closed-loop system. The $\frac{1}{\mu}$ value measures the stability margin due to the uncertainty description in the system.

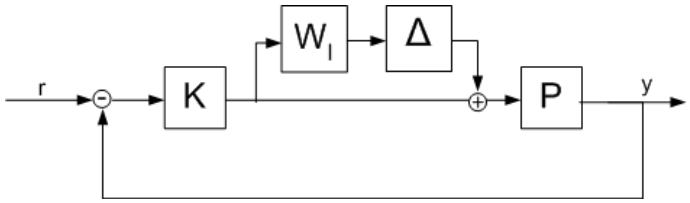

Figure 5.5: F/A-18 Input Multiplicative Uncertainty Structure

5.3.1 Diagonal Input Multiplicative Uncertainty

Figures 5.6 and 5.7 show the μ plot of the baseline and revised closed-loop system for coordinated (plants 1-4) and uncoordinated (plants 5-8) bank maneuvers. The uncertainty, Δ_{IM}, is assumed to have a diagonal structure indicating the presence of uncertainty in each actuation channel but no cross-coupling among the channels. The value of μ at each frequency ω is inversely related to the smallest uncertainty which causes the feedback system to have poles at $\pm j\omega$. Thus the largest value on the μ plot is equal to $1/k_m$ where k_m denotes the stability margin. In Figure 5.6, the peak value of μ is 1.150 ($k_m = 0.8695$) for the revised controller during steady maneuvers. The baseline achieves a peak value of μ is 1.030 ($k_m = 0.9708$). The baseline flight control law achieves a slightly better robustness for the coordinated bank turn maneuvers compared to the revised flight control law. Figure 5.7 shows the peak value of μ for both the control laws at uncoordinated bank turn maneuvers. Here, the baseline flight controller exhibits a peak μ value of 1.894 ($k_m = 0.5279$) and the revised flight controller achieves a μ value of 1.816 ($k_m = 0.5506$). During the uncoordinated maneuvers, the revised controller achieves better stability margins than the baseline design.

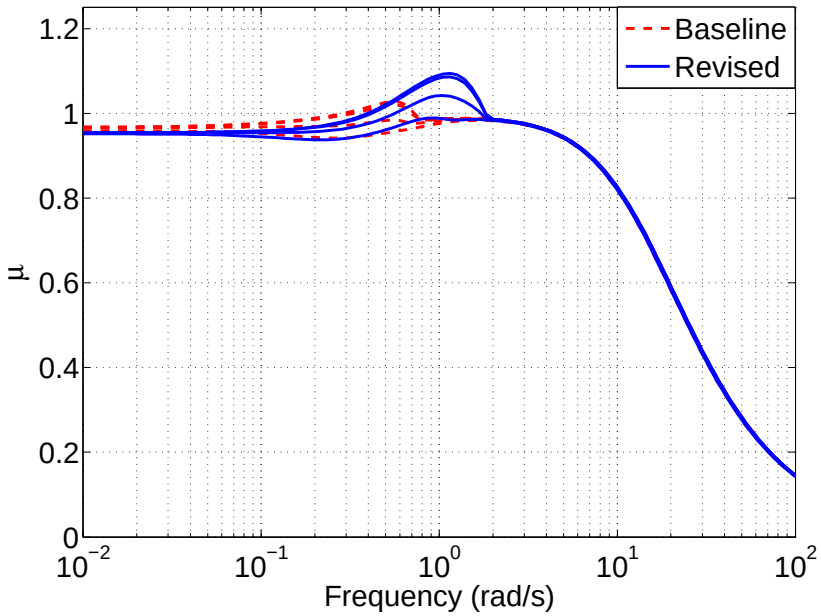

Figure 5.6: Diagonal Input Multiplicative Uncertainty: Coordinated maneuvers

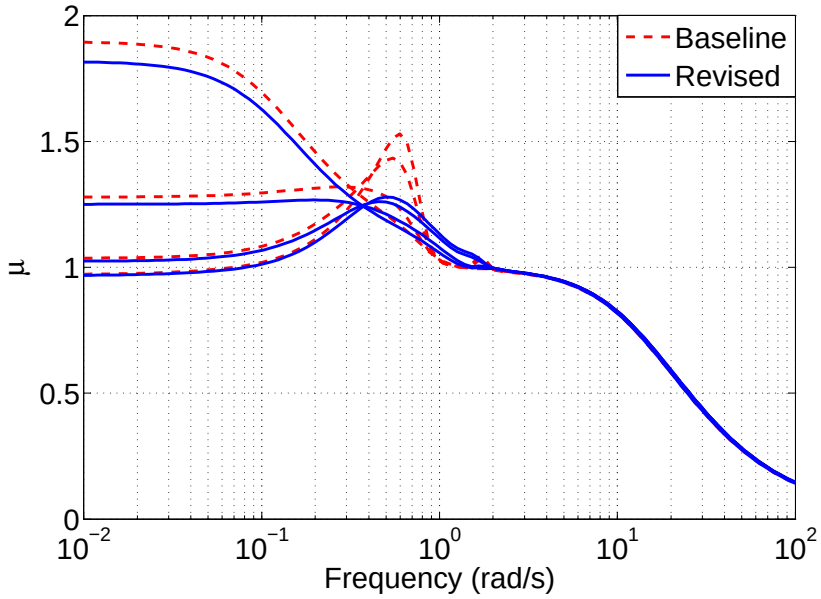

Figure 5.7: Diagonal Input Multiplicative Uncertainty: Uncoordinated maneuvers

Both the flight control laws exhibit similar robustness or stability margins under diagonal input multiplicative uncertainty for both the coordinated and uncoordinated maneuvers. Overall, the stability margins of both the control laws is excellent and nearly identical.

5.3.2 Full Block Input Multiplicative Uncertainty

The input multiplicative uncertainty, Δ_{IM}, is treated as a full block uncertainty in the analysis. This uncertainty structure models the effects of dynamic cross-coupling between the channels to determine how well the flight control laws are able to handle the coupling at the input to the F/A-18 actuators. As mentioned before, the falling leaf motion is an exaggerated form of in-phase Dutch-roll motion with large coupling in the roll-yaw direction. Increased robustness of the flight control law with respect to the full Δ_{IM} is associated with its ability to mitigate the onset of the falling leaf motion. Figure 5.8 presents robustness results for coordinated maneuvers (plants 1-4), and Figure 5.9 presents results for uncoordinated (plants 5-8) maneuvers.

Figure 5.8 shows the μ analysis for coordinated maneuvers. In this case, the baseline flight control law achieves a peak μ value of 1.846 ($k_m = 0.5417$) and the revised flight control law achieves a peak μ value of 1.220 ($k_m = 0.8196$). The results indicate the revised flight control law is more robust compared to the baseline flight control law. Similarly, Figure 5.9 shows the μ analysis for uncoordinated maneuvers. The baseline flight control law achieves a peak μ value of 3.075 ($k_m = 0.3252$) and the revised flight control law achieves a peak μ value of 2.032 ($k_m = 0.4921$).

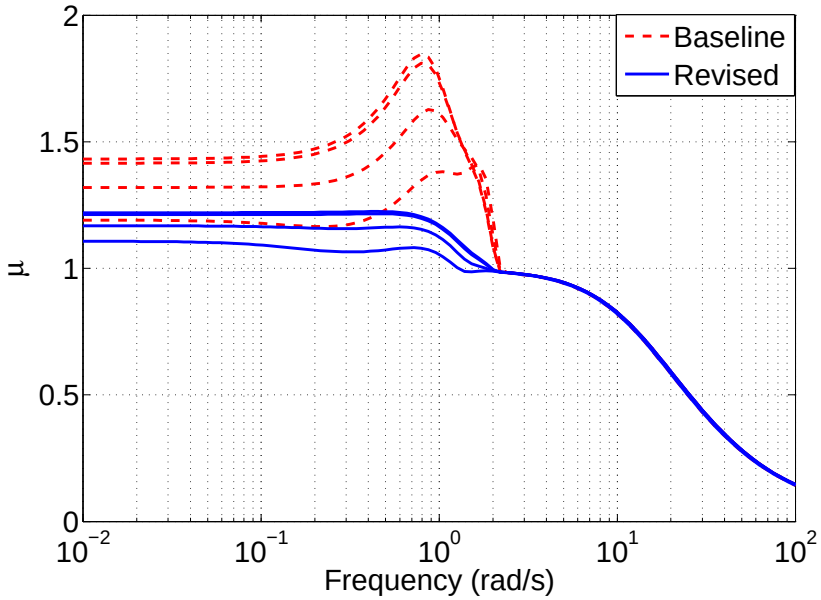

Figure 5.8: Full Block Input Multiplicative Uncertainty: Coordinated maneuvers

Linear robustness analysis analysis with respect to full-block input multiplicative uncertainty across input channels indicate the revised controller being more robust

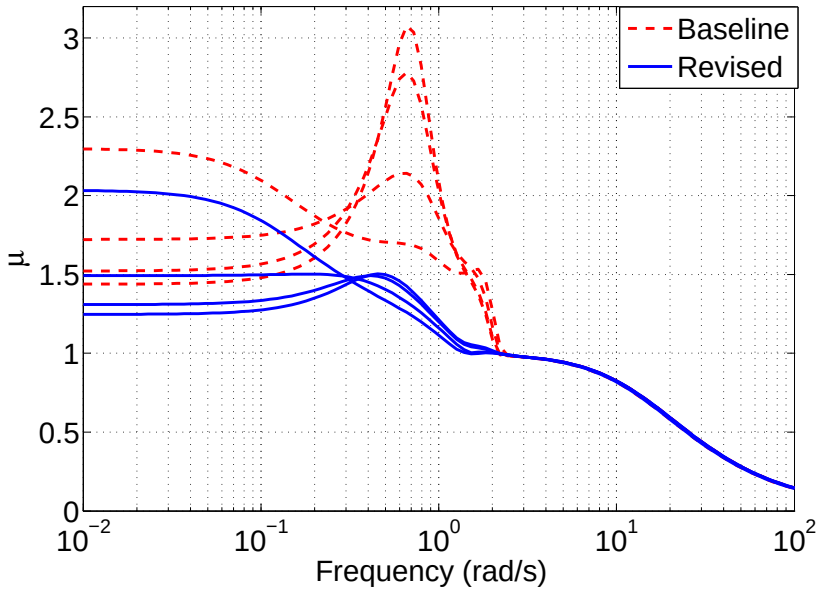

Figure 5.9: Full Block Input Multiplicative Uncertainty: Uncoordinated maneuvers

than the baseline design. This analysis shows that the revised controller is better able to handle the cross-coupling in the actuation channels. Moreover, both Figures 5.8 and 5.9 exhibit the revised controller provides additional damping to the system around approximately 1 rad/s, while the baseline peaks up around that frequency. To this point, the full-block uncertainty analysis has indicated a noticeable difference between the baseline and the revised flight control law.

5.4 Robustness Analysis to Parametric Uncertainty

Robustness analysis of flight control system with parametric uncertainty is another important analysis in validating closed-loop robustness and performance [1]. Moreover, robustness assessment of the flight control law due to the variations of aerodynamic coefficients over the flight envelope needs to be considered. Including parametric uncertainty models into the analysis is one approach to address this issue. Both controllers are examined with respect to robustness in the presence of parametric variations in the plant model. To this end, the stability derivatives of the linearized model are represented with $\pm 10\%$ uncertainty around their nominal values. These terms are chosen carefully to represent the stability characteristics of the F/A-18 aircraft that play an important role in the falling leaf motion. These terms are related to the entries of the linearized open-loop A matrix. The terms in the lateral direc-

tions are: sideforce due to sideslip (Y_β); rolling moment due to sideslip (L_β); yawing moment due to sideslip (N_β); roll damping (L_p); yaw damping (N_r). The following longitudinal terms have also been considered: pitch damping (M_q); normal force due to pitch rate (Z_q); pitch stiffness (M_α). Cook [21] provides a detailed description of these terms. The lateral aerodynamic terms: Y_β, L_β, N_β, L_p, and N_r correspond respectively to the $(1,1)$, $(3,1)$, $(5,1)$, $(3,3)$, and $(5,5)$ entries of the linearized A matrix presented in previous section. The longitudinal aerodynamic terms: M_q, Z_q, and M_α correspond respectively to the $(4,4)$, $(2,4)$, and $(4,2)$ entries of the same linearized A matrix.

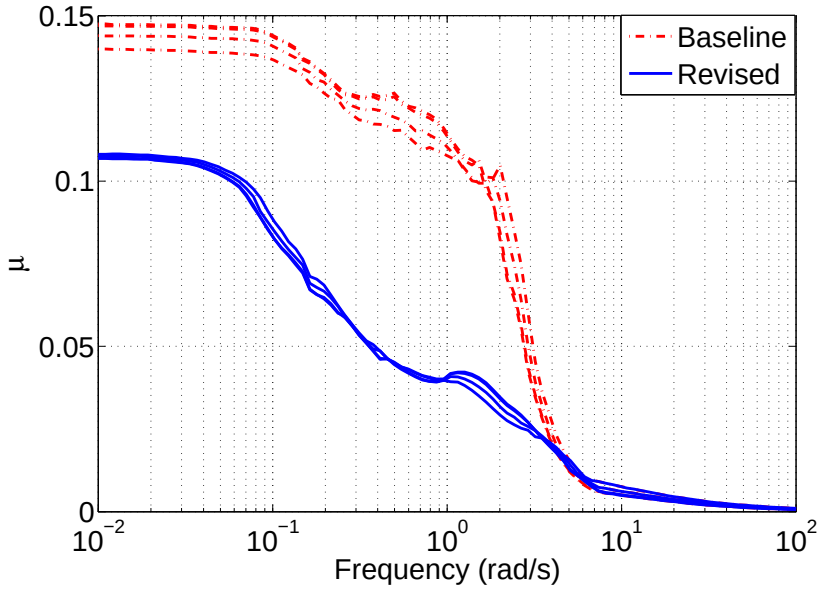

Figure 5.10: Real Parametric Uncertainty in Aerodynamic Coefficients: Coordinated maneuvers

Figures 5.10 and 5.11 show the μ plot of both closed-loop systems with respect to the parametric uncertainty for both coordinated (plants 1-4) and uncoordinated maneuvers (plants 5-8), respectively. In Figure 5.10, the stability margin for parametric uncertainty in the aerodynamic coefficients of the revised controller ($\mu = 0.1080$ and $k_m = 9.259$) is approximately 1.3 times larger than that of the baseline controller ($\mu = 0.1475$ and $k_m = 6.779$). Figure 5.11 presents results based on plants 5-8 for uncoordinated ($\beta = 10^o$) maneuvers. In Figure 5.11, the stability margin for parametric uncertainty in the aerodynamic coefficients of the revised controller ($\mu = 0.2016$ and $k_m = 4.960$) is approximately 1.3 times larger than that of the baseline controller ($\mu = 0.2746$ and $k_m = 3.642$). Hence, the revised flight controller is more robust to

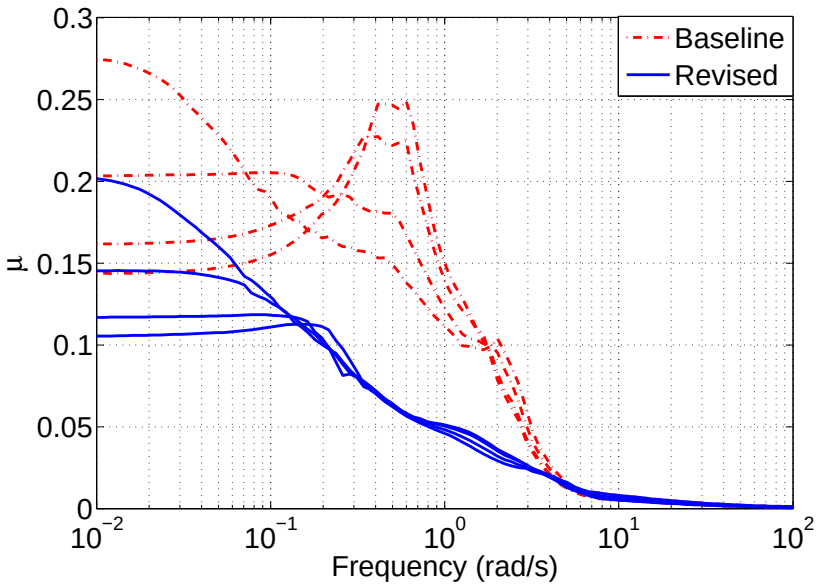

Figure 5.11: Real Parametric Uncertainty in Aerodynamic Coefficients: Uncoordinated maneuvers

error in aerodynamic derivatives than the baseline design. This is specifically true for the uncoordinated turns. With uncoordinated banking maneuvers, the μ value for the baseline flight control law peaks up around 0.7 rad/s, while the revised design does not exhibit the peaking behavior. However, both the flight controllers prove to be very robust against the parametric uncertainty in the stability derivatives.

5.5 Worst-Case Analysis of Flight Control Laws

The ability of the revised flight control law to damp out the sideslip motion, even during high AOA maneuvers, is key in suppressing the falling leaf motion [2]. This motivates a comparison between the worst-case performance of the two flight control laws due to disturbances in aileron and rudder channel, uncertainty in the stability derivatives, and their effect on the sideslip. Figure 5.12 shows the setup of the problem formulation. The transfer function of interest is calculated by the uncertain plant (P_Δ) times input-to-plant sensitivity function ($\frac{P_\Delta}{1+P_\Delta C}$), with aileron and rudder channel being the input and sideslip angle the output. P_Δ represents the uncertain plant. Again, analysis is presented with uncertainty being represented as: (i) parametric uncertainty in aerodynamic coefficients, and (ii) unmodeled dynamics uncertainty.

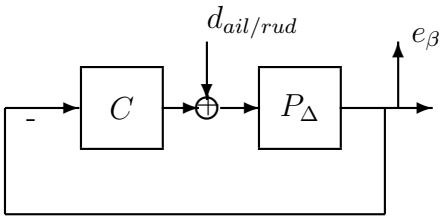

Figure 5.12: Setup of worst-case analysis: 'd' indicates the disturbances in rudder and aileron channel and 'e_β' indicates the Sideslip channel

5.5.1 Worst-Case Parametric Uncertainty Analysis

The uncertainty, in this case, is associated with stability derivatives of the plant as described in Section 5.4. Figure 5.13 shows a frequency-dependent μ plot of the worst-case gain analysis from the sideslip feedback channel to the aileron and rudder input channel for the coordinated maneuvers. Comparatively, the revised flight control law performs better than the baseline flight control law. The baseline flight control achieves a peak worst-case gain of 1.30 while the revised flight control law achieves a worst-case gain of 0.675. Figure 5.14 shows μ plot of the worst-case gain curve for uncoordinated maneuvers. In this case, the revised flight control law performs substantially better than the baseline design. The worst-case gain of the baseline control law is 2.41 while the revised achieves a value of 0.748.

In both maneuvers, the revised flight control law damps out the peak in the worst-case gain in sideslip direction while the baseline fails to do so. This analysis shows that the revised control law is better able to handle worst-case scenarios with respect to the aerodynamic parameter variations in the dynamics.

5.5.2 Unmodeled Dynamics: Diagonal Input Multiplicative Uncertainty

The unmodeled dynamics uncertainty is modeled in the actuation channel with no cross-coupling (diagonal input multiplicative uncertainty) between them, as described in Section 5.3. The results turn out to be similar for the full-block input multiplicative uncertainty case. Hence, only diagonal input multiplicative uncertainty results are presented.

In the diagonal input multiplicative uncertainty case for the coordinated maneuvers, the baseline flight control law achieves a slightly higher worst-case gain value com-

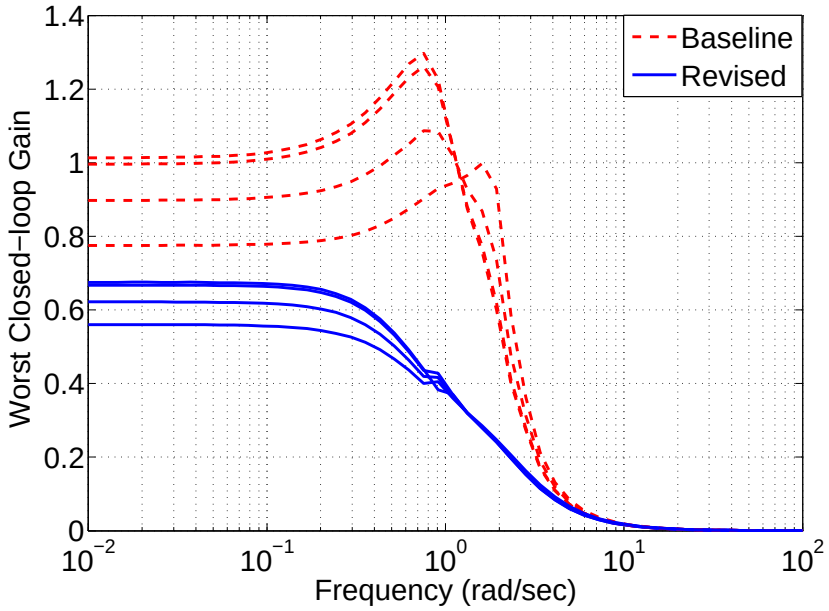

Figure 5.13: Worst-Case closed loop gain as a function of frequency under parametric variations: Coordinated maneuvers

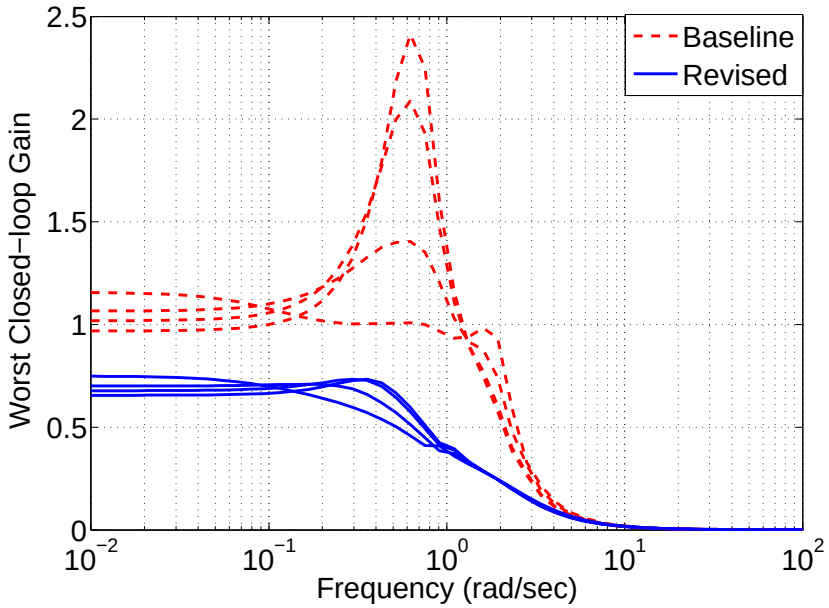

Figure 5.14: Worst-Case closed loop gain as a function of frequency under parametric variations: Uncoordinated maneuvers

pared to the revised flight control law. The revised controller achieves a worst-case gain of 4.12 while the baseline design achieves a gain of 4.70. Figure 5.15 shows the frequency dependent wort-case gain curve of the disturbance rejection properties of

the flight control laws. Moreover, Figure 5.16 shows the worst-case gain curve for the uncoordinated maneuvers. In this flight condition, the worst-case gain for both the baseline and the revised flight control law is same.

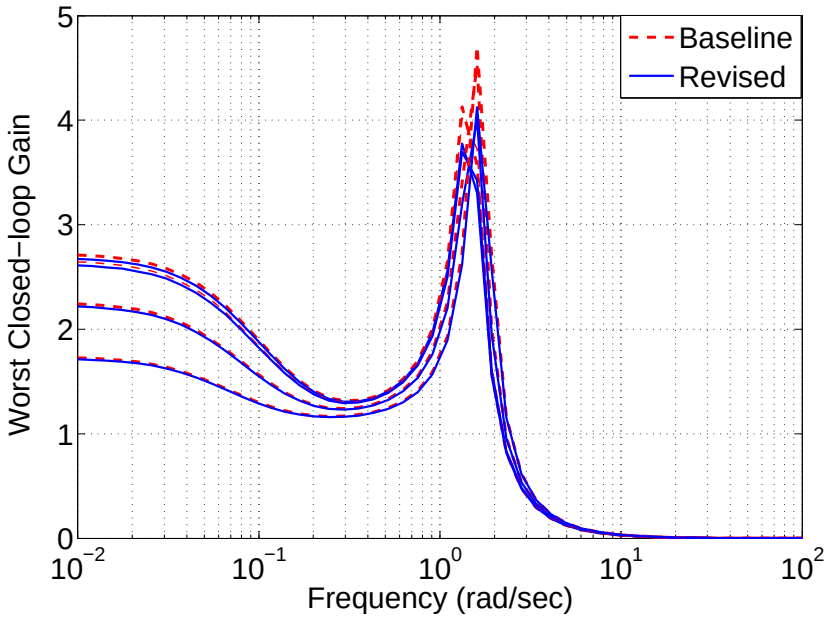

Figure 5.15: Worst-Case closed loop gain as a function of frequency under unmodeled dynamics uncertainty: Coordinated maneuvers

Both the baseline and the revised achieved similar robustness properties for the worst-gain analysis with unmodeled dynamics uncertainty.

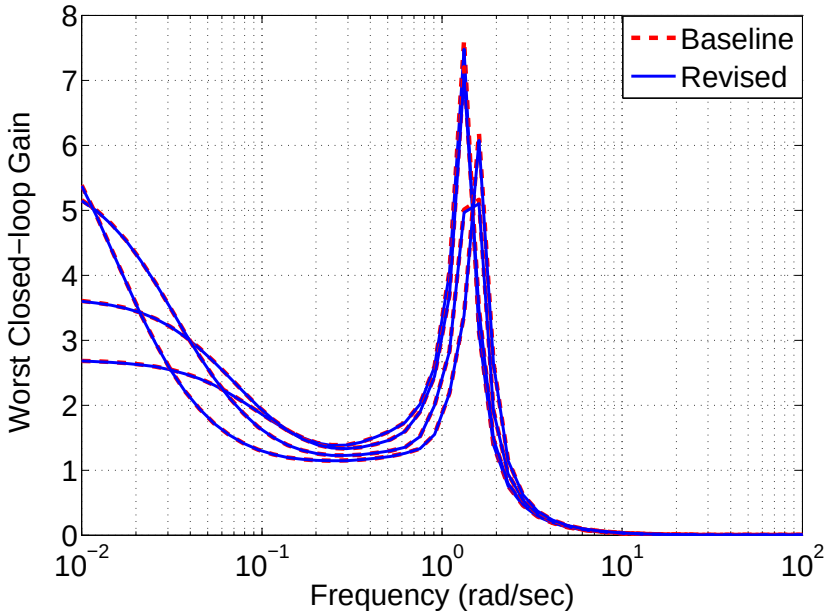

Figure 5.16: Worst-Case closed loop gain as a function of frequency under unmodeled dynamics uncertainty: Uncoordinated maneuvers

5.6 Summary of Linear Analysis Results

Section 5.2 - 5.5 employs various linear robustness analysis techniques to analyze and compare the stability properties of the baseline and the revised flight control law. Gain and phase margin analysis is extensively used during the certification of the flight control law. The standard loopmargin analysis, performed in Section 5.2, shows both the controllers achieve almost identical robustness margin and are very robust. Various μ analyses are performed in the following subsections with different uncertainty structure in the aircraft plant. Section 5.3 analyzes both the controller under the presence of unmodeled dynamics uncertainty in the actuation channel. Both the controllers achiever similar robustness properties under no cross-coupling in the actuation channels. However, the revised design achieves better robustness properties when cross-coupling is present in the actuation channels. Similarly, in Section 5.4, the revised controller achieves better robustness margin under variations in the aerodynamic coefficients. Finally, the worst-case gain analysis is performed in Section 5.5. The worst-case closed-loop gain for the revised controller turns out to be less than the baseline design under variations in aerodynamic coefficients. However, both the controllers achieve similar worst-case closed-loop gain under unmodeled dynamics uncertainty in the actuation channels.

The flight test results have shown that the revised design is able to damp out the falling leaf motion, while the baseline controller clearly failed to do so. Some of the linear analyses results presented so far have shown that the revised control law has better stability properties than the baseline design. However, some linear analyses, including the loopmargin analysis, have found no differences in stability properties between the two control design. This inconsistency in linear analyses motivates to perform nonlinear analysis between the baseline and the revised design.

Chapter 6

Nonlinear Region-of-Attraction Analysis

This chapter discusses the technique for estimating the region-of-attraction (ROA) for (locally asymptotically stable) nonlinear dynamics described by polynomial vector field. This technique is then applied to the F/A-18 aircraft to compare the stability region of the baseline and the revised flight control law.

The outline of this chapter is as follow: Section 6.1 provides a motivation to why nonlinear analysis can be of practical use to the F/A-18 flight control problem. Section 6.2 presents the technical approach to estimating the ROA for polynomial nonlinear system. Polynomial models are constructed in Section 6.3 for the closed loop systems with the baseline and revised flight control laws. This step is required because the computational method to estimate the ROA is only applicable for polynomial systems. Finally, the chapter concludes with Section 6.4, which presents results for the inner and outer approximation to the ROA for the F/A-18 closed-loop dynamics.

6.1 Motivation

The baseline flight control law of the F/A-18 Hornet aircraft went through the extensive validation and verification process without detecting the susceptibility to the falling leaf motion. The failure to detect the falling leaf motion is not due to the lack of an accurate aerodynamic model. In fact, Chapter 3 showed that the nonlinear simulation model of the F/A-18 Hornet aircraft is able to reproduce the falling leaf

mode. Thus the failure to detect this susceptibility should be attributed to the lack of appropriate analysis tools. Chapter 5 showed that classical gain and phase margin analyses indicate that the revised flight control law has similar robustness properties as the baseline flight control law. More advanced linear analysis tools, such as μ and worst-case performance, indicate that the revised flight controller has noticeably better robustness properties than the baseline control law. However, it can be difficult to interpret these results since the falling leaf motion is a truly nonlinear dynamical phenomenon. Thus nonlinear analyses tools would provide useful insight into the susceptibility of both control laws to the falling leaf motion. Recently, significant research has been performed on the development of nonlinear analysis tools for computing regions of attraction, reachability sets, input-output gains, and robustness with respect to uncertainty for nonlinear polynomial systems [3–12]. These tools make use of polynomial sum-of-squares optimization [12] and hence they can only be applied to systems whose dynamics are described by polynomial vector fields. These techniques offer great potential to complement the linear analyses and nonlinear simulations that are typically used in the flight control validation process.

6.2 Region-of-Attraction (ROA) Estimation

This section describes the technical approach to estimate the region of attraction for nonlinear, polynomial systems. This analysis is based on a fundamental difference between asymptotic stability for linear and nonlinear systems. For linear systems, asymptotic stability of an equilibrium point is a global property. In other words, if an equilibrium point is asymptotically stable then its state trajectory will converge back to the equilibrium when starting from any initial condition. For nonlinear systems, asymptotically stable equilibrium points are not necessarily globally asymptotically stable. Khalil [28] and Vidyasagar [29] provide good introductory discussions of this issue. The region-of-attraction (ROA) of an asymptotically stable equilibrium point is the set of initial conditions whose state trajectories converge back to the equilibrium [28]. If the ROA is small, then a disturbance can easily drive the system out of the ROA and the system will fail to come back to the stable equilibrium point. Thus the size of the ROA can be interpreted as a measure of the stability properties of a nonlinear system around an equilibrium point. This motivates the computation of ROA estimates.

Consider an autonomous nonlinear, polynomial system of the form:

$$\dot{x} = f(x),\ x(0) = x_0 \tag{6.1}$$

where $x \in \mathbb{R}^n$ is the state vector and $f : \mathbb{R}^n \to \mathbb{R}^n$ is a multivariable polynomial. Assume that the origin is a locally asymptotically stable equilibrium point. This assumption is without loss of generality because state coordinates can always be redefined to shift an equilibrium point to the origin. The ROA is formally defined as:

$$\mathcal{R} := \left\{ x_0 \in \mathbb{R}^n :\ \text{If } x(0) = x_0 \text{ then } \lim_{t\to\infty} x(t) = 0 \right\} \tag{6.2}$$

Computing the exact ROA for nonlinear dynamical systems is very difficult. There has been significant research devoted to estimating invariant subsets of the ROA [6–12, 30, 31]. The approach taken in this paper is to restrict the search to ellipsoidal approximations of the ROA. Given an $n \times n$ matrix $N = N^T > 0$, define the shape function $p(x) := x^T N x$ and level set $\mathcal{E}_\beta := \{x \in \mathbb{R}^n \ :\ p(x) \leq \beta\}$. $p(x)$ defines the shape of the ellipsoid and β determines the size of the ellipsoid $\mathcal{E}_\beta$. The choice of p is problem dependent and reflects dimensional scaling information as well as the importance of certain directions in the state space. N can typically be chosen to be diagonal with $N_{i,i} := 1/x_{i,max}^2$. With this choice, $\mathcal{E}_{\beta=1}$ is a coordinate-aligned ellipsoid whose extreme points along the i^{th} state direction are $\pm x_{i,max}$. In this form, the level set value β provides an easily interpretable value for the size of the level set.

Given the shape function p, the problem is to find the largest ellipsoid $\mathcal{E}_\beta$ contained in the ROA:

$$\begin{aligned} \beta^* = &\max \beta \\ &\text{subject to: } \mathcal{E}_\beta \subset \mathcal{R} \end{aligned} \tag{6.3}$$

Determining the best ellipsoidal approximation to the ROA is still a challenging computational problem. Instead, lower and upper bounds for β^* satisfying $\underline{\beta} \leq \beta^* \leq \bar{\beta}$ are computed. If the lower and upper bounds are close then the largest ellipsoid level set, defined by Equation (6.3), has been approximately computed.

The upper bounds are computed via a search for initial conditions leading to divergent trajectories. If $\lim_{t\to\infty} x(t) = +\infty$ when starting from $x(0) = x_{0,div}$ then $x_{0,div} \notin \mathcal{R}$. If we define $\bar{\beta}_{div} := p(x_{0,div})$ then $\mathcal{E}_{\bar{\beta}_{div}} \not\subset \mathcal{R}$ which implies $\beta^* \leq \bar{\beta}_{div}$. An

exhaustive Monte Carlo search is used to find a tight upper bound on β^*. Specifically, random initial conditions are chosen starting on the boundary of a large ellipsoid: x_0 is chosen to satisfy $p(x_0) = \beta_{try}$ where β_{try} is sufficiently large that $\beta_{try} \gg \beta^*$. If a divergent trajectory is found, the initial condition is stored and an upper bound on β^* is computed. β_{try} is then decreased by a factor of 0.995 and the search continues until a maximum number of simulations is reached. There is a trade-off involved in choosing the factor 0.995. A smaller factor results in a larger reduction of the upper bound for each divergent trajectory but it typically limits the accuracy of the upper bound. No divergent trajectories can be found when $\beta_{try} < \beta^*$ and this roughly limits the upper bound accuracy to $\beta^*/(\text{factor})$. The value of 0.995 is very close to one and is chosen to obtain an accurate upper bound on β^*. $\bar{\beta}_{MC}$ will denote the smallest upper bound computed with this Monte Carlo search.

The lower bounds are computed using Lyapunov functions and recent results connecting sums-of-squares polynomials to semidefinite programming. Computing these bounds requires the vector field $f(x)$ in Equation (6.1) to be a polynomial function. A basic introduction to sum-of-squares optimizations is provided in Appendix A.3. The algorithm to compute a lower bound using sum-of-squares optimizations is briefly described here. Full algorithmic details are provided in the references [3–5, 32–35]. Lemma 1 is the main Lyapunov theorem used to compute lower bounds on β^*. This specific lemma is proved by [3] but very similar results are given in textbooks [29].

Lemma 1 *If there exists $\gamma > 0$ and a polynomial $V : \mathbb{R}^n \to \mathbb{R}$ such that:*

$$V(0) = 0 \text{ and } V(x) > 0 \ \forall x \neq 0 \tag{6.4}$$

$$\Omega_\gamma := \{x \in \mathbb{R}^n \ : \ V(x) \leq \gamma\} \text{ is bounded.} \tag{6.5}$$

$$\Omega_\gamma \subset \{x \in \mathbb{R}^n \ : \ \nabla V(x) f(x) < 0\} \cup \{0\} \tag{6.6}$$

then for all $x_0 \in \Omega_\gamma$, the solution of Equation (6.1) exists, satisfies $x(t) \in \Omega_\gamma$ for all $t \geq 0$, and $\Omega_\gamma \subset \mathcal{R}$.

A function V, satisfying the conditions in Lemma 1 is a Lyapunov function and Ω_γ provides an estimate of the region of attraction. If $x = 0$ is asymptotically stable, a linearization can be used to compute a Lyapunov function. Let $A := \frac{\partial f}{\partial x}\big|_{x=0}$ be the linearization of the dynamics about the origin and compute $P > 0$ that solves the Lyapunov equation $A^T P + PA = -I$. $V_{LIN}(x) := x^T P x$ is a quadratic Lyapunov

function that satisfies the conditions of Lemma 1 for sufficiently small $\gamma > 0$. V_{LIN} can be used to compute a lower bound on β^* by solving two maximizations:

$$\begin{aligned} \gamma^* := & \max \gamma \\ & \text{subject to: } \Omega_\gamma \subset \{x \in \mathbb{R}^n \ : \ \nabla V_{LIN}(x) f(x) < 0\} \end{aligned} \tag{6.7}$$

$$\begin{aligned} \underline{\beta} := & \max \beta \\ & \text{subject to: } \mathcal{E}_\beta \subset \Omega_{\gamma^*} \end{aligned} \tag{6.8}$$

The first maximization finds the largest level set Ω_{γ^*} of V_{LIN} such that Lemma 1 can be used to verify $\Omega_{\gamma^*} \subseteq \mathcal{R}$. The second maximization finds the largest ellipsoid $\mathcal{E}_{\underline{\beta}}$ contain within Ω_{γ^*}. The set containment constraints are replaced with a sufficient condition involving non-negative polynomials [3]. For example, $\mathcal{E}_\beta \subset \Omega_{\gamma^*}$ in Optimization (6.8) is replaced by

$$\begin{aligned} \underline{\beta} := & \max_{\beta,\ s(x)} \beta \\ & \text{subject to: } s(x) \geq 0 \ \forall x \\ & \qquad -(\beta - p(x))\, s(x) + (\gamma^* - V_{LIN}(x)) \geq 0 \ \forall x \end{aligned} \tag{6.9}$$

The function $s(x)$ is a decision variable of the optimization, i.e. it is found as part of the optimization. It is straight-forward to show that the two non-negativity conditions in Optimization (6.9) are a sufficient condition for the set containment condition in Optimization (6.8). If $s(x)$ is restricted to be a polynomial, both constraints involve the non-negativity of polynomial functions. A sufficient condition for a generic multivariate polynomial $h(x)$ to be non-negative is the existence of polynomials $\{g_1, \ldots, g_n\}$ such that $h = g_1^2 + \cdots + g_n^2$. A polynomial which can be decomposed in this way is called a sum-of-squares (SOS). Finally, if we replace the non-negativity conditions in Optimization (6.9) with SOS constraints, then we arrive at an SOS optimization problem:

$$\begin{aligned} \underline{\beta} := & \max \beta \\ & \text{subject to: } s(x) \text{ is SOS} \\ & \qquad -(\beta - p(x)) s(x) + (\gamma^* - V_{LIN}(x)) \text{ is SOS} \end{aligned} \tag{6.10}$$

There are connections between SOS polynomials and semidefinite matrices. Moreover, optimization problems involving SOS constraints can be converted and solved as a semidefinite programming optimization. Importantly, there is freely available software to set up and solve these problems [36–39]. $\underline{\beta}_{LIN}$ will denote the lower bound obtained from Optimization (6.10) using the quadratic Lyapunov function obtained from linearized analysis.

Unfortunately, $\underline{\beta}_{LIN}$ is usually orders of magnitude smaller than the upper bound $\bar{\beta}_{MC}$. Several methods to compute better Lyapunov functions exist, including V-s iterations [32–35], bilinear optimization [3], and the use of simulation data [4, 5]. In this paper, V-s iteration is used to compute the Lyapunov function and the inner ellipsoidal approximation to the ROA. The Lyapunov function $V(x)$ in the iteration is initialized with the linearized Lyapunov function V_{LIN}. The iteration also uses functions $l_1(x) = -\epsilon_1 x^T x$ and $l_2(x) = -\epsilon_2 x^T x$ where ϵ_1 and ϵ_2 are small positive constants on the order of 10^{-6}. The V-s iteration algorithm steps are:

1. $\underline{\gamma \textbf{ Step}}$: Hold V fixed and solve for s_2 and γ^*

$$\gamma^* := \max_{s_2 \in \text{SOS}, \gamma} \gamma \quad \text{s.t. } -(\gamma - V)s_2 - \left(\frac{\partial V}{\partial x} f + l_2\right) \in \text{SOS}$$

2. $\underline{\beta \textbf{ Step}}$: Hold V, γ^* fixed and solve for s_1 and $\underline{\beta}$

$$\underline{\beta} := \max_{s_1 \in \text{SOS}, \beta} \beta \quad \text{s.t. } -(\beta - p)s_1 + (\gamma^* - V) \in \text{SOS}$$

3. $\underline{V \textbf{ step}}$: Hold s_1, s_2, $\underline{\beta}$, γ^* fixed and solve for V satisfying:

$$\begin{aligned} &-(\gamma^* - V)s_2 - \left(\frac{\partial V}{\partial x} f + l_2\right) \in \text{SOS} \\ &-(\underline{\beta} - p)s_1 + (\gamma^* - V) \in \text{SOS} \\ &V - l_1 \in \text{SOS}, V(0) = 0 \end{aligned}$$

4. Repeat as long as the lower bound $\underline{\beta}$ continues to increase.

Software and additional documentation on the V-s iteration is provided at [39]. The basic issue is that searching for a Lyapunov function V results in a bilinear term Vs_2 in the γ constraint. This bilinear term can not be handled directly within the SOS programming framework because the constraints in SOS programs must be linear in

the decision variables. The $V - s$ iteration avoids the bilinearity in Vs_2 by holding either s_2 or V fixed. Each step of this iteration is a linear SOS optimization that can be solved with available software. In the V-s iteration, the Lyapunov functions are allowed to have polynomial degree greater than two. Increasing the degree of the Lyapunov function will improve the lower bound at the expense of computational complexity.

The V step requires additional discussion. An interior-point linear matrix inequality solver is used to find a feasible solution to the feasibility problem in the V step. The Lyapunov function V that is used in the γ and β steps will be feasible for the constraints in the V step. Thus it possible for the solver to simply return the same Lyapunov function that was used in the γ and β steps. While this is possible, it typically happens that the solver returns a different V that allows both γ and β to be increased at the next iteration. This step is informally justified by the fact that interior point solvers try to return a solution at the analytic center of set specified by the linear matrix inequality constraints. Thus the V step typically returns a feasible V that is "pushed away" from the constraints. A more formal theory for the behavior of this feasibility step is still an open question.

6.3 Polynomial Model Formulation & Validation of F/A-18 Aircraft

Section 6.2 described an approach to estimate regions of attraction for nonlinear systems. The approach to estimate lower bounds on the ROA relies on SOS optimization methods and can only be applied to polynomial systems. Moreover, the computational requirements for the SOS optimizations grow rapidly in the number of state variables and polynomial degree. This approximately limits this method to nonlinear analysis problems with at most 7-10 states and degree 3-5 polynomial models. Consequently, the construction of accurate, low-degree polynomial models is an important step in the proposed analysis process. This section formulates cubic degree polynomial models for the closed-loop systems consisting of the F/A-18 aircraft and the baseline and revised flight control laws.

6.3.1 Polynomial Model Formulation

A nine state, six DOF nonlinear model for the F/A-18 was described in Chapter 2. The phugoid mode of the aircraft involves the V and θ states. The phugoid mode is slow and is not important for capturing the falling leaf characteristics. The heading ψ does not impact any of other state dynamics and hence it can be neglected. Consequently a six state model of the F/A-18 aircraft is sufficient for analyzing the falling leaf mode. Additional rationale for neglecting (V, θ, ψ) is discussed in Section 5.1.

The mechanism to extract a six-state representation from the nine-state model is outlined. First, the nine-state model, Equation (2.1), is trimmed around a specific flight condition. Consider the flight condition for a coordinated turn ($\beta_t = 0^o$) at a 35^o bank angle and at $V_t = 350$ ft/s. The trim values are provided in Equation (6.11). The subscript 't' denotes a trim value.

$$\begin{bmatrix} \alpha_t \\ p_t \\ q_t \\ r_t \\ \theta_t \\ \psi_t \end{bmatrix} = \begin{bmatrix} 20.17^o \\ -1.083^o/s \\ 1.855^o/s \\ 2.634^o/s \\ 18.69^0 \\ 0^o \end{bmatrix}, \quad \begin{bmatrix} \delta_{stab,t} \\ \delta_{ail,t} \\ \delta_{rud,t} \\ \delta_{th,t} \end{bmatrix} = \begin{bmatrix} -4.449^o \\ -0.4383^o \\ -1.352^o \\ 14500 \text{ lbf} \end{bmatrix} \tag{6.11}$$

The analysis, presented in this paper, is performed around the flight condition mentioned in Equation (6.11). This flight condition is one of the eight different operating points, specifically Plant 4, around which linear analysis was performed in Chapter 5.

The states and inputs for the six-state model are defined relative to this trim point: $x_6 := [\beta - \beta_t,\ \alpha - \alpha_t,\ p - p_t,\ q - q_t,\ r - r_t,\ \phi - \phi_t]$ and $u_3 := [\delta_{ail} - \delta_{ail_t},\ \delta_{rud} - \delta_{rud_t},\ \delta_{stab} - \delta_{stab_t}]$. The state derivatives for the six state model, $\dot{x}_6$, are computed using Equation (2.3c), (2.3b), (2.4) and the first row ($\dot{\phi}$ entry) of (2.2), respectively. In these equations, V, θ, ψ and T are held fixed at their trimmed values. Moreover, these state derivatives are linear in the inputs. Thus the six-state model has the following form:

$$\dot{x}_6 = F(x_6) + G(x_6)u_3 \tag{6.12}$$

$$y = H(x_6) + J(x_6)u_3 \tag{6.13}$$

Figure 6.1 shows the structure of the closed-loop plant that is considered in this paper. P denotes the 6-state nonlinear model mentioned in Equation (6.12) and (6.13). K denotes either the baseline or revised control law presented in Section 4. Both the closed-loop models are formed with the negative feedback of the controller (K) around the nonlinear plant (P), as shown in Figure 6.1.

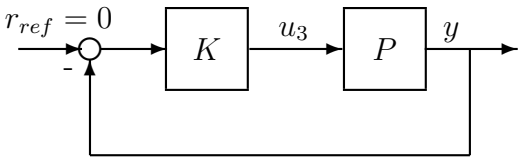

Figure 6.1: Feedback System

The autonomous ($r_{ref} = 0$) closed-loop dynamics are given by:

$$\frac{dx_{cl}}{dt} = \mathcal{F}(x_{cl}) \tag{6.14}$$

where $x_{cl} := [x_6^T,\ x_c]^T \in \mathbb{R}^7$ denotes the closed-loop states and $\mathcal{F}$ is given by Equation (6.15).

$$\mathcal{F} = \begin{bmatrix} F(x_6) - G(x_6)C_c x_c - G(x_6)D_c M(x_6)^{-1}(H(x_6) - J(x_6)C_c x_c) + G(x_6)u_{3_t} \\ A_c x_c + B_c M(x_6)^{-1}\left(H\left(x_6\right) - J\left(x_6\right)C_c x_c\right) \end{bmatrix} \tag{6.15}$$

where $M(x_6) = (I_l + J\left(x_6\right)D_c)$. l denotes the number of measurements in y.

The 7-state closed-loop model $\mathcal{F}$, in Equation (6.15), is nonlinear due to trigonometric terms, M^{-1}, and polynomial functions to model the aerodynamic coefficients. $\mathcal{F}$ can be approximated by a third degree polynomial function of x_{cl}. The approximation steps are as follows. First, the linearization of $\mathcal{F}$ is computed at $x_{cl} = 0$. Then $\mathcal{F}$ is expressed as $\mathcal{F} := \mathcal{F}_{lin}x_{cl} + \mathcal{F}_{nonl}(x_{cl})$ where $\mathcal{F}_{lin}$ denotes the linearization. Second, each entry of the vector-valued function $\mathcal{F}_{nonl}(x_{cl})$ is approximated by a polynomial consisting of second and third degree terms. The benefit of this procedure is that the polynomial model retains the same linearization as the original nonlinear model.

The polynomial approximation step exploits structure that exists in the nonlinear model. For example, p, q, r, and x_c typically enter linearly with nonlinear functions of α, β, and/or ϕ. To illustrate the point, lets consider the state-derivative

$\dot{\phi} = p + \tan\theta\,(q\sin\phi + r\cos\phi)$ from Equation 2.2. The value of θ is held at its trim value during approximation. Notice, q and r enters linearly with nonlinear functions of ϕ. By examining each state-derivative separately, some insight can be gained on the structure of the nonlinear model. The assumed structure of the polynomial approximation used in this paper is shown while presenting the approximated closed-loop polynomial model in Appendix A.4. This structure is used to determine the second and third degree terms to include in the polynomial functions. Then the coefficients of the polynomial functions are computed to approximate Equation (6.15) over a specified range of the closed-loop state-space. The range of the state space is chosen to be the seven dimensional hypercube in Table 6.1. The table provides the minimum and maximum deviations of each state from the trim point in Equation (6.11). Values are provided in degree for ease of interpretation. The hypercube is uniformly gridded along each dimension by the number of points specified in Table 6.1. This gridding results in a total of 60000 samples in the hypercube. The nonlinear function $\mathcal{F}_{nonl}$ is evaluated at these points and least squares is used to compute the polynomial coefficients that minimize the difference between $\mathcal{F}_{nonl}$ and the polynomial function at these 60000 samples. The approximation results in the following cubic degree polynomial model:

$$\dot{x}_{cl} = \mathcal{P}(x_{cl}) \tag{6.16}$$

$\mathcal{P}$ is provided in Appendix A.4 for both the baseline and the revised controller.

Table 6.1: State space hypercube data for constructing polynomial models

State	Range: [min max]	Sampled Data Points
β (deg)	$[-10^o\ 10^o]$	5
α (deg)	$[-25^o\ 25^o]$	6
p (deg/s)	$[-35^o\ 35^o/s]$	5
q (deg/s)	$[-30^o/s\ 30^o/s]$	5
r (deg/s)	$[-15^o/s\ 15^o/s]$	5
ϕ (deg)	$[-25^o\ 25^o]$	5
x_c (deg)	$[-20^o\ 20^o]$	4

6.3.2 Polynomial Model Validation

The cubic polynomial models for the baseline and revised control laws involve approximations due to neglecting three aircraft states and due to the polynomial least-squares

fits. It is important to determine if the cubic polynomial models are sufficiently accurate. This section compares the polynomial closed-loop models with closed-loop models constructed with the original nine-state nonlinear model (Equation (2.1)). The term "original model" will refer to the closed loop models constructed with the nine-state nonlinear model. Numerical tools do not exist to rigorously perform this comparison and hence the validation performed in this section will rely on heuristic procedures. However, the validation provides some confidence that the polynomial model provides, for engineering purposes, a sufficiently accurate approximation.

The first validation method is to compare the polynomial and original model by simulating from many initial conditions. Numerous simulations have been performed by perturbing the states from their trim values. Most state trajectories are similar for both the polynomial and original model. Figure 6.2 compares the polynomial and original models with the baseline control law. This specific simulation is performed by perturbing the $\beta,\ \alpha,\ p,\ q,\ r,\ \phi$ states by $5^0,\ 20^o,\ 25^o,\ 20^o/s,\ 20^o/s,\ 5^o/s$, respectively, from their trim points. For the original models, V, θ, and ψ are initialized to their trim values. The simulation results show that the polynomial model is in good agreement with the original model. Note, however, that the α trajectory for the polynomial model diverges from the original model as time progresses. This deviation is large (relative to other states) when the perturbation in the α state is large. However, the simulation comparisons show that the cubic degree polynomial model captures the dynamic characteristics of the original closed-loop model, even with such large perturbation in the initial condition. Figure 6.3 provides a similar comparison of the polynomial and original models with the revised control law. Similar results were obtained at many other simulation initial conditions. This indicates that the polynomial approximation accurately the closed-loop dynamics of the original nonlinear closed-loop model.

The second comparison method provides a statistical quantification on the accuracy of the polynomial model approximation. The closed-loop realization for either of the controllers can be generated by using Equation (6.15) based on the original nonlinear model. For a given control law, two different seven state realizations are developed: (i) $\mathcal{F}$, based on the original nonlinear model, and (ii) $\mathcal{P}$, a cubic degree polynomial approximation to $\mathcal{P}$. For this comparison, both the models are evaluated by sampling random points within the ellipsoid ${x_{cl}}^T N x_{cl} \leq \bar{\beta}$, where $\bar{\beta}$ is the upper bound of ROA estimation introduced in Section 6.2. The value of $\bar{\beta}$ for both the control

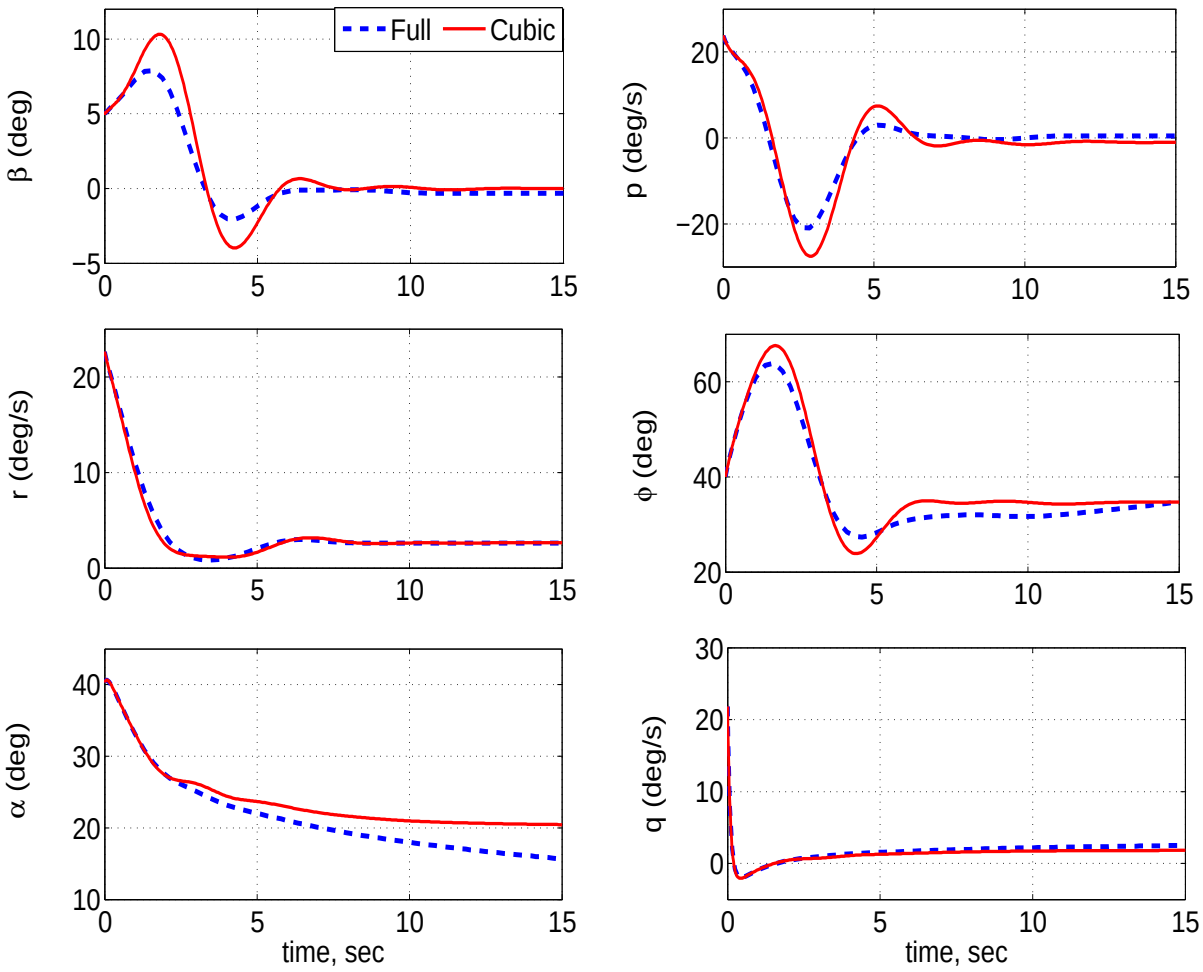

Figure 6.2: Baseline model: Simulation comparison between the original and approximated closed-loop baseline models due to initial perturbation in the states

law is estimated in Section 6.4.1. Moreover, the shape matrix N in the ellipsoid is presented in Equation (6.17). The relative weightings of the diagonal elements of N is determined by the physical operating range of the states around the trim point specified. In other words, the shape matrix roughly scales each state by the maximum magnitude observed during the flight conditions. The maximum magnitude is chosen to be the range of states over which the least squares is performed, as mentioned in Table 6.1. For ease of interpretation, the shape matrix is also provided in units of degree or degree/sec. However, the computation is performed using the radian

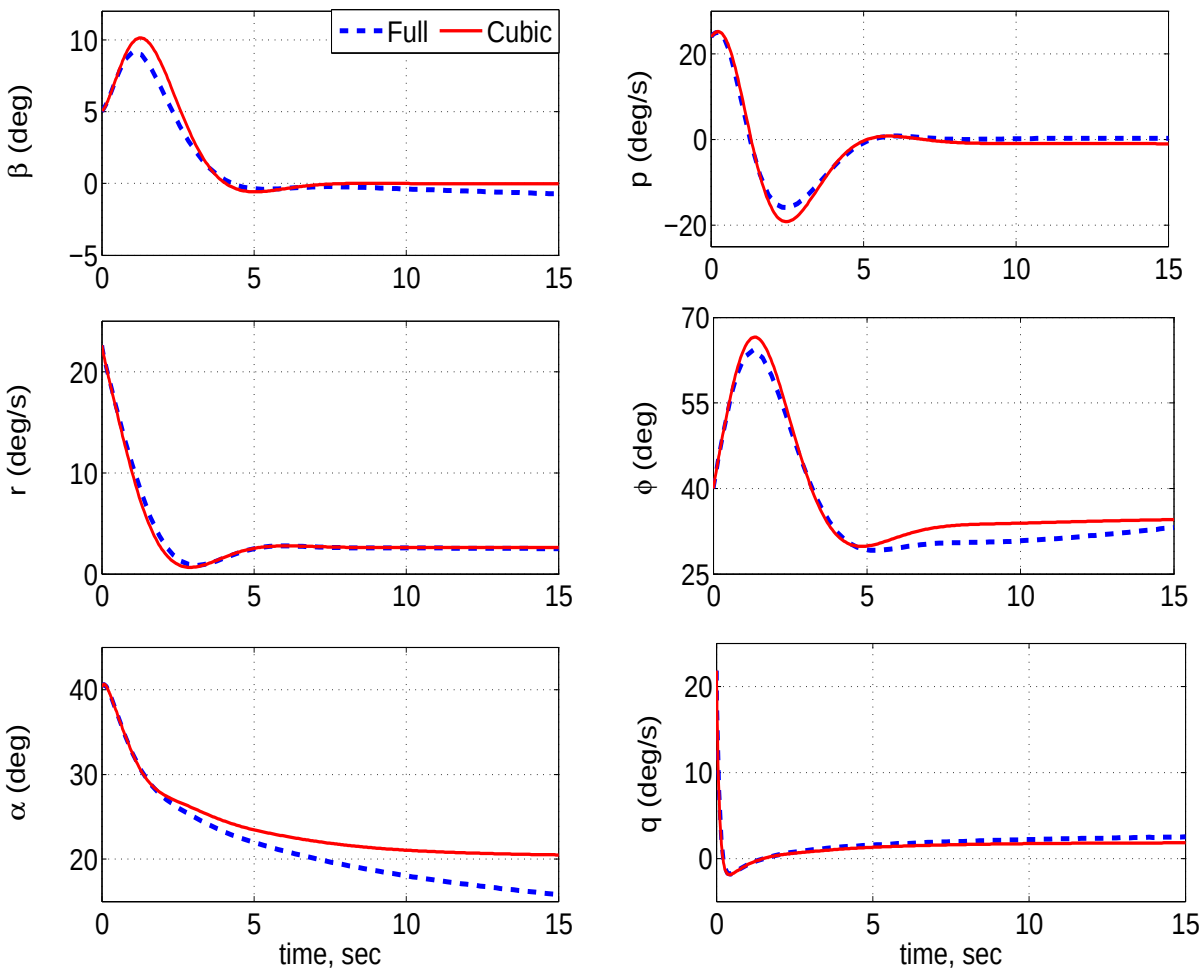

Figure 6.3: Revised model: Simulation comparison between the original and approximated closed-loop revised models due to initial perturbation in the states

representation of N.

$$N := diag(0.1745 \text{ rad}, 0.4363 \text{ rad}, 0.6109 \text{ rad/s}, 0.5236 \text{ rad/s}, 0.2618 \text{ rad/s}, 0.4363 \text{ rad}, 0.3491 \text{ rad})^{-2} \quad (6.17)$$

$$:= diag(10^o, 25^o, 35^o/s, 30^o/s, 15^o/s, 25^o, 20^o)^{-2} \quad (6.18)$$

Now, define relative error $:= \frac{||(\mathcal{F}|_{x_i} - \mathcal{P}|_{x_i})||_2}{||\mathcal{F}|_{x_i}||_2}$, where $x_i \in R^{7\times 1}$ satisfies ${x_i}^T N x_i \leq \bar{\beta}$. The relative error, evaluated within the ellipsoid, defines a metric on the notion of how 'close' the approximated model is to the original model. The relative error for the baseline control law is computed at 30,000 different $x_i \in R^{7\times 1}$ within the ellipsoid

${x_i}^T N x_i \leq 2.3$. Note, $\bar{\beta} = 2.3$ is taken from Section 6.4.1. The approximation incurs less than 10% relative error on 88% of the 30,000 points. Similarly, the relative error for the revised control law is also computed at 30,000 different points within the ellipsoid ${x_i}^T N x_i \leq 5.9$. In this case, the approximation incurs less than 10% relative error on approximately 90% of the 30,000 points. Moreover, for both the control laws, the spread of the relative error is also more or less uniform as the approximated models deviate away from the trim point. Figure 6.4 and 6.5 show the spread of this relative error of the approximation for using the baseline and the revised control law, respectively. The x-axis indicates the size of the ellipsoid, ${x_{cl}}^T N x_{cl}$. The origin indicates the trim point of the model.

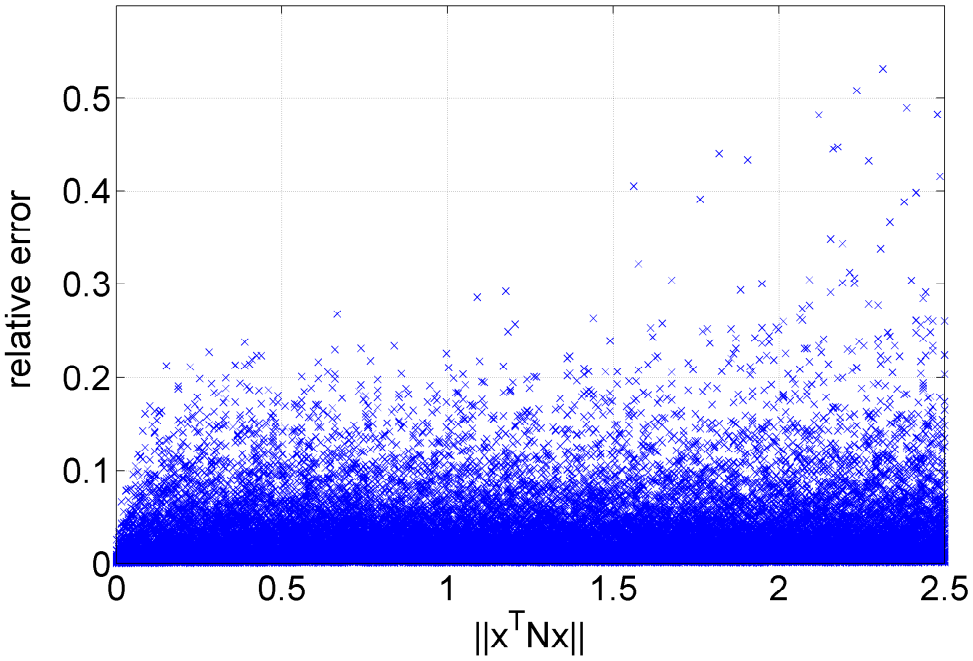

Figure 6.4: Baseline model approximation: The size (Eucledian 2-norm) of the relative error between the original baseline model and the approximated model as the approximated model deviates away from the trim point

Both these validation procedure is heuristic but it is still an open problem to develop rigorous and computable metrics of the approximation error between a generic nonlinear (non-analytic) model and a polynomial model. However, these approaches provide some confidence that the developed polynomial model has captured the dynamic characteristics of the original model, for all engineering purposes.

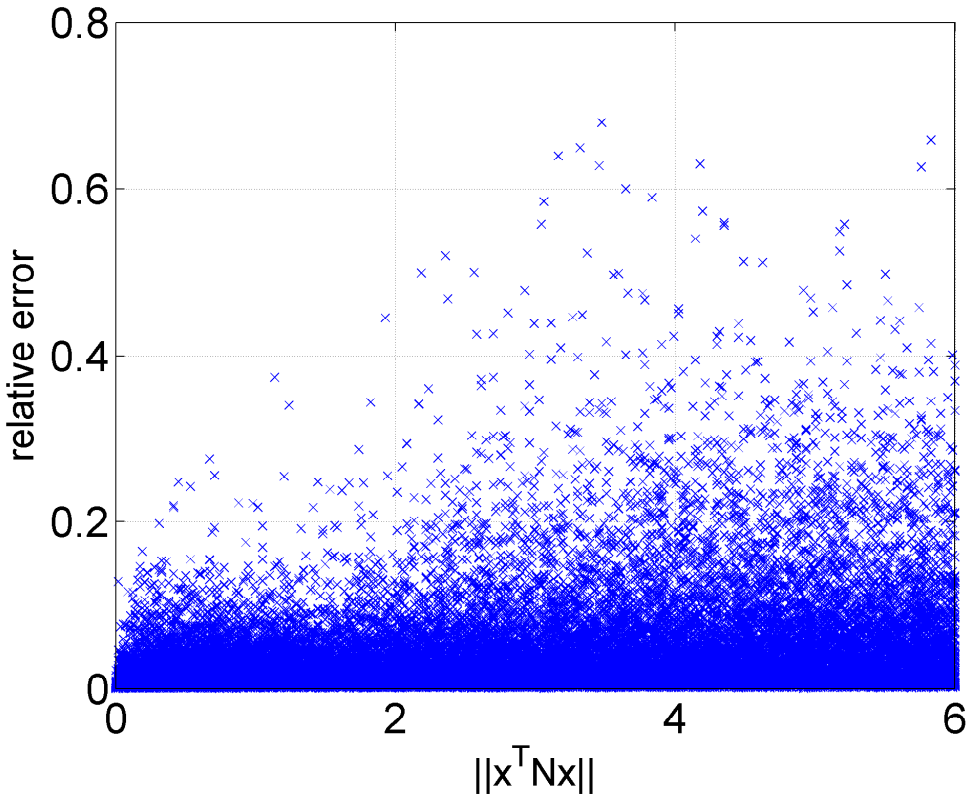

Figure 6.5: Revised model approximation: The size (Eucledian 2-norm) of the relative error between the original revised model and the approximated model as the approximated model deviates away from the trim point

6.4 Nonlinear Analysis

Extensive linear analyses has been performed to compare the robustness properties of the closed loop systems with the baseline and revised flight control laws in Chapter 5. Both the controllers yield similar gain and phase margins, while some of the μ analyses indicated that the revised design has better robustness properties than the baseline. However, linear analysis is only valid within a small region around the operating point and this is generally insufficient for analyzing nonlinear phenomenon like the falling leaf motion. This section applies the nonlinear ROA estimation (described in Section 6.2) method to compare the robustness properties of both flight control laws. The analyses are performed for the operating point mentioned in Equation (6.11) using the cubic polynomial closed-loop models developed in Section 6.3.

6.4.1 Estimation of Upper Bound on ROA

The Monte Carlo search, described in Section 6.2, is used to estimate ROA upper bounds $\bar{\beta}$ for both flight control laws. The Monte Carlo search was performed with a maximum of 2 million simulations each for the baseline and revised control laws. The search returns an initial condition x_0 on the boundary of the ellipsoid, i.e. $p(x_0) = x_0^T N x_0 = \bar{\beta}_{MC}$, that causes the system to go unstable. Hence, the value of the $\bar{\beta}_{MC}$ provides an upper bound of the ROA for the F/A-18 aircraft. Recall that the shape matrix N is defined in Equation (6.17). The baseline control law provides an upper bound of $\bar{\beta}_{MC} = 2.298$ whereas the revised control law provides an upper bound of $\bar{\beta}_{MC} = 5.836$.

The Monte Carlo search returned the following initial condition for the closed system with the baseline control law:

$$x_0 = [-5.632^o,\ -33.54^o/s,\ 7.908^o/s,\ 0.6103^o,\ 3.959^o,\ 6.107^o/s,\ 0.06820^o]^T$$

This initial condition satisfies $p(x_0) = 2.298$. Figure 6.6 shows the unstable response of the baseline system resulting from this initial condition. Decreasing the initial condition slightly to $0.995x_0$ leads to a stable response.

For the revised control law the Monte Carlo search returned the following initial condition:

$$x_0 = [3.841^o,\ 54.25^o/s,\ 8.705^o/s,\ 29.45^o,\ 1.641^o,\ 0.630^o/s,\ 0.7880^o]^T$$

This initial condition satisfies $p(x_0) = 5.895$ and Figure 6.7 shows the unstable response of the revised system resulting from this initial condition. Again, a stable initial condition is obtained by slightly decreasing the initial condition to $0.995x_0$.

6.4.2 Estimation of Lower Bound on ROA

The V-s iteration, described in Section 6.2 is employed to estimate the ROA lower bounds $\underline{\beta}$ for both the F/A-18 flight control laws. Recall, $N = N^T$ indicates the shape matrix of ellipsoid and is determined by the physical operating range of the states around the trim point specified. N is provided by Equation (6.17). The ellipsoid, $x_{cl}^T N x_{cl} = \underline{\beta}$, defines the set of initial conditions for which the control law will bring the aircraft back to its trim point. The state corresponding to the smaller

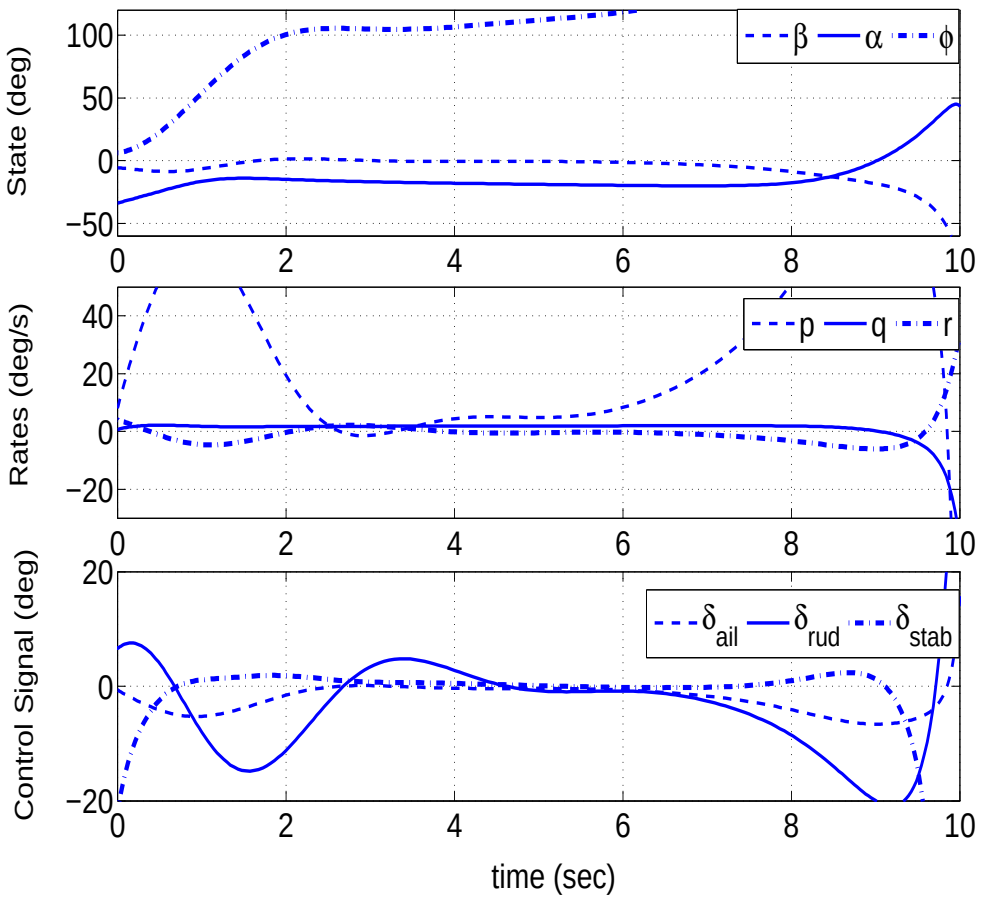

Figure 6.6: Unstable trajectories for Baseline control law with IC s.t. $x_o^T N x_o = 2.298$

diagonal element of N is expected to have a wide range of variation in estimating the region of attraction. If the aircraft is perturbed due to a wind gust or other upset condition but remains in the ellipsoid then the control law will recover the aircraft and bring it back to trim. In other words the ellipsoid defines a safe flight envelope for the F/A-18. Hence, the ROA provides a measure of how much perturbation the aircraft can tolerate before it becomes unstable. Roughly, the value of the $\underline{\beta}$ can be thought of as 'nonlinear stability margin', similar to the linear stability margin (k_m) concept presented in the linear analysis. However, these two margins are not directly comparable to each other.

Increasing the degree of the Lyapunov function improves the lower bound estimate of the ROA as discussed in Section 6.2. At first, bounds using the quadratic Lyapunov function from linearized analysis, denoted as $\underline{\beta}_{LIN}$, are computed. This method has been proposed for validation of flight control laws [1]. The baseline flight control law

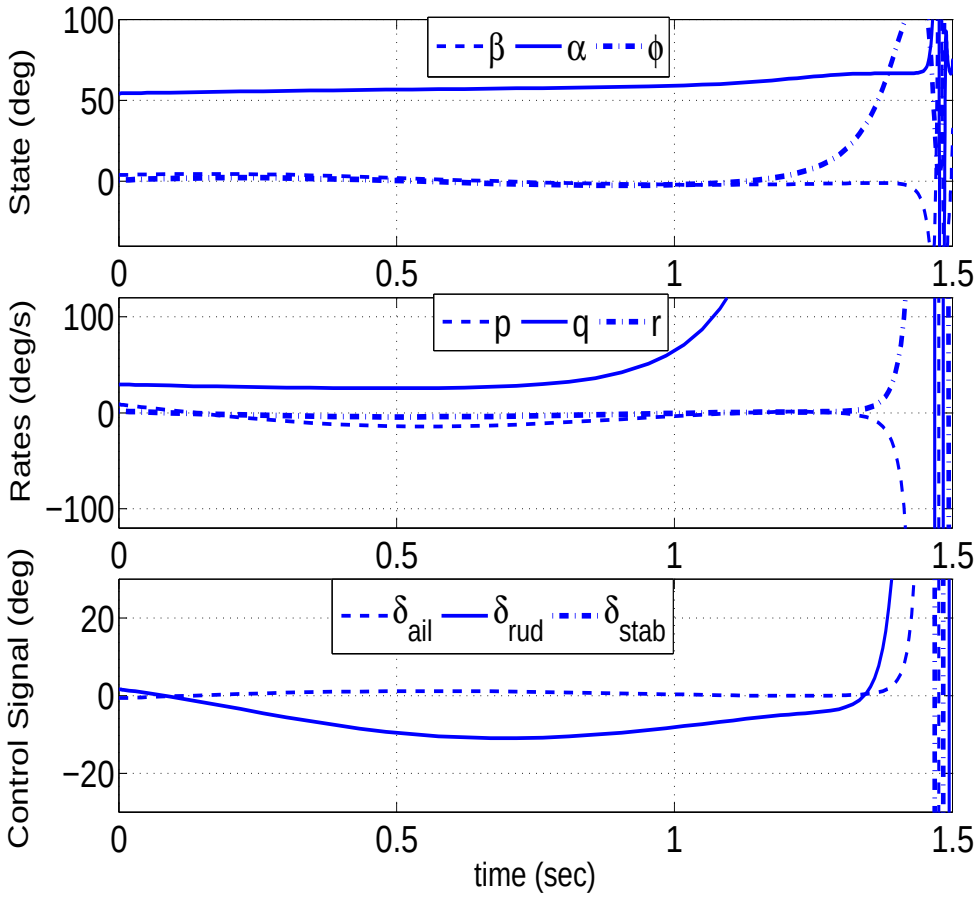

Figure 6.7: Unstable trajectories for Revised control law with IC s.t. $x_o^T N x_o = 5.895$

achieves a bound of $\underline{\beta}_{LIN} = 5.100 \times 10^{-3}$ while the revised achieves $\underline{\beta}_{LIN} = 8.200 \times 10^{-3}$. Recall, the upper bound estimation, $\bar{\beta}_{MC}$, of the ROA is 2.298 for baseline and 5.895 for the revised flight control law. These lower bounds are not particularly useful since they are three orders of magnitude smaller than the corresponding upper bounds. The estimate of the lower bound needs to be improved. Hence, the V-s iteration with quadratic and quartic Lyapunov functions are used to increase the lower bound estimate.

The V-s iteration with quadratic Lyapunov functions gives $\underline{\beta}_2 = 0.8921$ for the baseline control law and $\underline{\beta}_2 = 3.719$ for the revised control law. The lower bound estimation has improved compared to the linearized Lyapunov analysis. However, the estimation can be further improved by using quartic Lyapunov function. The V-s iteration with quartic Lyapunov functions is $\underline{\beta}_4 = 2.006$ for the baseline control law and $\underline{\beta}_4 = 4.299$ for the revised control law. These bounds are significantly larger than

the bounds obtained for the linearized Lyapunov function. A sixth order Lyapunov function can lead to improved lower bounds but with a significant increase in computation time. The lower bounds with different degree of Lyapunov function show that the linearized ROA method is much more conservative than the results obtained using the quartic Lyapunov function.

6.4.3 Discussion

The largest ellipsoid contained in the region of attraction is denoted as $\mathcal{E}_{\beta^*} := \{x_{cl} \in \mathbb{R}^7 \ : \ x_{cl}^T N x_{cl} \leq \beta^*\}$. The lower and upper bounds on β^* have been computed for the closed-loop systems with both F/A-18 flight control laws. The bounds on β^* for the baseline control law are: $2.006 \leq \beta^* \leq 2.298$. For the revised control law the bounds are: $4.299 \leq x_{cl}^T N x_{cl} \leq 5.895$. These bounds on the ROA can be visualized by plotting slices of the ellipsoid $x_{cl}^T N x_{cl}$. Figure 6.8 and 6.9 show slices of both the inner/outer approximations of the best ellipsoidal ROA approximation for both the flight control laws, respectively in α-β and p-r planes. These states are chosen since they play an important role in characterizing the falling leaf motion. In both the figures, the solid lines show the slices of the inner bounds obtained from quartic Lyapunov analysis. Every initial condition within the solid ellipses will return to the trim condition (marked as a '+'). If the aircraft is perturbed due to an upset condition or wind gust but remains within this ellipsoid then the control law will recover the aircraft and bring it back to trim. The dashed lines show the slices of the outer bounds obtained from Monte Carlo analysis. There is at least one initial condition on the outer ellipsoid which leads to a divergent trajectory. The ellipsoid is seven dimensional and hence the initial condition leading to a divergent trajectory does not necessarily lie on the slice of the ellipsoid shown in the figure. Upset conditions that push the aircraft state to this upper bound ellipsoid could potentially lead to loss of control.

The closeness of these upper/lower bounds indicate that the best ellipsoidal ROA approximation problem has been solved for engineering purposes. Hence, definitive conclusions regarding the stability region about the flight control laws can be drawn for the F/A-18 aircraft. The slices for the quartic Lyapunov functions demonstrate that the ROA estimate for the revised control law is larger than the one for the baseline control law. For example, from the α-β slice it can be concluded that the baseline controller returns to the trim condition for initial perturbations in an ellipse defined by

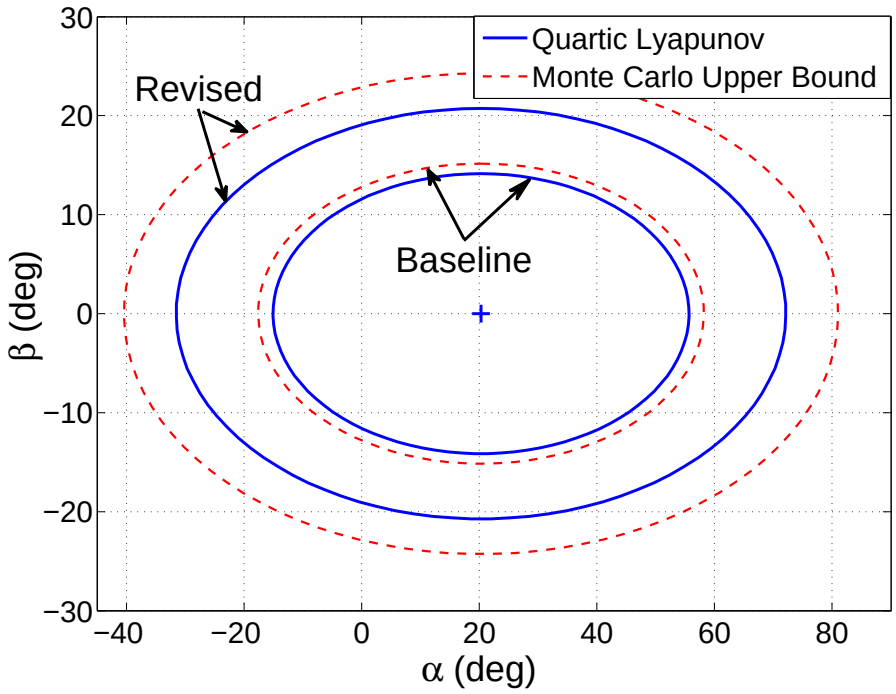

Figure 6.8: Lower / upper bound slices for ROA estimate in $\alpha - \beta$ plane. The lower bound estimate is based on the quartic Lyapunov function.

β between (approximately) -14^o and $+14^o$ and α between (approximately) -15 and $+55^o$. The revised controller returns to the trim condition for initial perturbations in an ellipse defined by β between -21^o and $+21^o$ and α between -32^o and $+72^o$. It is important to note that, the revised controller is better able to damp out the sideslip motion and consequently, increasing the dutch-roll damping. It has been shown that increased dutch-roll damping due to the revised flight control law architecture is one of the key reasons to suppress the falling leaf motion [2]. Figure 6.8 shows that the sideslip damping has significantly improved in the revised flight control law compared to the baseline design. The revised flight control law also increases the stability region in other directions. Moreover, the aircraft also achieves an increased stability region along the angle-of-attack direction with the revised design. Overall, the suppression of the falling leaf can be attributed to the larger stability region provided by the revised flight control law.

In fact, the robustness improvement for the revised controller is more dramatic if the volume of the ROA estimate is considered. The volume of the ellipsoid $\mathcal{E}_\beta$ is proportional to $\beta^{(n/2)}$ where $n = 7$ is the state dimension. Thus the ROA estimate

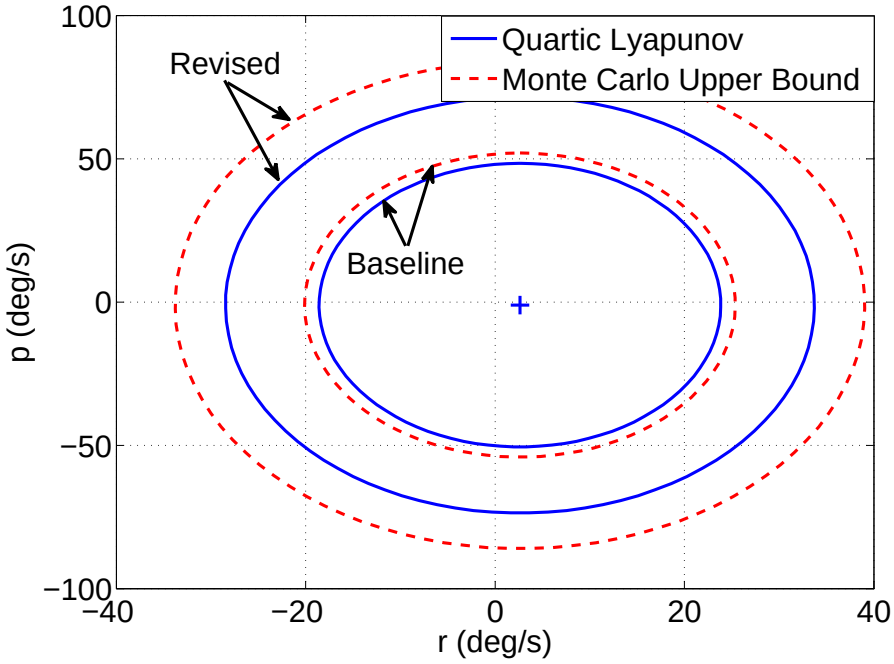

Figure 6.9: Lower / upper bound slices for ROA estimate in $p - r$. The lower bound estimate is based on the quartic Lyapunov function.

obtained by the revised control law has a volume which is $(\underline{\beta}_{4,rev}/\underline{\beta}_{4,base})^{3.5}$ greater than that obtained by the baseline design. This corresponds to a volume increase of 14.3 for the revised flight control law. This is a significant increase in the stability region. Thus information from these two ellipsoids can be used to draw conclusions about the safe flight envelope. The size of these ellipsoids measure the robustness of the flight control law to disturbances. In summary, the ellipsoids define a metric for the safe flight envelope of the F/A-18 aircraft. Based on this metric, the revised control law has an increased safe flight envelope, which helps suppressing the falling leaf motion.

The nonlinear analysis imposes a limitation that the dynamics of the aircraft need to be described by the polynomial functions of the states. Hence, the caveat with this nonlinear analysis results is that the size of the ROA may be larger than where the polynomial model is valid. Due to the approximation procedure, the approximated polynomial model deviates from the original model away from the trim points. As a cross-validation, both the approximated and the original model are simulated by sampling the initial conditions on the ellipsoid ${x_{cl}}^T N x_{cl} = \bar{\beta}$. Numerous simulation

comparisons revealed that both the models' state trajectories are in good agreement, in light of the discussion of Section 6.3.2. Moreover, the heuristic statistical method of model validation, performed in Section 6.3.2, also provides some confidence on the validity of the approximated model on the boundary of the outer ellipsoidal approximation.

The computation required for all bounds is summarized in Table 6.2. The quartic Lyapunov functions provided much better lower bounds than the quadratic Lyapunov functions. However, computing bounds with quartic Lyapunov functions required significantly more time than computing bounds with quadratic Lyapunov functions. This is due to the computational growth of SOS optimizations due to an increase in the degree of the polynomial model. Increasing the state dimension, e.g. by including the V and θ states, also would result in a large increase in computation for the lower bounds. The computation times for the Monte Carlo upper bounds were significantly longer than the times for the lower bounds. However, similar upper bounds can be obtained with fewer Monte Carlo simulations. Note, the analyses are performed on *Intel(R) Core(TM) i7 CPU 2.67GHz 8.00GB RAM.*

Table 6.2: Computational time for performing ROA analysis

Analysis	Lyapunov Order	Iteration Steps	**Baseline**	**Revised**
Lower Bound	4^{th}	80	7.935 Hrs	7.365 Hrs
Lower Bound	2^{nd}	40	0.113 Hrs	0.111 Hrs
Lower Bound Linear Dynamics	4^{th}	40	0.00340 Hrs	0.00440 Hrs
Upper Bound		2 million	80 Hrs	80 Hrs

Chapter 7

Conclusion

This chapter summarizes the main contribution of the thesis and outline some directions of future research. Moreover, the MATLAB codes for generating the models and results presented in this thesis are available in:
http://www.aem.umn.edu/ AerospaceControl/.

7.1 Summary

The thesis has developed a nonlinear simulation model of the F/A-18 aircraft. All required data, including aerodynamic data and physical parameters, to construct the F/A-18 nonlinear simulation model are presented in this thesis.

Extensive linear robustness analyses have been performed in Chapter 5. Classical gain and phase margin analyses indicate that the revised flight control law has similar robustness properties as the baseline flight control law. More advanced linear analysis tools, such as μ and worst-case performance, indicate that the revised flight controller has noticeably better robustness properties than the baseline control law.

Chapter 6 estimates bounds on the regions of attraction for two F/A flight control laws. These bounds establish 'nonlinear robustness' metric and provide useful information in validating and verifying the flight control laws' susceptibility to the falling leaf motion. Upper bounds were estimated using Monte Carlo simulations and lower bounds were estimated using sum of squares optimization. It is important to note that the ROA analysis accounts for significant nonlinearities in the F/A-18 aircraft

dynamics. This makes the analysis more applicable to nonlinear flight phenomenon such as the falling leaf mode. The conclusion of this analysis is that the revised F/A-18 flight control law has a significantly larger region of attraction than the baseline control law. This nonlinear analysis indicates that revised control law is less susceptible to to a loss of control phenomenon like the falling leaf mode. In addition, a general and systematic way of approximating the nonlinear F/A-18 aircraft dynamics by polynomial vector fields is also proposed. The approximation method can be applied to other aircraft dynamics without loss of generality. Moreover, some heuristic validation procedures are also mentioned to ensure that the approximation procedure captures the dynamic characteristics of the original nonlinear model.

7.2 Future Research

The main future direction of research is oriented towards overcoming the limitations imposed by using the polynomial SOS optimization technique to estimate the ROA. The ROA estimation procedure presented in Chapter 6 does not handle hard nonlinearities like actuator saturation. Actuator saturation can impose serious limitations in control design process. Hence, estimating ROA without information about actuator saturation can potentially validate flight control law up to region which may not even be physically reachable. Consequently, ignoring the actuator saturation may raise a source of concern during the validation stage of the flight control law.

Another direction of research can be envisioned by realizing that suitable metric for comparing two different nonlinear models are yet to be developed. The ROA estimation can only be applied to dynamics that are described by polynomial vector fields. In reality, the actual flight dynamics are never described by polynomial model. This enforces the analyst to perform polynomial approximation to the original dynamics. Being able to compare the 'closeness' of the approximated polynomial model to the original model provide the analyst some confidence that the ROA estimation is meaningful. Hence, developing suitable metric for formalizing the notion of 'closeness' between two different nonlinear models is another source of future research.

Moreover, the proposed ROA estimation technique is computationally intensive. A drawback is that the size of the optimization problem grows rapidly if the SOS optimization involves polynomials with many variables and/or high degree. Hence, further investigation is required to reduce the computational cost of the SOS technique to handle larger (more than 7 states) system.

Bibliography

[1] Heller, M., Niewoehner, R., and Lawson, P. K., "On the Validation of Safety Critical Aircraft Systems, Part I: An Overview of Analytical & Simulation Methods," *AIAA Guidance, Navigation, and Control Conference*, No. AIAA 2003-5559, 2003.

[2] Heller, M., David, R., and Holmberg, J., "Falling leaf motion suppression in the F/A-18 Hornet with revised flight control software," *AIAA Aerospace Sciences Meeting*, No. AIAA-2004-542, 2004.

[3] Tan, W., *Nonlinear Control Analysis and Synthesis using Sum-of-Squares Programming*, Ph.D. thesis, University of California, Berkeley, 2006.

[4] Topcu, U., Packard, A., Seiler, P., and Wheeler, T., "Stability region analysis using simulations and sum-of-squares programming," *Proceedings of the American Control Conference*, 2007, pp. 6009–6014.

[5] Topcu, U., Packard, A., and Seiler, P., "Local stability analysis using simulations and sum-of-Squares programming," *Automatica*, Vol. 44, No. 10, 2008, pp. 2669–2675.

[6] Chiang, H.-D. and Thorp, J., "Stability regions of nonlinear dynamical systems: A constructive methodology," *IEEE Transactions on Automatic Control*, Vol. 34, No. 12, 1989, pp. 1229–1241.

[7] Davison, E. and Kurak, E., "A computational method for determining quadratic Lyapunov functions for nonlinear systems," *Automatica*, Vol. 7, 1971, pp. 627–636.

[8] Genesio, R., Tartaglia, M., and Vicino, A., "On the estimation of asymptotic stability regions: State of the art and new proposals," *IEEE Transactions on Automatic Control*, Vol. 30, No. 8, 1985, pp. 747–755.

[9] Tibken, B., "Estimation of the domain of attraction for polynomial systems via LMIs," *Proceedings of the IEEE Conference on Decision and Control*, 2000, pp. 3860–3864.

[10] Tibken, B. and Fan, Y., "Computing the domain of attraction for polynomial systems via BMI optimization methods," *Proceedings of the American Control Conference*, 2006, pp. 117–122.

[11] Vannelli, A. and Vidyasagar, M., "Maximal Lyapunov functions and domains of attraction for autonomous nonlinear systems," *Automatica*, Vol. 21, No. 1, 1985, pp. 69–80.

[12] Parrilo, P., *Structured Semidefinite Programs and Semialgebraic Geometry Methods in Robustness and Optimization*, Ph.D. thesis, California Institute of Technology, 2000.

[13] Napolitano, M. R., Paris, A. C., and Seanor, B. A., "Estimation of the longitudinal aerodynamic parameters from flight data for the NASA F/A-18 HARV," *AIAA Atmospheric Flight Mechanics Conference*, No. AIAA-96-3419-CP, 1996, pp. 469–478.

[14] Napolitano, M. R., Paris, A. C., and Seanor, B. A., "Estimation of the lateral-directional aerodynamic parameters from flight data for the NASA F/A-18 HARV," *AIAA Atmospheric Flight Mechanics Conference*, No. AIAA-96-3420-CP, 1996, pp. 479–489.

[15] Lluch, C. D., *Analysis of the Out-of-Control Falling Leaf Motion using a Rotational Axis Coordinate System*, Master's thesis, Virginia Polytechnic Institue and State Unniversity, 1998.

[16] Iliff, K. W. and Wang, K.-S. C., "Extraction of lateral-directional stability and control derivatives for the basic F-18 aircraft at high angles of attack," *NASA TM-4786*, 1997.

[17] Napolitano, M. R. and Spagnuolo, J. M., "Determination of the stability and control derivatives of the NASA F/A-18 HARV using flight data," Tech. rep., NASA, 1993.

[18] Carter, B. R., *Time optimization of high performance combat maneuvers*, Master's thesis, Naval Postgraduate School, 2005.

[19] Buttrill, S. B., Arbuckle, P. D., and Hoffler, K. D., "Simulation model of a twin-tail, high performance airplane," Tech. Rep. NASA TM-107601, NASA, 1992.

[20] Stengel, R., *Flight Dynamics*, Princeton University Press, 2004.

[21] Cook, M., *Flight Dynamics Principles*, Wiley, 1997.

[22] Illif, K. W. and Wang, K.-S. C., "Retrospective and recent examples of aircraft parameter identification at NASA Dryden Flight Research Center," *Journal of Aircraft*, Vol. 41, No. 4, 2004.

[23] Foster, J. V., 2009.

[24] Stevens, B. and Lewis, F., *Aircraft Control and Simulaion*, John Wiley & Sons, 1992.

[25] Jaramillo, P. T. and Ralston, J. N., "Simulation of the F/A-18D falling leaf," *AIAA Atmospheric Flight Mechanics Conference*, 1996, pp. 756–766.

[26] Heller, M., Niewoehner, R., and Lawson, P. K., "High angle of attack control law development and testing for the F/A-18E/F Super Hornet," *AIAA Guidance, Navigation, and Control Conference*, No. AIAA-1999-4051, 1999, pp. 541–551.

[27] Balas, G., Chiang, R., Packard, A., and Safonov, M., *Robust Control Toolbox*, MathWorks, 2008.

[28] Khalil, H., *Nonlinear Systems*, Prentice Hall, 2nd ed., 1996.

[29] Vidyasagar, M., *Nonlinear Systems Analysis*, Prentice Hall, 2nd ed., 1993.

[30] Hauser, J. and Lai, M., "Estimating quadratic stability domains by nonsmooth optimization," *Proceedings of the American Control Conference*, 1992, pp. 571–576.

[31] Hachicho, O. and Tibken, B., "Estimating domains of attraction of a class of nonlinear dynamical systems with LMI methods based on the theory of moments," *Proceedings of the IEEE Conference on Decision and Control*, 2002, pp. 3150–3155.

[32] Jarvis-Wloszek, Z., *Lyapunov Based Analysis and Controller Synthesis for Polynomial Systems using Sum-of-Squares Optimization*, Ph.D. thesis, University of California, Berkeley, 2003.

[33] Jarvis-Wloszek, Z., Feeley, R., Tan, W., Sun, K., and Packard, A., "Some Controls Applications of Sum of Squares Programming," *Proceedings of the 42nd IEEE Conference on Decision and Control*, Vol. 5, 2003, pp. 4676–4681.

[34] Tan, W. and Packard, A., "Searching for control Lyapunov functions using sums of squares programming," *42nd Annual Allerton Conference on Communications, Control and Computing*, 2004, pp. 210–219.

[35] Jarvis-Wloszek, Z., Feeley, R., Tan, W., Sun, K., and Packard, A., *Positive Polynomials in Control*, Vol. 312 of *Lecture Notes in Control and Information Sciences*, chap. Controls Applications of Sum of Squares Programming, Springer-Verlag, 2005, pp. 3–22.

[36] Prajna, S., Papachristodoulou, A., Seiler, P., and Parrilo, P. A., *SOSTOOLS: Sum of squares optimization toolbox for MATLAB*, 2004.

[37] Lofberg, J., "YALMIP : A Toolbox for Modeling and Optimization in MATLAB," *Proceedings of the CACSD Conference*, Taipei, Taiwan, 2004.

[38] Sturm, J., "Using SeDuMi 1.02, a MATLAB toolbox for optimization over symmetric cones," *Optimization Methods and Software*, 1999, pp. 625–653.

[39] Balas, G., Packard, A., Seiler, P., and Topcu, U., "Robustness Analysis of Nonlinear Systems," http://www.aem.umn.edu/ AerospaceControl/.

[40] Iliff, K. W. and Wang, K.-S. C., "Flight-Determined Subsonic Longitudinal Stability and Control Derivatives of the F-18 High Angle of Attack Research Vehicle (HARV) With Thrust Vectoring," *NASA/TP-97-206539*, 1997.

[41] Parrilo, P., "Semidefinite programming relaxations for semialgebraic problems," *Mathematical Programming Ser. B*, Vol. 96, No. 2, 2003, pp. 293–320.

[42] Lasserre, J., "Global Optimization with Polynomials and the Problem of Moments," *SIAM Journal on Optimization*, Vol. 11, No. 3, 2001, pp. 796–817.

[43] Sturm, J., "SeDuMi version 1.05," http://fewcal.kub.nl/sturm/software/sedumi.html, 2001.

[44] Gatermann, K. and Parrilo, P., "Symmetry groups, semidefinite programs, and sums of squares," *Journal of Pure and Applied Algebra*, Vol. 192, 2004, pp. 95–128.

Appendix A

Appendices

A.1 F/A-18 Full Aerodynamic Model

The aerodynamic coefficients presented in this section have been extracted from various papers [13–18]. The aerodynamic model of the aircraft is presented as closed-form expression. Note that due to lack of data in low angle-of-attack ($0^o \leq \alpha \leq 10^o$), artificial data have been introduced to ensure realistic fit for estimating the closed-form expression of the aerodynamic coefficients. Plots of the coefficients' least-square fit are also presented.

A.1.1 Pitching Moment Coefficient, C_m

Pitching moment coefficients have been extracted from [40]. The pitching moment coefficient is modeled for the contribution from: (i) the bare airframe, (ii) stabilator deflection as a function of α, and (iii) pitch damping derivative as a function of α. Equation A.1 and Table A.1 describes the pitching moment coefficient used in this thesis.

$$C_m = \left(C_{m_{\alpha_2}}\alpha^2 + C_{m_{\alpha_1}}\alpha + C_{m_{\alpha_0}}\right) + \left(C_{m_{\delta_{stab_2}}}\alpha^2 + C_{m_{\delta_{stab_1}}}\alpha + C_{m_{\delta_{stab_0}}}\right)\delta_{stab} + \frac{\bar{c}}{2V}\left(C_{m_{q_3}}\alpha^3 + C_{m_{q_2}}\alpha^2 + C_{m_{q_1}}\alpha + C_{m_{q_0}}\right)q \tag{A.1}$$

Figure A.1 and A.2 show the plot of the pitching moment coefficient for the above three different effects. Note, artificial data (marked as square box) have been included to ensure a realistic fit at low α. Below 10^o angle-of-attack, the coefficients do not

Table A.1: Pitching Moment Coefficient Data

Bareframe Coefficient			Control Derivatives			Damping Derivative		
$C_{m_{\alpha_2}}$	=	-1.2897	$C_{m_{\delta_{stab_2}}}$	=	0.9338	$C_{m_{q_3}}$	=	64.7190
$C_{m_{\alpha_1}}$	=	0.5110	$C_{m_{\delta_{stab_1}}}$	=	-0.3245	$C_{m_{q_2}}$	=	-68.5641
$C_{m_{\alpha_0}}$	=	-0.0866	$C_{m_{\delta_{stab_0}}}$	=	-0.9051	$C_{m_{q_1}}$	=	10.9921
						$C_{m_{q_0}}$	=	-4.1186

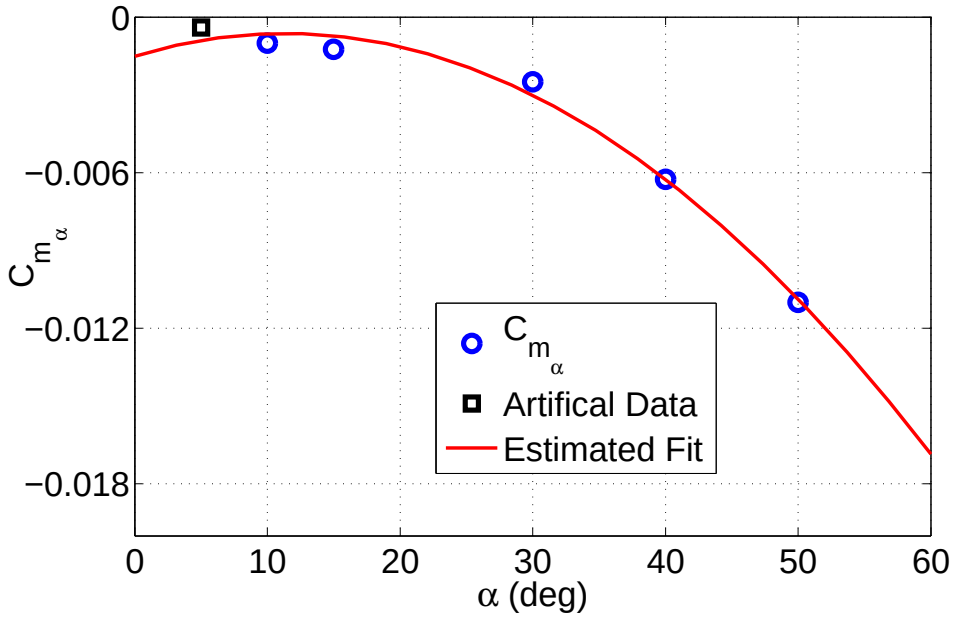

Figure A.1: Bare frame pitching moment

change drastically. Hence, the artificial data have been chosen to hold the coefficient value fixed at the last known value.

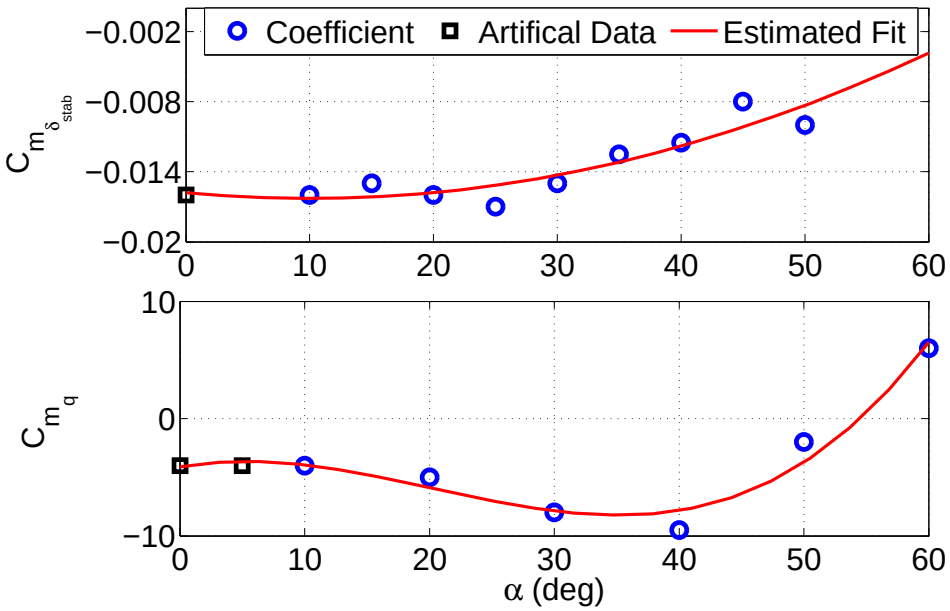

Figure A.2: (i) Top subplot shows the pitching moment coefficient due to stabilator deflection, and (ii) bottom subplot shows the pitching moment coefficient due to damping

A.1.2 Rolling Moment Coefficient, C_l

The rolling moment coefficients data are extracted from [14]. The rolling moment coefficient is modeled based on the contribution from: (i) the bare airframe, (ii) aileron & rudder deflection as a function of α, and (iii) damping derivative due to roll & yaw rate as a function of α. Equation A.2 and Table A.2 describes the rolling moment coefficient used in this thesis.

$$\begin{aligned} C_l = & \left(C_{l_{\beta_4}} \alpha^4 + C_{l_{\beta_3}} \alpha^3 + C_{l_{\beta_2}} \alpha^2 + C_{l_{\beta_1}} \alpha + C_{l_{\beta_0}} \right) \beta \\ & + \left(C_{l_{\delta_{ail_3}}} \alpha^3 + C_{l_{\delta_{ail_2}}} \alpha^2 + C_{l_{\delta_{ail_1}}} \alpha + C_{l_{\delta_{ail_0}}} \right) \delta_{ail} \\ & + \left(C_{l_{\delta_{rud_3}}} \alpha^3 + C_{l_{\delta_{rud_2}}} \alpha^2 + C_{l_{\delta_{rud_1}}} \alpha + C_{l_{\delta_{rud_0}}} \right) \delta_{rud} \\ & + \frac{b}{2V} \left(C_{l_{p_1}} \alpha + C_{l_{p_0}} \right) p + \frac{b}{2V} \left(C_{l_{r_2}} \alpha^2 + C_{l_{r_1}} \alpha + C_{l_{r_0}} \right) r \end{aligned} \tag{A.2}$$

Figure A.3 and A.4 show the rolling moment coefficient as a function of α. The artificial data for C_{l_β} is also shown in Figure A.3. The artificial data for C_{l_β} have been chosen from the available aerodynamic data for the F-16 [24]. The F-16 aircraft has similar values for C_{l_β} [24] as F/A-18. Moreover, the artificial data in Figure A.4

Table A.2: Rolling Moment Coefficient Data

Bareframe Coefficient			Control Derivatives			Damping Derivative		
$C_{l_{\beta_4}}$	=	-1.6196	$C_{l_{\delta_{ail_3}}}$	=	0.1989	$C_{l_{p_1}}$	=	0.2377
$C_{l_{\beta_3}}$	=	2.3843	$C_{l_{\delta_{ail_2}}}$	=	-0.2646	$C_{l_{p_0}}$	=	-0.3540
$C_{l_{\beta_2}}$	=	-0.3620	$C_{l_{\delta_{ail_1}}}$	=	-0.0516	$C_{l_{r_2}}$	=	-1.0871
$C_{l_{\beta_1}}$	=	-0.4153	$C_{l_{\delta_{ail_0}}}$	=	0.1424	$C_{l_{r_1}}$	=	0.7804
$C_{l_{\beta_0}}$	=	-0.0556	$C_{l_{\delta_{rud_3}}}$	=	-0.0274	$C_{l_{r_0}}$	=	0.1983
			$C_{l_{\delta_{rud_2}}}$	=	0.0083			
			$C_{l_{\delta_{rud_1}}}$	=	0.0014			
			$C_{l_{\delta_{rud_0}}}$	=	0.0129			

are chosen to hold the values fixed at the last known value.

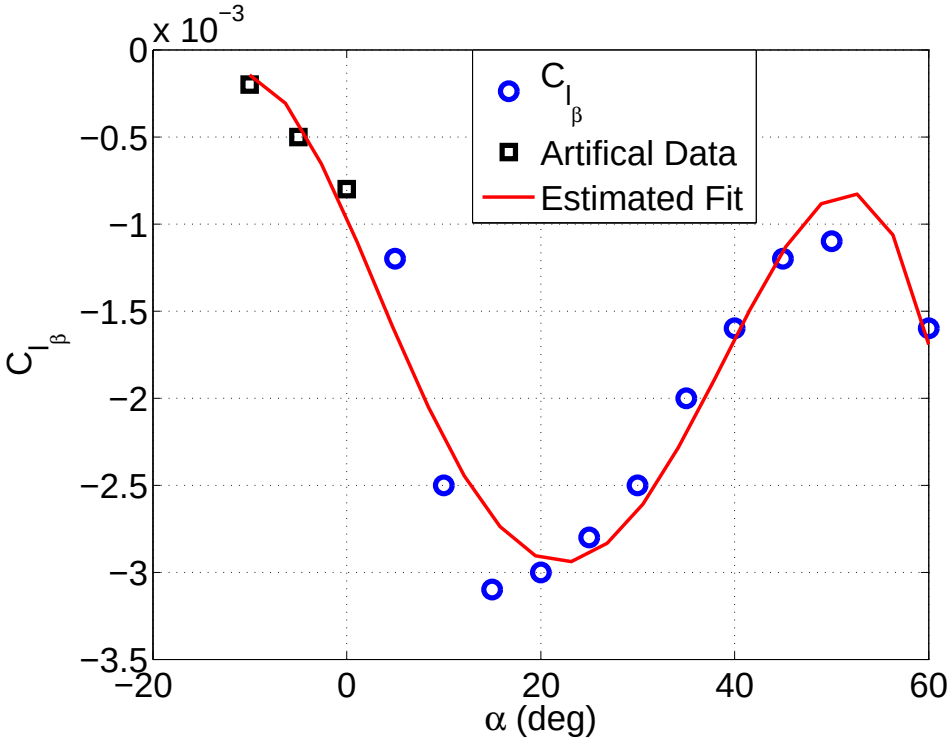

Figure A.3: Bare frame rolling moment coefficient

A.1.3 Yawing Moment Coefficient, C_n

The yawing moment coefficients data are extracted from [14]. The yawing moment coefficient is build-up based on the contribution from: (i) the bare airframe, (ii) aileron & rudder deflection as a function of α, and (iii) damping derivative due to

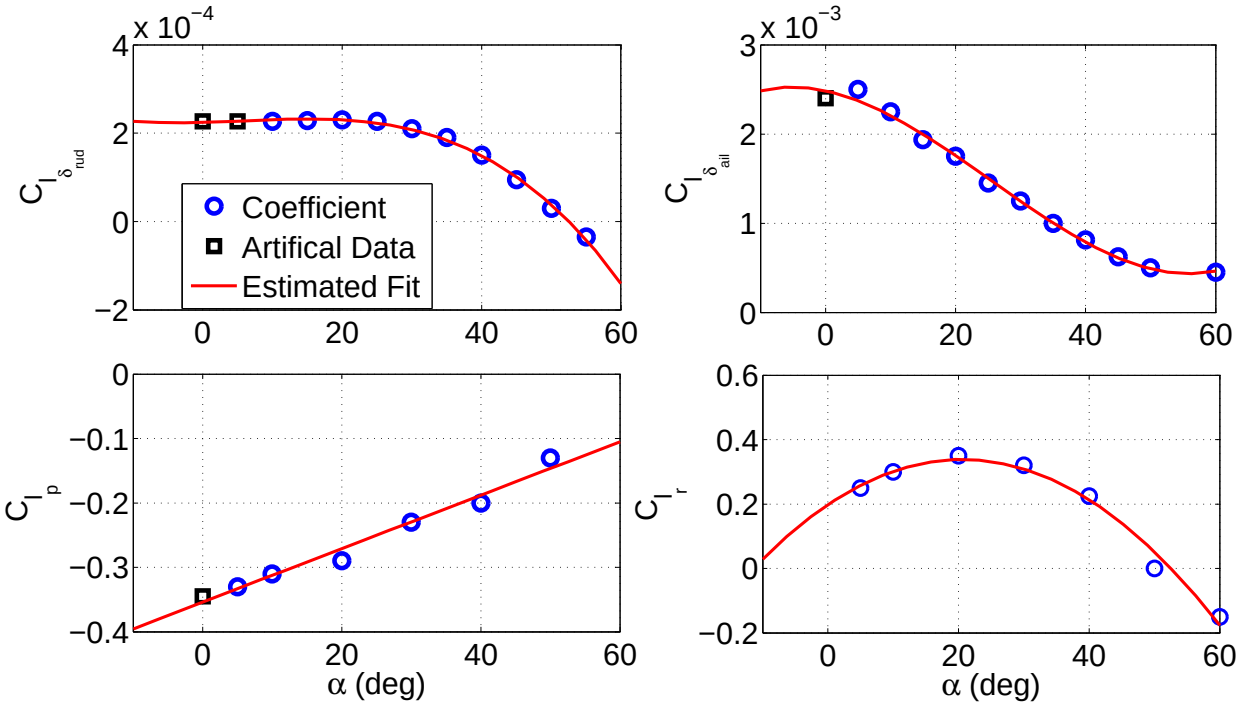

Figure A.4: (i) Top subplots show the rolling moment coefficient due to control effector's deflection, and (ii) bottom subplots show the rolling moment coefficient due to damping

roll & yaw rate as a function of α. Equation A.3 and Table A.3 describes the yawing moment coefficient used in this thesis.

$$\begin{aligned} C_n = & \left(C_{n_{\beta_2}}\alpha^2 + C_{n_{\beta_1}}\alpha + C_{n_{\beta_0}}\right)\beta \\ & + \left(C_{n_{\delta_{rud_4}}}\alpha^4 + C_{n_{\delta_{rud_3}}}\alpha^3 + C_{n_{\delta_{rud_2}}}\alpha^2 + C_{n_{\delta_{rud_1}}}\alpha + C_{n_{\delta_{rud_0}}}\right)\delta_{rud} \\ & + \left(C_{n_{\delta_{ail_3}}}\alpha^3 + C_{n_{\delta_{ail_2}}}\alpha^2 + C_{n_{\delta_{ail_1}}}\alpha + C_{n_{\delta_{ail_0}}}\right)\delta_{ail} \\ & + \frac{b}{2V}\left(C_{n_{p_1}}\alpha + C_{n_{p_0}}\right)p + \frac{b}{2V}\left(C_{n_{r_1}}\alpha + C_{n_{r_0}}\right)r \end{aligned} \tag{A.3}$$

Figure A.5-A.6 shows the plot of the yawing moment coefficient for the above three different effects. Again, the artificial data have been chosen to hold the low α values at last known value.

Table A.3: Yawing Moment Coefficient Data

Bareframe Coefficient			Control Derivatives			Damping Derivative		
$C_{n_{\beta_2}}$	=	-0.3816	$C_{n_{\delta_{ail_3}}}$	=	0.2694	$C_{n_{p_1}}$	=	-0.0881
$C_{n_{\beta_1}}$	=	0.0329	$C_{n_{\delta_{ail_2}}}$	=	-0.3413	$C_{n_{p_0}}$	=	0.0792
$C_{n_{\beta_0}}$	=	0.0885	$C_{n_{\delta_{ail_1}}}$	=	0.0584	$C_{n_{r_1}}$	=	-0.1307
			$C_{n_{\delta_{ail_0}}}$	=	0.0104	$C_{n_{r_0}}$	=	-0.4326
			$C_{n_{\delta_{rud_4}}}$	=	0.3899			
			$C_{n_{\delta_{rud_3}}}$	=	-0.8980			
			$C_{n_{\delta_{rud_2}}}$	=	0.5564			
			$C_{n_{\delta_{rud_1}}}$	=	-0.0176			
			$C_{n_{\delta_{rud_0}}}$	=	-0.0780			

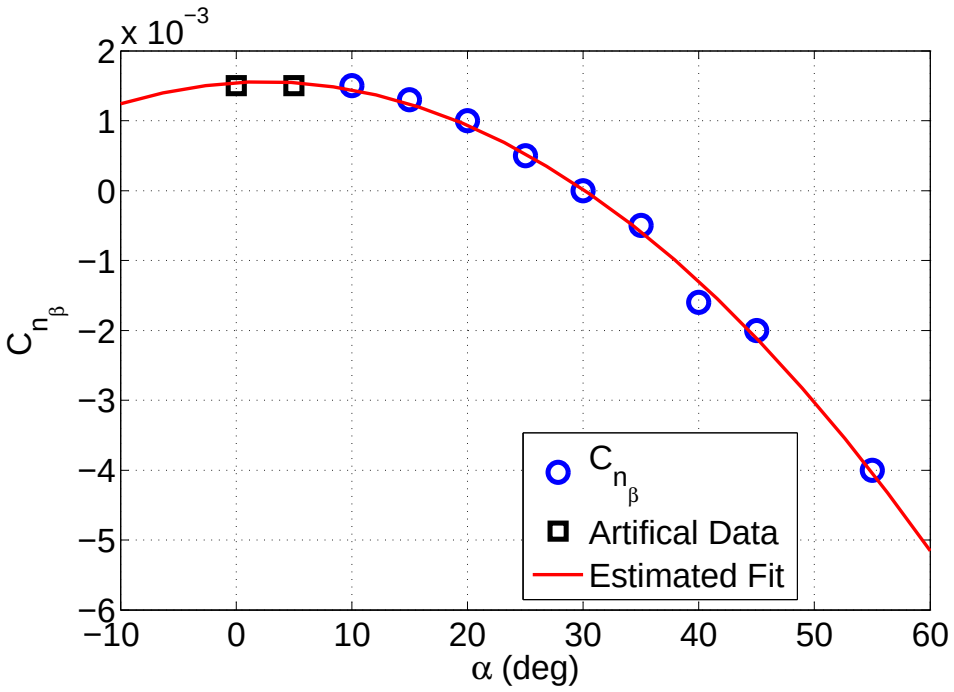

Figure A.5: Bare frame yawing moment coefficient

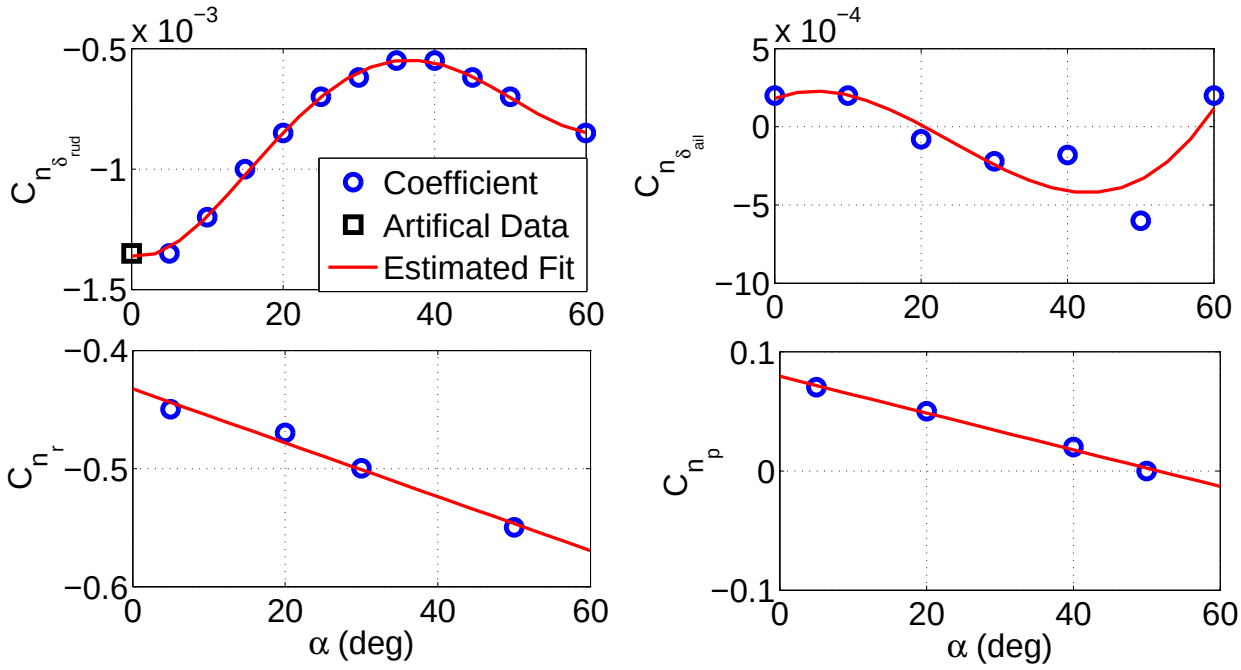

Figure A.6: (i) Top subplots show the yawing moment coefficient due to control effector's deflection, and (ii) bottom subplots show the yawing moment coefficient due to damping

A.1.4 Sideforce Coefficient, C_Y

The sideforce coefficients data are extracted from [14, 16]. The sideforce coefficient formed is based on the contribution from : (i) the bare airframe [16], and (ii) aileron & rudder deflection as a function of α [14]. Equation A.4 and Table A.4 describes the sideforce coefficient used in this thesis.

$$\begin{aligned} C_Y = & \left(C_{Y_{\beta_2}} \alpha^2 + C_{Y_{\beta_2}} \alpha + C_{Y_{\beta_0}} \right) \beta \\ & + \left(C_{Y_{\delta_{ail_3}}} \alpha^3 + C_{Y_{\delta_{ail_2}}} \alpha^2 + C_{Y_{\delta_{ail_1}}} \alpha + C_{Y_{\delta_{ail_0}}} \right) \delta_{ail} \\ & + \left(C_{Y_{\delta_{rud_3}}} \alpha^3 + C_{Y_{\delta_{rud_2}}} \alpha^2 + C_{Y_{\delta_{rud_1}}} \alpha + C_{Y_{\delta_{rud_0}}} \right) \delta_{rud} \end{aligned} \tag{A.4}$$

Figures A.7 and A.8 shows the contribution of the sideforce coefficient as a function of α. Note, in Figure A.7, the data has a lot of variations within the α range. However, the fit captures the characteristics of a fighter aircraft's sideforce coefficient. This has been verified by examining the F-16's sideforce coefficient [24].

Table A.4: Sideforce Coefficient Data

Bareframe Coefficient			Control Derivatives		
$C_{Y_{\beta_2}}$	=	-0.1926	$C_{Y_{\delta_{ail_3}}}$	=	-0.8500
$C_{Y_{\beta_1}}$	=	0.2654	$C_{Y_{\delta_{ail_2}}}$	=	1.5317
$C_{Y_{\beta_0}}$	=	-0.7344	$C_{Y_{\delta_{ail_1}}}$	=	-0.2403
			$C_{Y_{\delta_{ail_0}}}$	=	-0.1656
			$C_{Y_{\delta_{rud_3}}}$	=	0.9351
			$C_{Y_{\delta_{rud_2}}}$	=	-1.6921
			$C_{Y_{\delta_{rud_1}}}$	=	0.4082
			$C_{Y_{\delta_{rud_0}}}$	=	0.2054

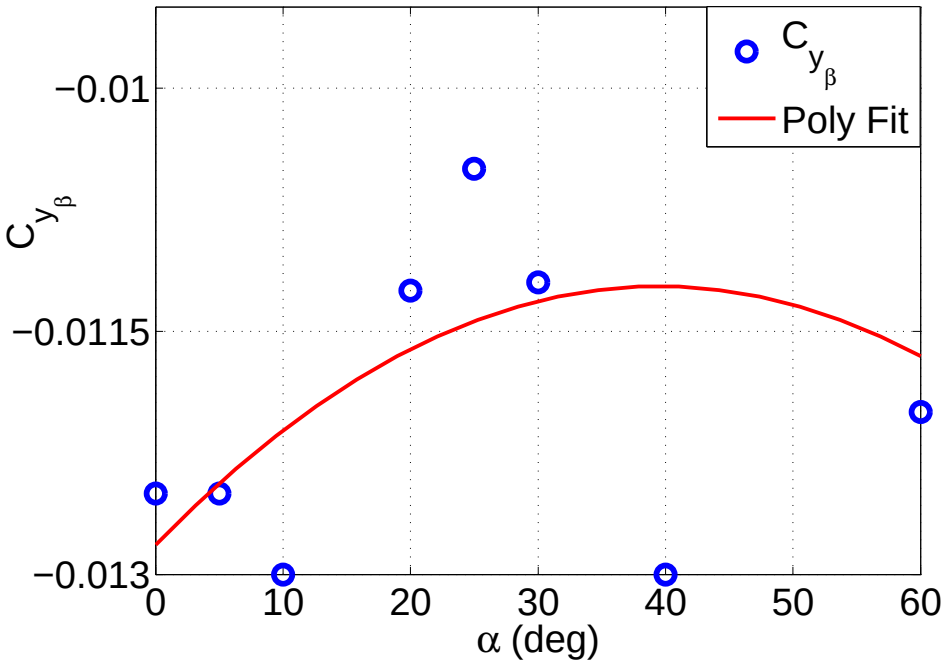

Figure A.7: Bare frame sideforce coefficient

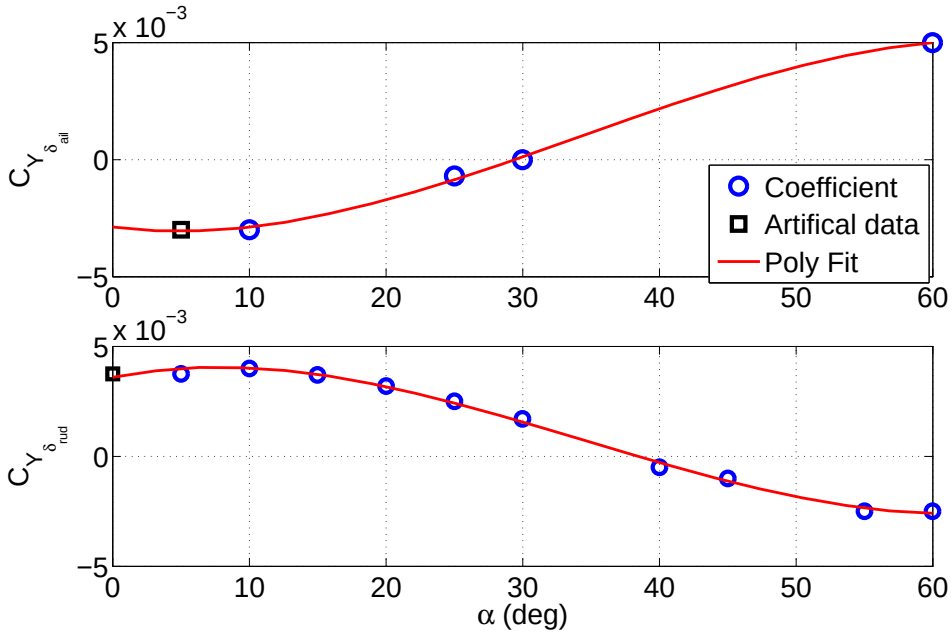

Figure A.8: Control effectors' contribution to sideforce coefficient

A.1.5 Lift Coefficient, C_L

The bare frame lift coefficient values have been extracted from [15] in polynomial form. The lift coefficient is modeled as Equation A.5. The control effector's contribution to lift coefficient are formulated by combining normal force data [40] and axial force data [17]. Equation A.5 and Table A.5 describes the lift force coefficient used in this thesis.

$$C_L = \left(C_{L_{\alpha_3}}\alpha^3 + C_{L_{\alpha_2}}\alpha^2 + C_{L_{\alpha_1}}\alpha + C_{L_{\alpha_0}}\right)\cos\left(\frac{2\beta}{3}\right) + \left(C_{L_{\delta_{stab_3}}}\alpha^3 + C_{L_{\delta_{stab_2}}}\alpha^2 + C_{L_{\delta_{stab_1}}}\alpha + C_{L_{\delta_{stab_0}}}\right)\delta_{stab} \quad \text{(A.5)}$$

Table A.5: Lift Force Coefficient Data

Bareframe Coefficient			Control Derivatives		
$C_{L_{\alpha_3}}$	=	1.1645	$C_{L_{\delta_{stab_3}}}$	=	2.1852
$C_{L_{\alpha_2}}$	=	-5.4246	$C_{L_{\delta_{stab_2}}}$	=	-2.6975
$C_{L_{\alpha_1}}$	=	5.6770	$C_{L_{\delta_{stab_1}}}$	=	0.4055
$C_{L_{\alpha_0}}$	=	-0.0204	$C_{L_{\delta_{stab_0}}}$	=	0.5725

Figures A.9 and A.10 shows the build up of the lift force coefficient as a function of α.

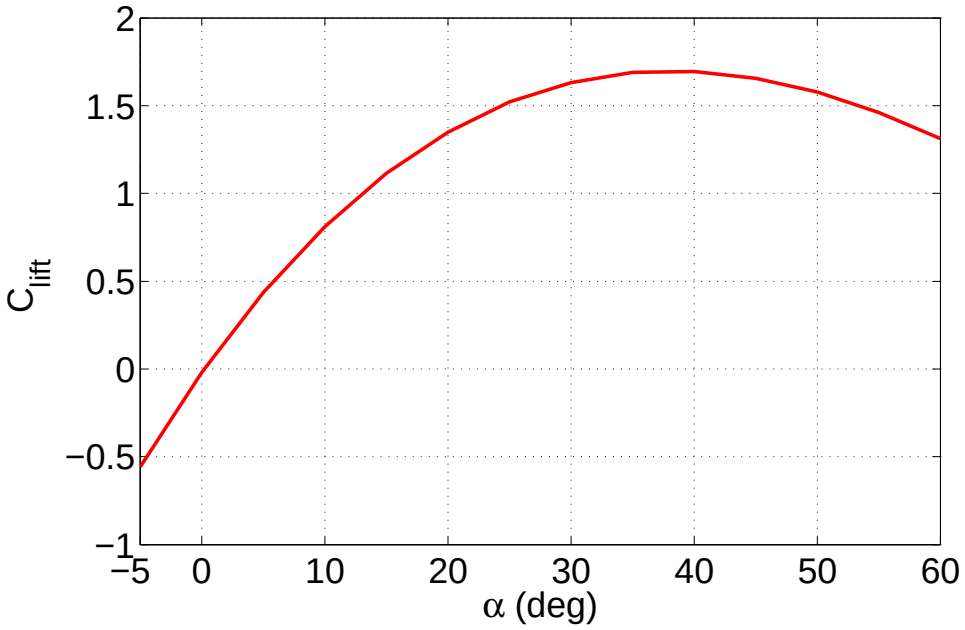

Figure A.9: Bare frame lift force coefficient

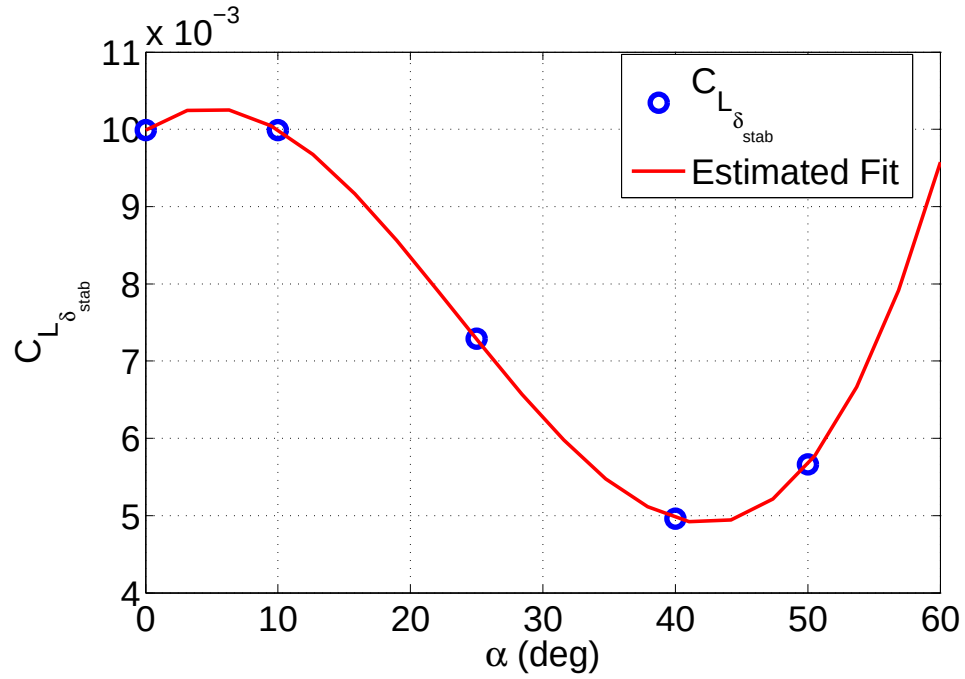

Figure A.10: Stabilator's contribution to lift force coefficient

A.1.6 Drag Coefficient, C_D

The bare frame drag coefficient values have been extracted from [15] in polynomial form. The drag coefficient is modeled as equation A.6. The control effector's contribution to drag force coefficient are formulated by combining normal force data [40] and axial force data [17]. Equation A.6 and Table A.6 describes the drag force coefficient used in this thesis.

$$\begin{aligned} C_D = &\left(C_{D_{\alpha_4}}\alpha^4 + C_{D_{\alpha_3}}\alpha^3 + C_{D_{\alpha_2}}\alpha^2 + C_{D_{\alpha_1}}\alpha + C_{D_{\alpha_0}}\right)\cos\beta + C_{D_0} \\ &+ \left(C_{D_{\delta_{stab_3}}}\alpha^3 + C_{D_{\delta_{stab_2}}}\alpha^2 + C_{D_{\delta_{stab_1}}}\alpha + C_{D_{\delta_{stab_0}}}\right)\delta_{stab} \end{aligned} \tag{A.6}$$

Table A.6: Drag Force Coefficient Data

Bareframe Coefficient			Control Derivatives		
$C_{D_{\alpha_4}}$	=	1.4610	$C_{D_{\delta_{stab_3}}}$	=	-3.8578
$C_{D_{\alpha_3}}$	=	-5.7341	$C_{D_{\delta_{stab_2}}}$	=	4.2360
$C_{D_{\alpha_2}}$	=	6.3971	$C_{D_{\delta_{stab_1}}}$	=	-0.2739
$C_{D_{\alpha_1}}$	=	-0.1995	$C_{D_{\delta_{stab_0}}}$	=	0.0366
$C_{D_{\alpha_0}}$	=	-1.4994			
C_{D_0}	=	1.5036			

Figures A.11 and A.12 show the build up of the drag force coefficient as a function of α.

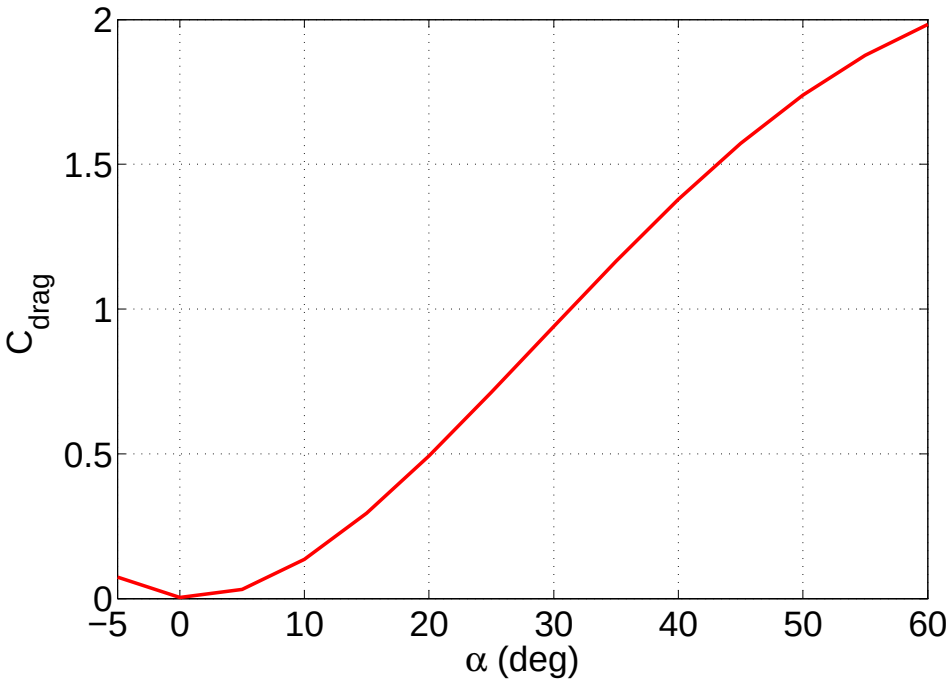

Figure A.11: Bare frame drag force coefficient

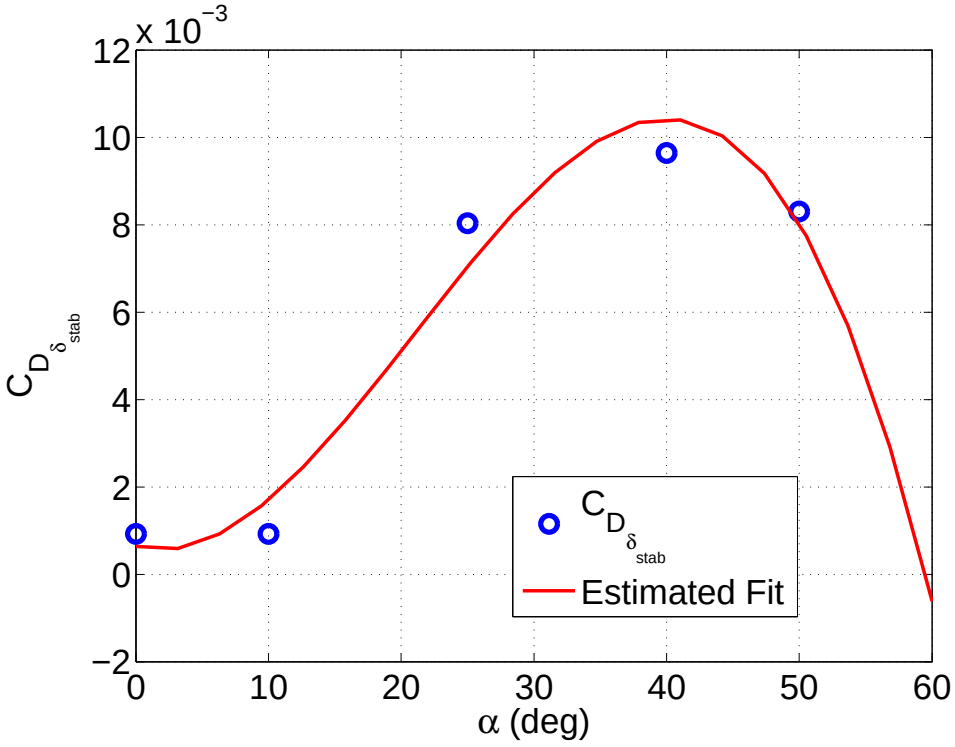

Figure A.12: Stabilator's contribution to drag force coefficient

A.2 Linear Plant

The linear plant described in Equation 5.1 is provided below. This linear plant is around the trim points mentioned in Table 5.1 for plant 4 and plant 8. Refer to Equation (2.1) for the ordering of the states and inputs. Due to space constraint, A matrix is shown below in two separate matrices. $A(1:9, 1:4)$ indicates the first four columns of the A matrix and $A(1:9, 5:9)$ indicates the last five columns of the A matrix.

A.2.1 Coordinated 35^o Bank Turn: Plant 4

$$A(1:9,1:4) = \begin{bmatrix} -6.932 \times 10^{-2} & 17.41 & -36.75 & 0 \\ -1.435 \times 10^{-4} & 2.719 \times 10^{-2} & -1.411 \times 10^{-3} & 3.467 \times 10^{-1} \\ -4.537 \times 10^{-4} & 1.870 \times 10^{-3} & -2.025 \times 10^{-1} & 0 \\ -1.304 \times 10^{-4} & -7.179 & -4.916 \times 10^{-1} & -6.172 \times 10^{-1} \\ 2.297 \times 10^{-5} & 0 & -8.667 \times 10^{-1} & 4.393 \times 10^{-2} \\ 1.964 \times 10^{-5} & 4.263 \times 10^{-1} & -1.329 \times 10^{-2} & 1.233 \times 10^{-3} \\ 0 & 0 & 0 & 1.000 \\ 0 & 0 & 0 & 0 \\ 0 & 0 & 0 & 0 \end{bmatrix}$$

$$A(1:9,5:9) = \begin{bmatrix} 0 & 0 & -6.066 & -31.54 & 0 \\ 0 & -9.380 \times 10^{-1} & 7.139 \times 10^{-2} & -1.691 \times 10^{-2} & 0 \\ 1.000 & 0 & -4.688 \times 10^{-2} & 7.563 \times 10^{-3} & 0 \\ -3.689 \times 10^{-2} & 7.631 \times 10^{-1} & 0 & 0 & 0 \\ -1.947 \times 10^{-1} & -2.026 \times 10^{-2} & 0 & 0 & 0 \\ 1.579 \times 10^{-2} & -1.600 \times 10^{-1} & 0 & 0 & 0 \\ 1.941 \times 10^{-1} & 2.771 \times 10^{-1} & 0 & 6.258 \times 10^{-2} & 0 \\ 8.192 \times 10^{-1} & -5.615 \times 10^{-2} & 0 & 0 & 0 \\ 6.055 \times 10^{-1} & 0 & 2.006 \times 10^{-2} & 0 & 0 \end{bmatrix}$$

$$B = \begin{bmatrix} 0 & 0 & -7.560 & 9.067 \times 10^{-4} \\ -6.952 \times 10^{-3} & 1.293 \times 10^{-2} & 0 & 0 \\ 0 & 0 & -3.425 \times 10^{-2} & -9.577 \times 10^{-7} \\ 4.249 & 5.989 \times 10^{-1} & 0 & 0 \\ 0 & 0 & -1.796 & 0 \\ -7.287 \times 10^{-2} & -2.877 \times 10^{-1} & 0 & 0 \\ 0 & 0 & 0 & 0 \\ 0 & 0 & 0 & 0 \\ 0 & 0 & 0 & 0 \end{bmatrix}$$

$$C = \begin{bmatrix} 0 & -5.758 \times 10^{-1} & 0 & 0 & 0 & 0 & 0 & 0 & 0 \\ 0 & 0 & 0 & 1 & 0 & 0 & 0 & 0 & 0 \\ 0 & 0 & 0 & 0 & 0 & 1 & 0 & 0 & 0 \\ 0 & 0 & 1 & 0 & 0 & 0 & 0 & 0 & 0 \\ 0 & 1 & 0 & 0 & 0 & 0 & 0 & 0 & 0 \\ 0 & 0 & 0 & 0 & 1 & 0 & 0 & 0 & 0 \\ 0 & 2.719 \times 10^{-2} & -1.411 \times 10^{-3} & 3.467 \times 10^{-1} & 0 & -9.380 \times 10^{-1} & 7.139 \times 10^{-2} & 0 & 0 \end{bmatrix}$$

$$D = \begin{bmatrix} -1.298 \times 10^{-1} & -1.610 \times 10^{-1} & 0 & 0 \\ 0 & 0 & 0 & 0 \\ 0 & 0 & 0 & 0 \\ 0 & 0 & 0 & 0 \\ 0 & 0 & 0 & 0 \\ 0 & 0 & 0 & 0 \\ -6.952 \times 10^{-3} & 1.293 \times 10^{-2} & 0 & 0 \end{bmatrix}$$

A.2.2 Uncoordinated 35^o Bank Turn: Plant 8

$$A(1:9,1:4) = \begin{bmatrix} -7.921 \times 10^{-2} & 7.516 & -35.84 & 0 \\ -1.635 \times 10^{-4} & 2.847 \times 10^{-2} & -1.650 \times 10^{-2} & 3.649 \times 10^{-1} \\ -4.659 \times 10^{-4} & 5.902 \times 10^{-3} & -1.998 \times 10^{-1} & -1.642 \times 10^{-1} \\ -1.441 \times 10^{-4} & -7.211 & -2.116 & -6.067 \times 10^{-1} \\ 2.667 \times 10^{-5} & 0 & -9.807 \times 10^{-1} & 4.689 \times 10^{-2} \\ 2.062 \times 10^{-5} & 3.995 \times 10^{-1} & -2.621 \times 10^{-1} & 1.188 \times 10^{-3} \\ 0 & 0 & 0 & 1.000 \\ 0 & 0 & 0 & 0 \\ 0 & 0 & 0 & 0 \end{bmatrix}$$

$$A(1:9,5:9) = \begin{bmatrix} 0 & 0 & -1.914 & -32.12 & 0 \\ 0 & -9.310 \times 10^{-1} & 7.219 \times 10^{-2} & -3.414 \times 10^{-3} & 0 \\ 1.000 & -6.434 \times 10^{-2} & -4.643 \times 10^{-2} & 5.671 \times 10^{-3} & 0 \\ -3.938 \times 10^{-2} & 7.608 \times 10^{-1} & 0 & 0 & 0 \\ -2.031 \times 10^{-1} & -2.487 \times 10^{-2} & 0 & 0 & 0 \\ 1.938 \times 10^{-2} & -1.607 \times 10^{-1} & 0 & 0 & 0 \\ 2.254 \times 10^{-1} & 3.219 \times 10^{-1} & 0 & 6.939 \times 10^{-2} & 0 \\ 8.192 \times 10^{-1} & -6.011 \times 10^{-2} & 0 & 0 & \\ 6.163 \times 10^{-1} & 0 & 2.537 \times 10^{-2} & 0 & \end{bmatrix}$$

$$B = \begin{bmatrix} -3.768 \times 10^{-1} & 7.476 \times 10^{-1} & -8.062 & 8.863 \times 10^{-4} \\ -6.106 \times 10^{-3} & 1.211 \times 10^{-2} & 4.061 \times 10^{-3} & 0 \\ 0 & 0 & -3.338 \times 10^{-2} & -1.023 \times 10^{-6} \\ 4.114 & 5.945 \times 10^{-1} & 0 & 0 \\ 0 & 0 & -1.782 & 0 \\ -7.977 \times 10^{-2} & -2.758 \times 10^{-1} & 0 & 0 \\ 0 & 0 & 0 & 0 \\ 0 & 0 & 0 & 0 \\ 0 & 0 & 0 & 0 \end{bmatrix}$$

$$C = \begin{bmatrix} 0 & -5.758 \times 10^{-1} & 0 & 0 & 0 & 0 & 0 & 0 & 0 \\ 0 & 0 & 0 & 1 & 0 & 0 & 0 & 0 & 0 \\ 0 & 0 & 0 & 0 & 0 & 1 & 0 & 0 & 0 \\ 0 & 0 & 1 & 0 & 0 & 0 & 0 & 0 & 0 \\ 0 & 1 & 0 & 0 & 0 & 0 & 0 & 0 & 0 \\ 0 & 0 & 0 & 0 & 1 & 0 & 0 & 0 & 0 \\ 0 & 2.847 \times 10^{-2} & 1.650 \times 10^{-2} & 3.649 \times 10^{-1} & 0 & -9.310 \times 10^{-1} & 7.219 \times 10^{-2} & 0 & 0 \end{bmatrix}$$

$$D = \begin{bmatrix} -1.298 \times 10^{-1} & -1.610 \times 10^{-1} & 0 & 0 \\ 0 & 0 & 0 & 0 \\ 0 & 0 & 0 & 0 \\ 0 & 0 & 0 & 0 \\ 0 & 0 & 0 & 0 \\ 0 & 0 & 0 & 0 \\ -6.106 \times 10^{-3} & 1.211 \times 10^{-2} & 4.061 \times 10^{-3} & 0 \end{bmatrix}$$

A.3 Basics of SOS Optimization

This appendix provides a brief review of sum-of-squares optimizations. Additional details can be found in [12, 41, 42]. A polynomial p is a *sum of squares* (SOS) if there exist polynomials $\{f_i\}_{i=1}^m$ such that $p = \sum_{i=1}^m f_i^2$. For example, $p = x^2 - 4xy + 7y^2$ is a sum of squares since $p = f_1^2 + f_2^2$ where $f_1 = (x - 2y)^2$ and $f_2 = 3y^2$. Note that if p is a sum of squares then $p(x) \geq 0 \ \forall x \in \mathbb{R}^n$. Thus $p \in$ SOS is a sufficient condition for a polynomial to be globally non-negative.

Quadratic forms can be expressed as $p(x) = x^T Q x$ where Q is a symmetric matrix. Similarly, polynomials of degree $\leq 2d$ can be expressed as $p(x) = z(x)^T Q z(x)$ where the vector z contains all monomials of degree $\leq d$. This is known as the Gram matrix form. An important fact is that p is SOS if and only if there exists $Q \succeq 0$ such that $p(x) = z(x)^T Q z(x)$. This provides a connection between SOS polynomials and positive semidefinite matrices.

A sum-of-squares program is an optimization problem with a linear cost and SOS constraints on the decision variables [36]:

$$\begin{aligned} &\min_{u \in \mathbb{R}^n} c^T u \\ &\text{subject to: } a_{k,0}(x) + a_{k,1}(x)u_1 + \cdots + a_{k,n}(x)u_n \in \text{ SOS } (k = 1, \ldots N_s) \end{aligned} \tag{A.7}$$

The vector $c \in \mathbb{R}^n$ and polynomials $\{a_{k,j}\}$ are given as part of the optimization data. $u \in \mathbb{R}^n$ are decision variables. SOS programs can be converted to semidefinite programs (SDPs) using the connection between SOS polynomials and positive semidefinite matrices. SOSTOOLS [36], Yalmip [37], and SOSOPT [39] are freely available MATLAB toolboxes for solving SOS optimizations. These packages allow the user to specify the polynomial constraints using a symbolic toolbox. Then they convert the SOS optimization into an SDP which is solved with SeDuMi [38, 43] or another freely available SDP solver. Finally the solution of the SDP is converted back to a polynomial solution.

A drawback is that the size of the resulting SDP grows rapidly if the SOS optimization involves polynomials with many variables and/or high degree. For a generic degree $2d$ polynomial p in n variables, the Gram matrix representation involves $\binom{n+d}{d}$ monomials. An SOS constraint on p is enforced via a positive semidefinite constraint on the $l_z \times l_z$ Gram matrix Q. For example, the Gram matrix has dimension $l_z = 495$

for a generic degree $2d = 8$ polynomial in $n = 8$ variables. The size of this positive semidefinite constraint is at or near the limits of current semidefinite programming solvers. While various techniques can be used to exploit the problem structure [44], this computational growth is a generic trend in SOS optimizations. For analysis of polynomial systems, this roughly limits the approach to systems with fewer than 8-10 states and cubic degree models. Polynomial models of higher degree can be handled if there are fewer states.

A.4 Closed-loop Polynomial Model

A.4.1 Baseline Polynomial Model

The cubic degree polynomial approximation for the closed-loop system with the baseline control law is:

$$\begin{aligned}
\dot{\beta} = & -3.978 \times 10^{-3}\alpha^3 - 2.191 \times 10^{-1}\alpha^2\beta + 2.9427 \times 10^{-5}\alpha^2\phi - 2.458 \times 10^{-3}\alpha\beta^2 \\
& + 5.509 \times 10^{-2}\alpha\beta\phi - 4.330 \times 10^{-5}\alpha\phi^2 + 6.2222 \times 10^{-2}\beta^3 - 1.672 \times 10^{-2}\beta^2\phi \\
& + 2.785 \times 10^{-3}\beta\phi^2 - 6.786 \times 10^{-3}\phi^3 + 2.708 \times 10^{-2}\alpha^2 + 2.017 \times 10^{-1}\alpha\beta \\
& - 5.323 \times 10^{-5}\alpha\phi - 2.698 \times 10^{-2}\beta^2 + 2.729 \times 10^{-2}\beta\phi - 2.747 \times 10^{-2}\phi^2 \\
& + (-3.181 \times 10^{-1}\alpha^2 + 3.466 \times 10^{-2}\beta^2 + 9.638 \times 10^{-1}\alpha)p \\
& + (-3.634 \times 10^{-1}\alpha\beta + 2.708 \times 10^{-1}\beta)q \\
& + (4.009 \times 10^{-1}\alpha^2 - 5.344 \times 10^{-3}\beta^2 + 3.141 \times 10^{-1}\alpha)r \\
& + (2.496 \times 10^{-2}\alpha^2 - 2.630 \times 10^{-2}\beta^2 - 5.127 \times 10^{-2}\alpha)x_{c_B} \\
& + -1.411 \times 10^{-3}\alpha + 2.314 \times 10^{-2}\beta + 3.474 \times 10^{-1}p + 7.134 \times 10^{-2}\phi \\
& - 9.225 \times 10^{-1}r + 1.406 \times 10^{-2}x_{c_B}
\end{aligned}$$

$$\begin{aligned}
\dot{\alpha} = & -2.139 \times 10^{-1}\alpha^3 + 7.550 \times 10^{-3}\alpha^2\beta + 3.540 \times 10^{-2}\alpha^2\phi - 1.846 \times 10^{-2}\alpha\beta^2 \\
& - 4.181 \times 10^{-5}\alpha\beta\phi + 1.029 \times 10^{-2}\alpha\phi^2 - 4.365 \times 10^{-3}\beta^3 - 4.154 \times 10^{-3}\beta^2\phi \\
& - 6.8825 \times 10^{-5}\beta\phi^2 + 1.252 \times 10^{-2}\phi^3 + 3.637 \times 10^{-1}\alpha^2 - 5.181 \times 10^{-2}\alpha\beta \\
& + 1.364 \times 10^{-2}\alpha\phi - 2.243 \times 10^{-2}\beta^2 + 1.093 \times 10^{-4}\beta\phi - 3.648 \times 10^{-2}\phi^2 \\
& + (6.357 \times 10^{-1}\alpha\beta - 9.576 \times 10^{-1}\beta)p \\
& + (-1.132\alpha^2 + 1.988 \times 10^{-1}\beta^2 + 6.941 \times 10^{-1}\alpha)q \\
& + (-7.499 \times 10^{-1}\alpha\beta - 3.619 \times 10^{-1}\beta)r \\
& + -2.299 \times 10^{-1}\alpha + 1.870 \times 10^{-3}\beta - 4.688 \times 10^{-2}\phi + 7.259 \times 10^{-1}q
\end{aligned}$$

$$\begin{aligned}
\dot{p} = & -3.314 \times 10^{-2}\alpha^3 - 19.69\alpha^2\beta - 1.646 \times 10^{-3}\alpha\beta^2 + 18.79\beta^3 - 8.022 \times 10^{-2}\alpha^2 \\
& + 15.86\alpha\beta + 1.219 \times 10^{-3}\beta^2 + (-5.204 \times 10^{-1}\alpha^2 + 1.252\alpha)p \\
& + (-4.737\alpha^2 + 6.823 \times 10^{-2}\alpha)r - 8.150 \times 10^{-1}qr - 3.173 \times 10^{-2}pq \\
& + (-2.056\alpha^2 + 3.553 \times 10^{-2}\alpha)x_{c_B} + 4.916 \times 10^{-2}\alpha - 7.366\beta - 9.538 \times 10^{-1}p \\
& - 3.688 \times 10^{-2}q + 1.479r + 6.513 \times 10^{-1}x_{c_B}
\end{aligned}$$

$$\dot{q} = 1.553\alpha^3 - 2.174\alpha^2 + (17.13\alpha^2 + 4.40\alpha)q - 1.964 \times 10^{-2}r^2 + 9.712 \times 10^{-1}pr + 1.964 \times 10^{-2}p^2 + (-2.303\alpha + 4.393 \times 10^{-2}p - 14.56q - 2.026 \times 10^{-2}r)$$

$$\begin{aligned}\dot{r} = {} & -3.196 \times 10^{-2}\alpha^3 - 1.678\alpha^2\beta + 1.274 \times 10^{-2}\alpha\beta^2 - 3.236 \times 10^{-1}\beta^3 \\ & + 3.869 \times 10^{-2}\alpha^2 - 1.795\alpha\beta - 9.442 \times 10^{-3}\beta^2 \\ & + (-9.543 \times 10^{-2}\alpha^2 + 2.081 \times 10^{-2}\alpha)p + (-5.179 \times 10^{-1}\alpha^2 + 4.541 \times 10^{-1}\alpha)r \\ & + 3.173 \times 10^{-2}qr - 7.543 \times 10^{-1}pq + (-5.102 \times 10^{-1}\alpha^2 + 4.497 \times 10^{-1}\alpha)x_{c_B} \\ & + -1.329 \times 10^{-2}\alpha + 5.164 \times 10^{-1}\beta + 5.438 \times 10^{-3}p + 1.579 \times 10^{-2}q \\ & - 5.042 \times 10^{-1}r - 3.129 \times 10^{-1}x_{c_B}\end{aligned}$$

$$\dot{\phi} = (-1.481 \times 10^{-1}\phi^2 + 2.921 \times 10^{-1}\phi)q + (-7.226 \times 10^{-2}\phi^2 - 2.181 \times 10^{-1}\phi)r + p + 1.941 \times 10^{-1}q + 2.772 \times 10^{-1}r$$

$$\dot{x}_{c_B} = 4.900r - x_{c_B}$$

A.4.2 Revised Polynomial Model

The cubic degree polynomial approximation for the closed-loop system with the revised control law is:

$$
\begin{aligned}
\dot{\beta} = {} & 3.153 \times 10^{-6}\alpha^3 - 2.065 \times 10^{-1}\alpha^2\beta + 1.958 \times 10^{-3}\alpha^2\phi - 1.360 \times 10^{-3}\alpha\beta^2 \\
& + 5.556 \times 10^{-2}\alpha\beta\phi - 4.814 \times 10^{-4}\alpha\phi^2 + 5.772 \times 10^{-2}\beta^3 - 1.964 \times 10^{-2}\beta^2\phi \\
& + 3.563 \times 10^{-3}\beta\phi^2 - 6.644 \times 10^{-3}\phi^3 + 2.404 \times 10^{-2}\alpha^2 + 1.717 \times 10^{-1}\alpha\beta \\
& - 6.328 \times 10^{-3}\alpha\phi - 2.454 \times 10^{-2}\beta^2 + 2.606 \times 10^{-2}\beta\phi - 2.771 \times 10^{-2}\phi^2 \\
& + (-3.010 \times 10^{-1}\alpha^2 + 2.034 \times 10^{-2}\beta^2 + 9.247 \times 10^{-1}\alpha)p \\
& + (-3.634 \times 10^{-1}\alpha\beta + 2.708 \times 10^{-1}\beta)q \\
& + (3.558 \times 10^{-1}\alpha^2 + 3.255 \times 10^{-2}\beta^2 + 4.181 \times 10^{-1}\alpha)r \\
& + (2.576 \times 10^{-2}\alpha^2 - 2.700 \times 10^{-2}\beta^2 - 5.287 \times 10^{-2}\alpha)x_{c_R} \\
& + -1.434 \times 10^{-3}\alpha + 2.750 \times 10^{-2}\beta + 3.529 \times 10^{-1}p \\
& + 7.253 \times 10^{-2}\phi - 9.372 \times 10^{-1}r + 1.429 \times 10^{-2}x_{c_R}
\end{aligned}
$$

$$
\begin{aligned}
\dot{\alpha} = {} & -2.139 \times 10^{-1}\alpha^3 + 7.550 \times 10^{-3}\alpha^2\beta + 3.540 \times 10^{-2}\alpha^2\phi - 1.845 \times 10^{-2}\alpha\beta^2 \\
& - 4.182 \times 10^{-5}\alpha\beta\phi + 1.029 \times 10^{-2}\alpha\phi^2 - 4.365 \times 10^{-3}\beta^3 - 4.154 \times 10^{-3}\beta^2\phi \\
& - 6.883 \times 10^{-5}\beta\phi^2 + 1.252 \times 10^{-2}\phi^3 + 3.637 \times 10^{-1}\alpha^2 - 5.181 \times 10^{-2}\alpha\beta \\
& + 1.364 \times 10^{-2}\alpha\phi - 2.243 \times 10^{-2}\beta^2 + 1.093 \times 10^{-4}\beta\phi - 3.649 \times 10^{-2}\phi^2 \\
& + (6.357 \times 10^{-1}\alpha\beta - 9.576 \times 10^{-1}\beta)p \\
& + (-1.132\alpha^2 + 1.988 \times 10^{-1}\beta^2 + 6.941 \times 10^{-1}\alpha)q \\
& + (-7.499 \times 10^{-1}\alpha\beta - 3.619 \times 10^{-1}\beta)r \\
& + -2.299 \times 10^{-1}\alpha + 1.871 \times 10^{-3}\beta - 4.688 \times 10^{-2}\phi + 7.259 \times 10^{-1}q
\end{aligned}
$$

$$
\begin{aligned}
\dot{p} = & -4.415 \times 10^{-1}\alpha^3 - 23.22\alpha^2\beta - 7.476 \times 10^{-1}\alpha^2\phi - 2.556 \times 10^{-1}\alpha\beta^2 \\
& + 20.20\beta^3 + 2.031 \times 10^{-1}\alpha^2 + 20.65\alpha\beta + 1.149\alpha\phi + 6.667 \times 10^{-2}\beta^2 \\
& + (-5.104\alpha^2 + 7.496\alpha)p + (7.453\alpha^2 - 16.52\alpha)r \\
& - 3.173 \times 10^{-2}pq - 8.151 \times 10^{-1}qr + (-2.227\alpha^2 + 2.823 \times 10^{-1}\alpha)x_{c_R} \\
& + 6.123 \times 10^{-2}\alpha - 9.701\beta - 3.923p - 6.103 \times 10^{-1}\phi \\
& - 3.688 \times 10^{-2}q + 9.365r + 5.311 \times 10^{-1}x_{c_R}
\end{aligned}
$$

$$
\begin{aligned}
\dot{q} = & \ 1.554\alpha^3 - 2.175\alpha^2 + (17.13\alpha^2 + 4.404\alpha)q + 1.964 \times 10^{-2}p^2 - 1.964 \times 10^{-2}r^2 \\
& + 9.713 \times 10^{-1}pr + -2.303\alpha + 4.393 \times 10^{-2}p - 14.55q - 2.026 \times 10^{-2}r
\end{aligned}
$$

$$
\begin{aligned}
\dot{r} = & -2.469 \times 10^{-1}\alpha^3 - 2.324\alpha^2\beta + 9.538 \times 10^{-2}\alpha\beta^2 - 4.018 \times 10^{-2}\beta^3 \\
& + 1.781 \times 10^{-1}\alpha^2 - 1.419\alpha\beta - 2.519 \times 10^{-2}\beta^2 \\
& + (-9.357 \times 10^{-1}\alpha^2 + 5.264 \times 10^{-1}\alpha)p + (1.7156\alpha^2 - 8.8988 \times 10^{-1}\alpha)r \\
& + 3.173 \times 10^{-2}qr - 7.544 \times 10^{-1}pq + (-5.427 \times 10^{-1}\alpha^2 + 4.694 \times 10^{-1}\alpha)x_{c_R} \\
& + (-1.344 \times 10^{-2}\alpha + 5.455 \times 10^{-1}\beta + 4.254 \times 10^{-2}p + 7.624 \times 10^{-3}\phi \\
& + 1.579 \times 10^{-2}q - 6.027 \times 10^{-1}r - 3.114 \times 10^{-1}x_{c_R})
\end{aligned}
$$

$$
\begin{aligned}
\dot{\phi} = & (-1.481 \times 10^{-1}\phi^2 + 2.921 \times 10^{-1}\phi)q + (-7.226 \times 10^{-2}\phi^2 - 2.182 \times 10^{-1}\phi)r \\
& + p + 1.941 \times 10^{-1}q + 2.772 \times 10^{-1}r
\end{aligned}
$$

$$
\dot{x}_{c_R} = 4.900r - x_{c_R}
$$